Single-electron analysis and open charm cross section in proton-proton collisions at $\sqrt{s}$ = 7 TeV

TECHNISCHE UNIVERSITÄT DARMSTADT

Fachbereich Physik
Institut für Kernphysik

HGS-HIRe for FAIR
Helmholtz Graduate School for Hadron and Ion Research
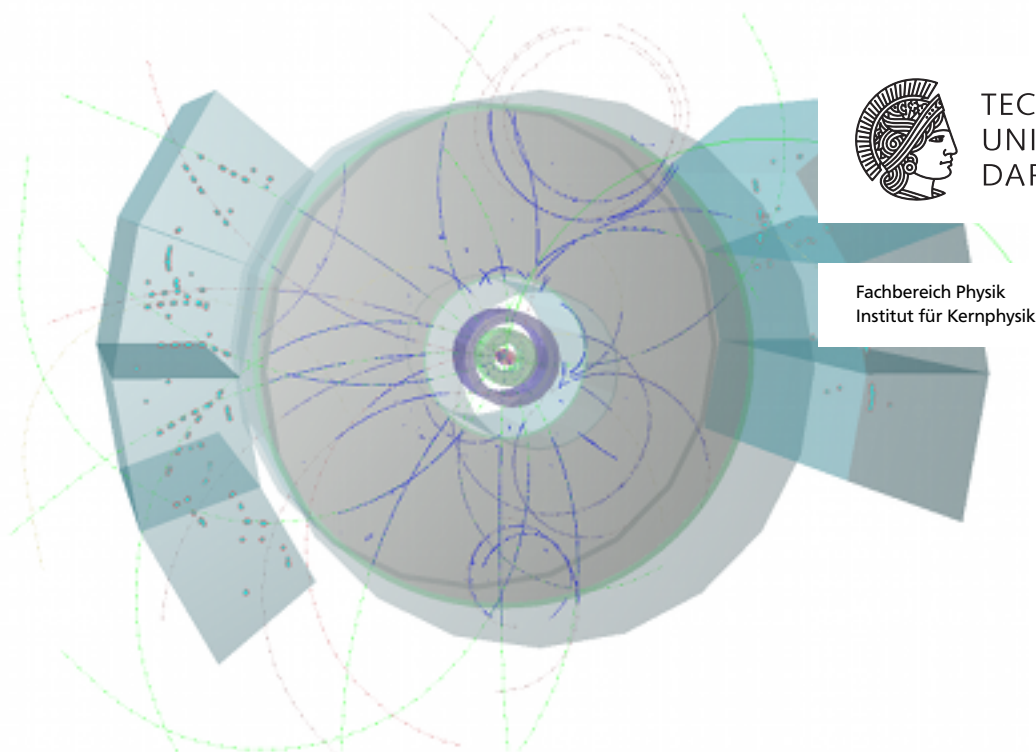
GSI

ALICE
A JOURNEY OF DISCOVERY

Single-electron analysis and open charm cross section in proton-proton collisions at $\sqrt{s}$ = 7 TeV
Single-Elektron Analyse und Opencharm-Wirkungsquerschnitt in Proton-Proton Kollisionen bei $\sqrt{s}$ = 7 TeV

Genehmigte Dissertation von M. Sc. Markus Fasel aus Koblenz

1. Gutachten: Professor Dr. Braun-Munzinger
2. Gutachten: Professor Dr. Wambach

Tag der Einreichung: 26. Juni 2012
Tag der Prüfung: 31. Oktober 2012

Darmstadt — D 17
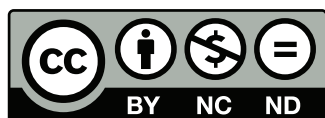
Erklärung zur Dissertation

Hiermit versichere ich, die vorliegende Dissertation ohne Hilfe Dritter nur mit den angegebenen Quellen und Hilfsmitteln angefertigt zu haben. Alle Stellen, die aus Quellen entnommen wurden, sind als solche kenntlich gemacht. Diese Arbeit hat in gleicher oder ähnlicher Form noch keiner Prüfungsbehörde vorgelegen.

Darmstadt, den 26. Juni 2012

(Markus Fasel)

Abstract

The Large Hadron Collider (LHC) at CERN is the world's highest energy hadron collider, providing proton-proton collisions currently at a centre-of-mass energy $\sqrt{s} = 8$ TeV and Pb-Pb collisions at $\sqrt{s_{NN}} = 2.76$ TeV. This opens a new energy regime, which allows the study of QCD in elementary pp-collisions and in the extreme environment of Pb-Pb collisions, as well as providing a discovery potential for rare and exotic particles. ALICE is the dedicated heavy-ion experiment at the LHC. The experiment is optimised to provide excellent tracking and particle identification capabilities, in particular at low-p_t, where the bulk of the particles is produced in heavy-ion collisions as well as in proton-proton collisions.

The production of heavy quarks is described in proton-proton collisions by next-to-leading order perturbative QCD (pQCD) calculations. Thus, the measurement of heavy-quark production in proton-proton collisions serves as a test of pQCD. Measurements performed at SPS, RHIC, and Tevatron experiments showed a good agreement with pQCD, where the data were usually at the upper limit of the prediction. In addition, measurements in proton-proton collisions serve as reference for heavy-ion collisions, in which heavy quarks are essential probes for parton energy loss in a deconfined medium. Heavy-quark production can be studied either with hadronic or in semi-leptonic decay channels. The analysis presented in this thesis is performed in the semi-electronic decay channel with the ALICE apparatus.

A crucial device for the electron selection is the Transition Radiation Detector (TRD), which provides an important contribution to the electron-pion separation for momenta larger than 1 GeV/c. In November 2010, the first data were recorded with the experiment. The electron selection performance was studied for the first time on real data using data-driven methods. A pion-rejection factor of 23 at a momentum of 2 GeV/c was obtained using a likelihood method on the total charge deposit in the detector for tracks with the maximum amount of charge deposit measurements.

The inclusive electron p_t-spectrum, which contains contributions from heavy-flavour hadrons as well as from various background sources, was measured for 0.5 GeV/c $< p_t <$ 8 GeV/c in proton-proton collisions at $\sqrt{s} = 7$ TeV at midrapidity ($|y| < 0.5$). The contribution of background electrons was quantified using a cocktail method, and it was subtracted from the inclusive spectrum. For the resulting spectrum of electrons from heavy-flavour hadron decays a signal-to-background ratio of 1 was observed at $p_t = 2$ GeV/c. This ratio grows with increasing electron p_t up to ≈ 5 at $p_t = 8$ GeV/c. The p_t-differential cross section of electrons from heavy-flavour hadron decays obtained by this method is in good agreement with fixed-order plus next-to-leading logarithm pQCD (FONLL) predictions. The total

charm cross section in proton-proton collisions obtained from this analysis is $\sigma_c = 7.6 \pm 0.3(\text{stat}) \pm 2.9(\text{sys})^{+3.2}_{-2.5}(\text{extr}) \pm 0.3(\text{norm}) \pm 0.3(\text{br})$ mb. Results from this analysis are published in [1].

Zusammenfassung

Im größten Hadronenkollider der Welt, dem Large Hadron Collider (LHC) am CERN, werden Protonen bei einer Schwerpunktsenergie, welche zur Zeit $\sqrt{s} = 8$ TeV beträgt, und Bleikerne bei derzeitig $\sqrt{s_{NN}} = 2.76$ TeV zur Kollision gebracht. Dadurch wird die Tür in einen neuen Energiebereich geöffnet, was die Untersuchung der QCD in elementaren Protonenkollisionen und in der extremen Umgebung von Schwerionenkollisionen erlaubt, und ein Endeckungspotenzial für seltene und exotische Teilchen bereitstellt. ALICE ist das auf Schwerionenkollisionen spezialisierte Experiment am LHC. Das Experiment wurde auf exzellente Teilchenidentifikation und Spurrekonstruktion bei niedrigem p_t optimiert, einem Impulsbereich, in dem sowohl in Proton-Proton als auch in Schwerionenkollisionen die Mehrzahl der Teilchen produziert wird.

Die Produktion schwerer Quarks wird in Protonenkollisionen durch perturbative Quantenchromodynamik (pQCD) in höherer Ordnung beschrieben. Daher kann die Messung der Produktion schwerer Quarks zur Überprüfung perturbativer QCD Rechnungen verwendet werden. Messungen bei niedrigeren Energien am SPS, am RHIC und am Tevatron zeigten gute Übereinstimmung mit pQCD Rechnungen, wobei die Daten typischerweise an der oberen Grenze der theoretischen Vorhersagen lagen. Des weiteren dienen die Messungen in Protonenkollisionen als Referenzbfür Schwerionenkollisionen. Die Produktion schwerer Quarks kann sowohl in hadronischen als auch in semi-leptonischen Zerfallskanälen untersucht werden. Die in dieser Dissertation vorgestellte Analyse, wurde in semi-elektronischen Zerfallskanälen mit dem ALICE Apparat durchgeführt.

Eine bedeutende Komponente zur Elektronenidentifikation ist der Übergangsstrahlungsdetektor (TRD), der einen wichtigen Beitrag zur Elektron-Pion Separation leistet. Das Verhalten der Elektronenidentifikation wurde das erste Mal an echten Daten mit einer auf Daten basierenden Methode überprüft. Der Pionenunterdrückungsfaktor wurde mit einer Likelihoodmethode basierend auf der Ladungsdeposition in der Kammer ermittelt. Bei einem Impuls von 2 GeV/c beträgt der gemessene Pionenunterdrückungsfaktor 23 für Spuren mit der maximalen an Ladungsdepositionsmessungen.

Das inklusive p_t-Spektrum von Elektronen, welches sowohl Beiträge aus Zerfällen von Hadronen mit schweren Quarks als auch Beiträge aus Untergrundquellen enthält, wurde im Transversalimpulsbereich 0.5 GeV/c < p_t < 8 GeV/c in Protonenkollisionen bei $\sqrt{s} = 7$ TeV bei zentraler Rapidität ($|y|$ < 0.5) gemessen. Der Anteil der Untergrundelektronen wurde mit Hilfe einer Cocktailmethode quantifiziert und vom inklusiven Spektrum abgezogen. Für das resultierende p_t-Spektrum von Elektronen aus den

Zerfällen von Hadronen mit schweren Quarks beträgt das Signal-zu-Untergrund Verhältnis 1 bei $p_\mathrm{t} = 2$ GeV/c. Diese Verhältnis steigt mit dem Transversalimpuls der Elektron bis auf ≈ 5 bei $p_\mathrm{t} = 8$ GeV/c. Der gemessene p_t-differenzielle Wirkungsquerschnitt stimmt gut mit FONLL pQCD überein. Der in dieser Analyse bestimmte totale charm Wirkungsquerschnitt beträgt $\sigma_c = 7.6 \pm 0.3(\mathrm{stat}) \pm 2.9(\mathrm{sys})^{+3.2}_{-2.5}(\mathrm{extr}) \pm 0.3(\mathrm{norm}) \pm 0.3(\mathrm{br})$ mb. Resultate aus dieser Dissertation wurden in [1] veröffentlicht.

Contents

List of Figures

1 Introduction

1.1 Physics of high-energy nucleus-nucleus collisions

Nature is governed by four interactions, the strong interaction, the weak interaction, the electromagnetic interaction and gravity. In the early universe, all forces are assumed to be unified in one force. During the expansion the universe cooled down and the forces decoupled. The decoupling of the strong and the electroweak interaction took place at a time of $\approx 10^{-35}$ seconds after the big bang [2].

The theory of strong interaction is *Quantum Chromodynamics* (QCD). Strongly interacting particles are observed as *hadrons*, consisting of quarks and antiquarks. The interaction is mediated by the exchange of gluons. Table 1.1 shows an overview of the different quark flavours. Hadrons are grouped into baryons which contain three quarks or antiquarks, and mesons which contain a quark and an antiquark. A further quantum number introduced by the theory of QCD is called "colour". Three colours *red*, *blue*, and *green* are defined. Hadrons are colour-neutral, which means for baryons each quark carries a different colour and for mesons one quark carries a certain colour and the other one the corresponding anti-colour. An important feature of QCD is that the gauge bosons, the gluons, carry colour themselves [4].

Table 1.1: Overview of the properties of quark flavours down (d), up (u), strange (s), charm (c), bottom (b) and top (t). Quark flavours are grouped into generations consisting of two flavours. The quantities are taken from [3].

	d	u	s	c	b	t
charge	-1/3	+2/3	-1/3	+2/3	-1/3	+2/3
mass (MeV/c²)	4.1 - 5.8	1.7 - 3.3	101^{+29}_{-21}	$1.27^{+0.07}_{-0.09} \times 10^3$	$4.67^{+0.18}_{-0.06} \times 10^3$	$1.72^{+0.013}_{-0.009} \times 10^5$
Isospin	-1/2	+1/2	0	0	0	0
Strangeness	0	0	-1	0	0	0
Charm	0	0	0	1	0	0
Bottom	0	0	0	0	-1	0
Top	0	0	0	0	0	1

A remarkable property of QCD is that the coupling constant depends on the momentum transfer q. The coupling constant α_s can be calculated [4] as

$$\alpha_s(q) = \frac{4\pi}{(11 - \frac{2}{3}N_f)\ln(\frac{q^2}{\Lambda^2})} \tag{1.1}$$

with the number of quark flavours N_f and the QCD scale parameter Λ which is $\approx$ 200 MeV. At small momentum transfer or large distance the coupling constant is large. Towards higher momentum transfer q or smaller distances, the coupling constant decreases. In this region the coupling is weak enough that the quarks can be considered as asymptotically free particles, such that QCD can be handled with perturbative methods.

The state of matter can be divided into *phases*, depending on conditions like temperature, pressure, chemical potential. Within a certain phase, physical properties of the material stay similar while at the phase transition, turning from one phase into another, they might change drastically [5]. For strongly interacting matter, QCD calculations on a discretized space-time lattice (*lattice QCD*) predict a phase transition [6] from the hadronic phase to a deconfined phase, called *Quark-Gluon Plasma* (QGP), when crossing a "critical temperature" T_c ($\approx$ 160 MeV): considering the ratio of the energy density ϵ and T^4, shown in Figure 1.1 (left), a strong increase of ϵ/T^4 in the region of the critical temperature is seen, while, within the phases the increase is much weaker or the ratio stays constant. A second observable is
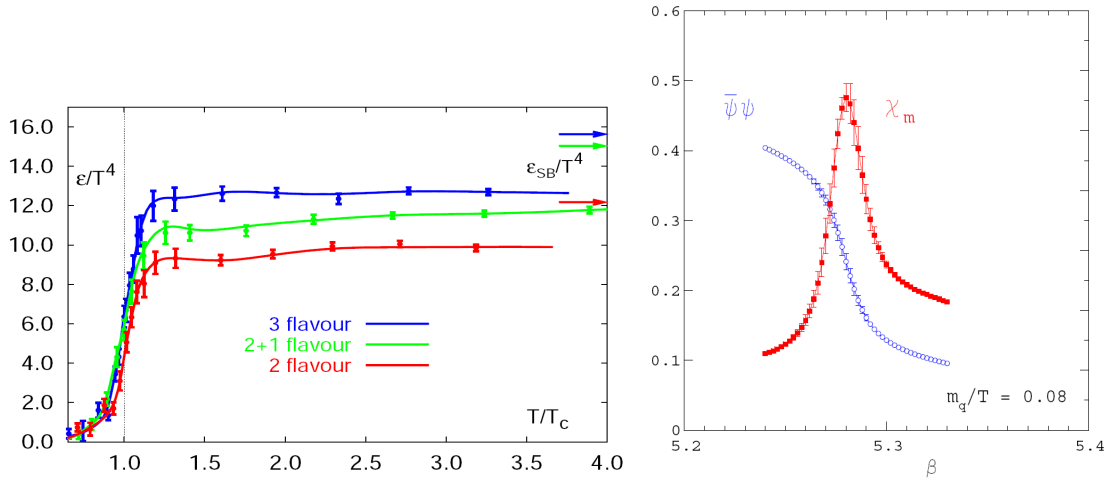
Figure 1.1: Energy density and chiral condensate as function of the temperature. The left plot shows the energy density ϵ/T^4 as function of the temperature for different quark numbers derived from lattice QCD calculations (figure taken from [6]). On the right plot (taken from [6]), the chiral condensate (blue) and the chiral susceptibility (red) versus the lattice coupling β, which is linked to the temperature, is shown. The maximum in the chiral susceptibility indicates the phase transition.
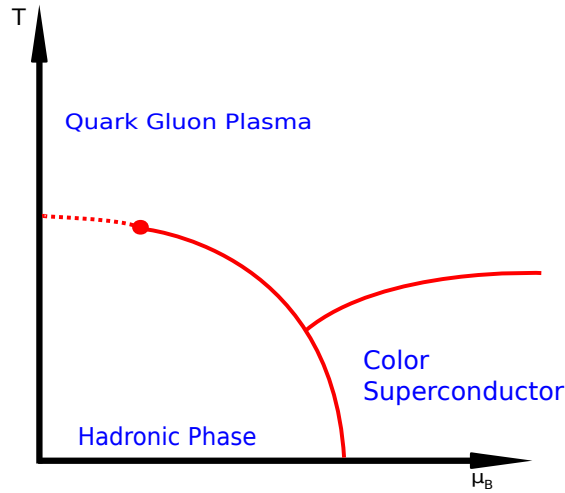
Figure 1.2: Sketch of the QCD phase diagram (based on [5, 8, 9]): At low temperature T and low baryochemical potential μ_B matter is in the hadronic phase. Increasing the temperature a phase transition to a different phase, the Quark-Gluon Plasma, sets in. At low μ_B the phase transition is expected to be a crossover transition (dashed line), which at higher μ_B may become a first order phase transition with a critical point in between. At high μ_B and low T several color superconducting phases are expected.

the chiral condensate, which is the order parameter for chiral symmetry breaking [7]. A non-vanishing chiral condensate indicates chiral-symmetry breaking. The chiral condensate drops when exceeding the critical temperature T_c, which means that chiral symmetry is restored. Chiral symmetry restoration is indicated in Figure 1.1 (right): the chiral condensate (blue) decreases with increasing temperature, and the slope has its maximum at the phase transition, where the chiral susceptibility, which is the partial derivative of the chiral condensate with respect to the quark mass, is largest.

Taking the temperature and the baryochemical potential as free parameters, a phase diagram for QCD can be drawn [5]. Figure 1.2 shows a sketch of the QCD phase diagram. At low temperature and low μ_B, matter is in the hadronic phase. When increasing temperature or μ_B, the phase transition to the Quark-Gluon Plasma takes place. The order of the phase transition between the hadronic and the QGP phase depends on the number of quark flavours and the quark masses [7]: with three quarks up, down and strange, where the masses of up and down are very small and the strange quark mass is $\approx$ 150 MeV, the phase transition is a crossover transition at low-μ_B [10] and possibly a first order phase transition at higher μ_B with a critical point where type of the phase transitions changes [5, 9] [1]. The

---

[1]   As discussed in [5] the phase transition mentioned here is based on lattice QCD calculation which indicate a crossover phase transition at $\mu_B = 0$. Other scenarios are under discussion [8].

search for the critical point is part of the *Relativistic Heavy Ion Collider* (RHIC)[2] energy scan program [11–13] as well as the CBM program at the future FAIR facility at GSI[14]. Towards higher μ_B several colour-superconducting phases are expected[3].

Relativistic heavy-ion collisions, in which sufficient temperatures or densities for the phase transition can be achieved, are a unique tool to study the Quark-Gluon Plasma experimentally. The first observation was done at the *Super Proton Synchrotron* (SPS)[4] with the heavy-ion programme [16]. At the RHIC, this observation was confirmed, and the first detailed studies of several signatures of the QGP were done [17]. The studies are taken up at the *Large Hadron Collider*(LHC), where even higher temperatures are reached. At the LHC also the study of harder probes (high-p_t particles beyond 20 GeV/c [18], jets [19, 20], W [21, 22] and Z [23, 24] bosons) becomes possible. In addition, the medium produced at the LHC has a larger volume and a longer lifetime [25].

Properties of the medium produced can be studied when comparing measured observables in heavy-ion collisions to the ones measured in *proton-proton* (pp) collisions at the same centre-of-mass energy. For hard probes, which are produced at the initial stage of the collisions, results of the observables should be a superposition of nucleon-nucleon collisions, in case there would be no medium effect. This is called *binary collision scaling*. Soft processes, like low-p_t particle production, are expeceted to scale with the *number of participating nucleons* [26], which is related to the overlap volume. The number of binary collisions is not directly accessible experimentally but has to be obtained using the *Glauber model* [27]. For this, collisions are divided into centrality classes. Centrality classes describe the overlap of the nuclei in the collision, with the most central collisions having the largest overlap and the most peripheral collisions having the smallest overlap. For each centrality class the mean number of binary collisions can be calculated using the Glauber model[5]. The most central collisions have the largest number of binary collisions. As observable to quantify medium effects the *nuclear modification factor R_{AA}* is defined as

$$R_{AA} = \frac{1}{N_{coll}} \frac{\frac{d^2 N_{AA}}{dp_t dy}}{\frac{d^2 N_{pp}}{dp_t dy}} \tag{1.2}$$

Here $d^2 N_{AA}/(dp_t dy)$ and $d^2 N_p/(dp_t dy)$ are the yields in A-A respectively pp collisions, and $< N_{coll} >$ is the average number of binary collisions, which is connected to the nuclear overlap function T_{AB}. Without

---

[2]   at Brookhaven National Laboratory (BNL)
[3]   for more information see [15]
[4]   at CERN, Geneva, Switzerland
[5]   for example see [28]
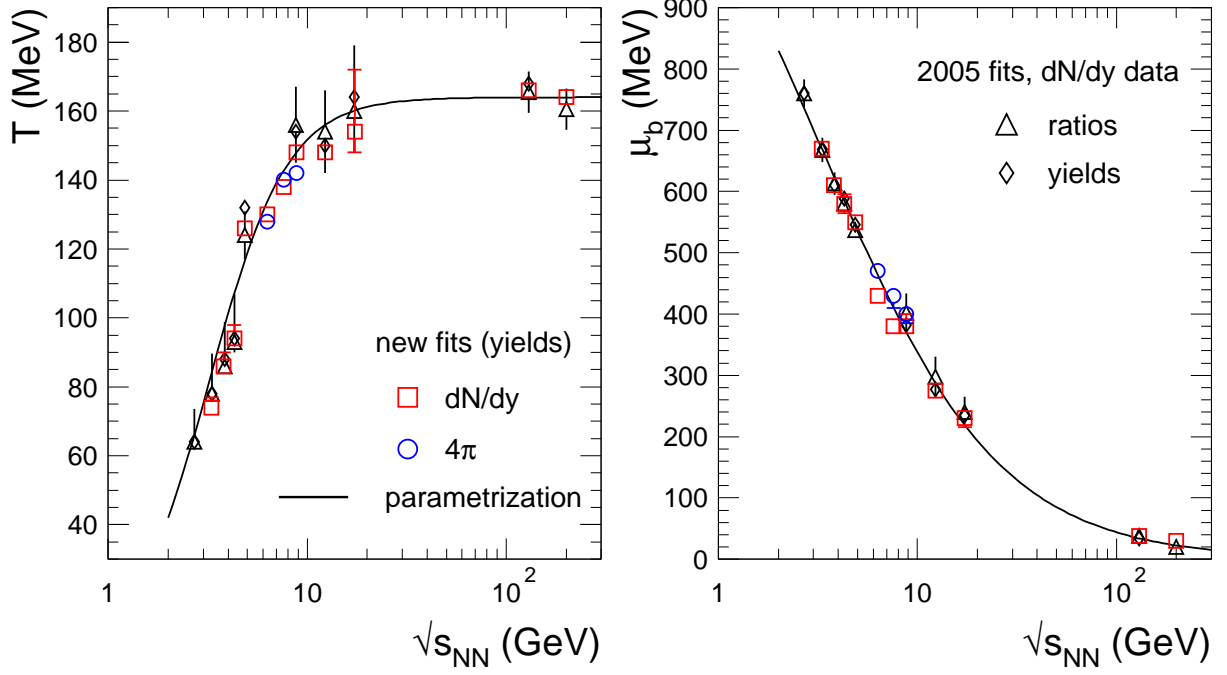
Figure 1.3: Freeze-out temperature and baryochemical potential as function of the centre-of-mass energy per nucleon $\sqrt{s_{NN}}$ (both plots taken from [37]): the points are derived from fits of the thermal model to particle ratios measured at different energies. Black lines indicate a parameterisation used to describe the $\sqrt{s_{NN}}$-dependence of the temperature([38]) and the baryochemical potential([39]).

modification by the medium, R_{AA} is expected to be 1 in the region where binary collision scaling is applicable. For example, photons produced in initial hard scattering processes do not interact via the strong interaction, so they are not expected to be influenced by the medium and the nuclear modification factor is expected to be 1. This has been verified experimentally at RHIC by PHENIX[6] [29] for $p_t < 14$ GeV/c, and at LHC by CMS[7] [30] for high-energy photons with E_t beyond 20 GeV. In case R_{AA} is below 1, the effect is called suppression. Considering charged hadron production, a suppression of high-p_t charged particles is seen at RHIC [31–34] and at LHC [18, 35, 36][8]. The suppression is interpreted as energy loss of the parton travelling through the medium before hadronisation.

When the Quark-Gluon Plasma expands, it cools down until the transition to the hadronic phase is reached (after $\approx 10^{-22}$s [40]). Due to confinement in the hadronic phase, quarks liberated in the QGP form hadrons. The number of hadrons of a given species is determined at the *chemical freeze out*. At the chemical freeze-out the inelastic collisions between particles stop so that the particle composition is not changed anymore [5]. With the help of the statistical model [41], the freeze out temperature

---

[6] Pioneering High Energy Nuclear Interactions eXperiment
[7] Compact Muon Solenoid
[8] In [36] the R_{CP}, which compares different centrality classes, is reported instead of the R_{AA}. The same applies also to the ATLAS[9] publications [24].

and the baryochemical potential can be determined from measured hadron ratios. Particle ratios and absolute yield from heavy-ion collisions were studied at the *Schwerionensynchrotron* (SIS)[10] [42], at the *Alternating Gradient Synchrotron* (AGS)[11], at the SPS and at RHIC [37, 38]. Here one has to consider that the initial temperature at SIS or AGS is possibly not high enough to provide a phase transition, even though the baryochemical potential is larger than at SPS, RHIC, or LHC. From the study of the particle yields a dependence of the freeze out temperature and the baryochemical potential on the centre-of-mass energy per nucleon pair $\sqrt{s_{NN}}$ is derived. This is shown in Figure 1.3. It turns out that with increasing $\sqrt{s_{NN}}$ the temperature increases until a saturation at ≈ 164 MeV at the top SPS energy ($\sqrt{s_{NN}} = 17.3$ GeV), and the baryochemical potential decreases. Based on the $\sqrt{s_{NN}}$ dependence of T and μ_B, the freeze out conditions for LHC can be predicted[43] to T ≈ 164 MeV and $\mu_B \approx 1$ MeV, which is approximately the condition of the early universe.

1.2 Physics with heavy quarks

The charm quark was discovered in 1974 by two groups independently: as a narrow resonance at a dielectron invariant mass of 3.1 GeV/c^2 in e^+e^-- collisions at the Stanford Linear Accelerator (SLAC) [44], and in a fixed target experiment with a proton beam on a beryllium target at the Brookhaven National Laboratory (BNL)[45]. The observed resonance is a bound state of a charm and an anticharm quark, which is called J/ψ. In 1977, the bottom quark was discovered as a narrow resonance at an invariant mass of 9.5 GeV/c^2 in the dimuon invariant mass spectrum measured in a fixed target experiment with a proton beam on a beryllium and a platinum target at the Fermi National Laboratory (FNAL) [46]. This resonance can be identified as a bound state of a bottom and an antibottom quark, called Υ.

The study of heavy-flavour production is of interest both in proton-proton and in heavy-ion collisions. Due to the large mass of b and c quarks, the production of heavy flavour can be described by applying perturbative QCD. Figure 1.4 shows the charm and bottom production cross section in pp collisions as a function of $\sqrt{s}$ calculated with MNR[12], a *next-to-leading order* (NLO) *perturbative QCD* (pQCD) model describing heavy quark production [47, 48]. In the calculation the masses are assumed to be 1.2 GeV/c^2 for the charm quark and 4.75 GeV/c^2 for the bottom quark. LHAPDF [49] is used as parton density function and Peterson fragmentation as fragmentation function [50]. Going from RHIC to LHC energies, for bottom a stronger increase in the cross section is visible than for charm. At 200 GeV the cross section

---

[10] at GSI, Darmstadt, Germany
[11] at Brookhaven National Laboratory (BNL)
[12] The model is named according to the authors Mangano-Ridolfi-Nason.
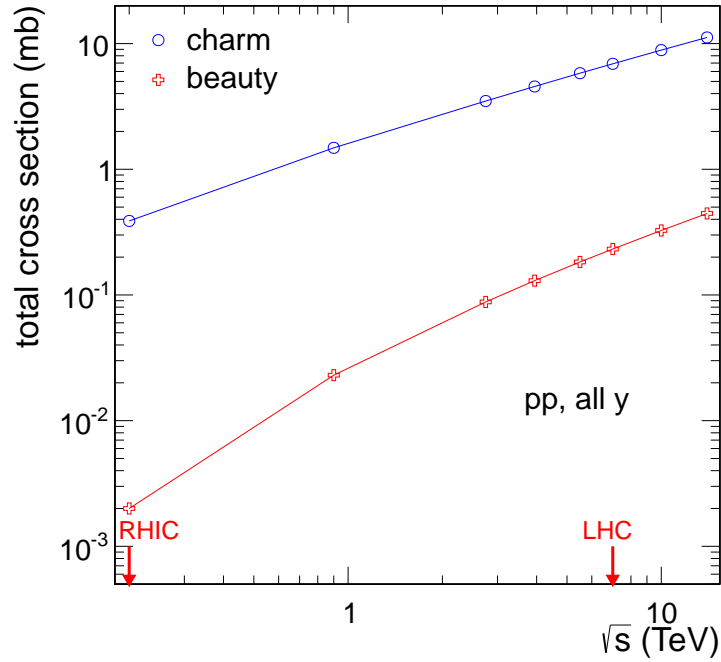
Figure 1.4: Calculated cross sections for charm (blue) and bottom (red) production in proton-proton collisions as function $\sqrt{s}$ [47, 48]: at $\sqrt{s}$ = 7 TeV the cross section for charm production is 6.9 mb and for bottom production it is 0.2 mb. The calculation is based on next-to-leading order perturbative QCD (MNR).

for charm production is a factor ≈200 higher than for bottom, while at 7 TeV the factor is about 30. In addition, at $\sqrt{s}$ = 7 TeV the bottom production cross section is comparable to the charm cross section at RHIC. More recent predictions extend NLO calculations by a resummation of logarithms of p_t/m at next-to-leading-logarithmic accuracy [51], performed in two "schemes" *FONLL*[13] [52] and *GM-VFNS*[14] [53].

In addition to tests of pQCD, heavy-flavour measurements in proton-proton collisions are of interest in relation to heavy-ion collisions since they provide reference distributions for the study of the nuclear modification factor.

In heavy-ion collisions, the study of heavy quarks can be used to test the energy loss of heavy partons while passing through the hot and dense medium [54]. Partons propagating through the medium loose energy by radiating gluons and by collisions with other partons. However, in forward direction in a cone with the opening angle ϕ the radiation is suppressed. This is called the "dead cone effect" [55]. The angle ϕ increases with increasing parton mass. For heavy quarks the cone angle would be larger and so the radiative energy loss in the medium was predicted to be smaller than the radiative energy loss of light

---

[13] Fixed Order plus Next-to-Leading-Logarithms
[14] General-mass variable-flavour-number scheme
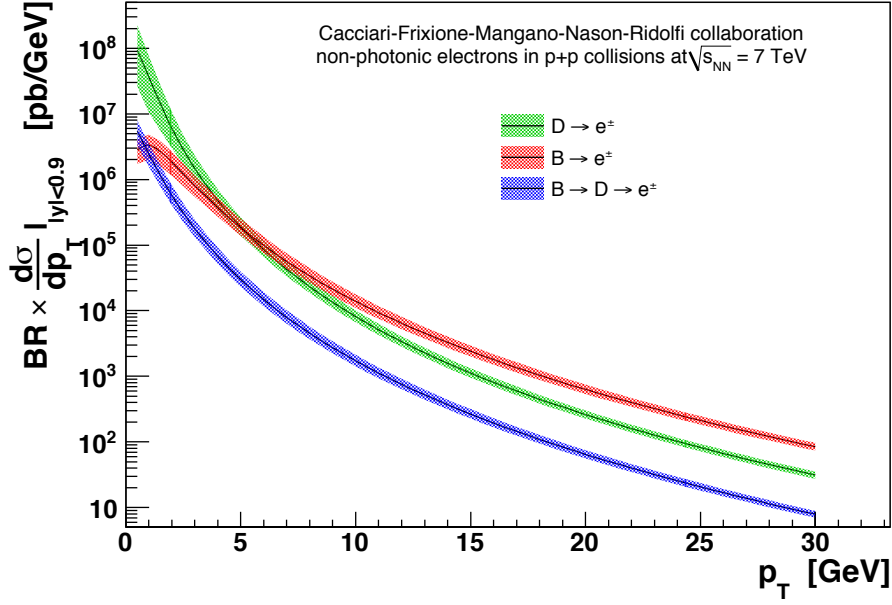
Figure 1.5: Predicted differential cross section as function of p_t of electrons from heavy-flavour hadron decays calculated with FONLL [52, 56], multiplied with the branching ratio into electrons ($\approx 10\%$). Contributions from charm or bottom hadron decays into electrons and the decay from bottom hadrons into charm hadrons, which then further decay into electrons are shown separately. In the p_t region between 3 and 6 GeV/c, the bottom component is of the same order as the charm component, and for higher p_t the decays of bottom hadrons into electron become dominant.

quarks, and the one of bottom quarks should be smaller than the one of charm quarks. This expectation has already been challenged by PHENIX results as discussed later in this section.

Open-charm production can be studied either by fully reconstructing the decay of charmed hadrons in hadronic channels (i.e. $D^0 \rightarrow K^- \pi^+$), or via an inclusive measurement of electrons or muons coming from heavy-flavour hadron decays. All three methods have to deal with large background especially at low-p_t, either combinatorial background in the reconstruction of the charmed mesons or in the semi-leptonic channels background from other electron or muon sources. Measurements in the hadronic channels allow a direct estimate of the charm cross section. However a measurement at low-p_t which on the one hand contains the largest part of the cross section, remains challenging due to large background, especially in heavy-ion collisions. In the semi-leptonic channels, the neutrino prevents the full reconstruction of open heavy-flavour hadrons, so measurements have to be performed as inclusive ones over all contributing channels. Figure 1.5 shows the differential cross section as function of p_t of electrons from charmed and bottom hadron decays in pp collisions at $\sqrt{s} = 7$ TeV predicted by FONLL. The prediction, referred to as "central value" in the following, uses the renomalization scale $\mu = p_t$, and $m_c = 1.5$ GeV/c^2 and $m_b = 4.75$ GeV/c^2 for the charm and bottom quark mass. To obtain a systematic uncertainty, the

renormalization scale and the charm and bottom quark mass are varied. Based on this, theoretical limits on the differential cross section can be derived. Also, in this calculation CTEQ6.6 [57] is used as parton density function. The uncertainty of the prediction in the low p_t-range is substantial and almost reaches a factor 2 between the central value and the limits of the prediction. In the region below 3 GeV/c, the decay of charm hadrons into electrons is the dominating contribution. For p_t between 3 and 6 GeV/c, both charm and bottom hadron decays into electrons are of the same order, and for higher p_t, due to the harder p_t-spectrum of electrons produced in semi-leptonic bottom decays, the bottom component becomes dominating. Due to the longer lifetime of bottom hadrons (c$\tau \approx$ 500 μm, compared to c$\tau \approx$ 100 μm for charm hadrons [3]), a separation is possible using displaced vertices to identify the bottom component. Using single-electron channels, also heavy-flavour measurements in the p_t-range below 1 GeV/c are possible.

At RHIC, heavy flavour measurements in pp collisions at $\sqrt{s}$ = 200 GeV are mainly performed in the semi-electronic channel at midrapidity by PHENIX [58, 59] ($|\eta|$ < 0.35) and STAR [15] [60–62] ($|\eta|$ < 0.7). Figure 1.6a shows the differential cross section of electrons from heavy-flavour hadron decays measured with PHENIX compared to FONLL [59]. For both collaborations the measurements lay at the upper limit of the FONLL predictions, however they are still compatible with the prediction within experimental and theoretical uncertainty. Using angular correlations between electrons from heavy-flavour hadron decays and the daughter tracks in the hadronic decay channel, STAR [62] separated the charm and bottom contribution to the inclusive heavy-flavour electron p_t spectrum. The method makes use of differences in the angular distribution between the electrons from heavy-flavour hadron decays and the associated hadrons for charm and bottom. This allows to obtain the relative fraction of electrons from B-hadron decays by a simultaneous fit of template distributions derived from *PYTHIA* simulations to the measured one (for more information see [64, 65]). The resulting $d\sigma/dp_t$ of electrons from bottom hadron decays is compatible with the centre of the FONLL prediction. A complementary measurement by PHENIX [66] confirms this observation, however with larger uncertainty. Instead of using angular correlations, differences in the invariant mass distributions of the electron-hadron pair for charm and bottom are used to disentangle the contributions. Measurements in the semi-muonic decay channels are performed by PHENIX at forward rapidity (1.5 < η < 1.8) in the p_t range 1 GeV/c < p_t < 3 GeV/c [67]. In this measurement the results are above FONLL predictions, with large systematic uncertainties.

In heavy-ion collisions, both PHENIX and STAR measure heavy flavour in the semi-electronic channel. In PHENIX the nuclear modification factor and the elliptic flow are measured for Au–Au collisions at

---

[15]   Solonoidal Tracker At RHIC

(a) p_t spectrum of electrons from heavy-flavour hadron decays in pp collisions

(b) Nuclear modification factor and elliptic flow v_2 of electrons from heavy-flavour hadron decays in the most central Au–Au collisions
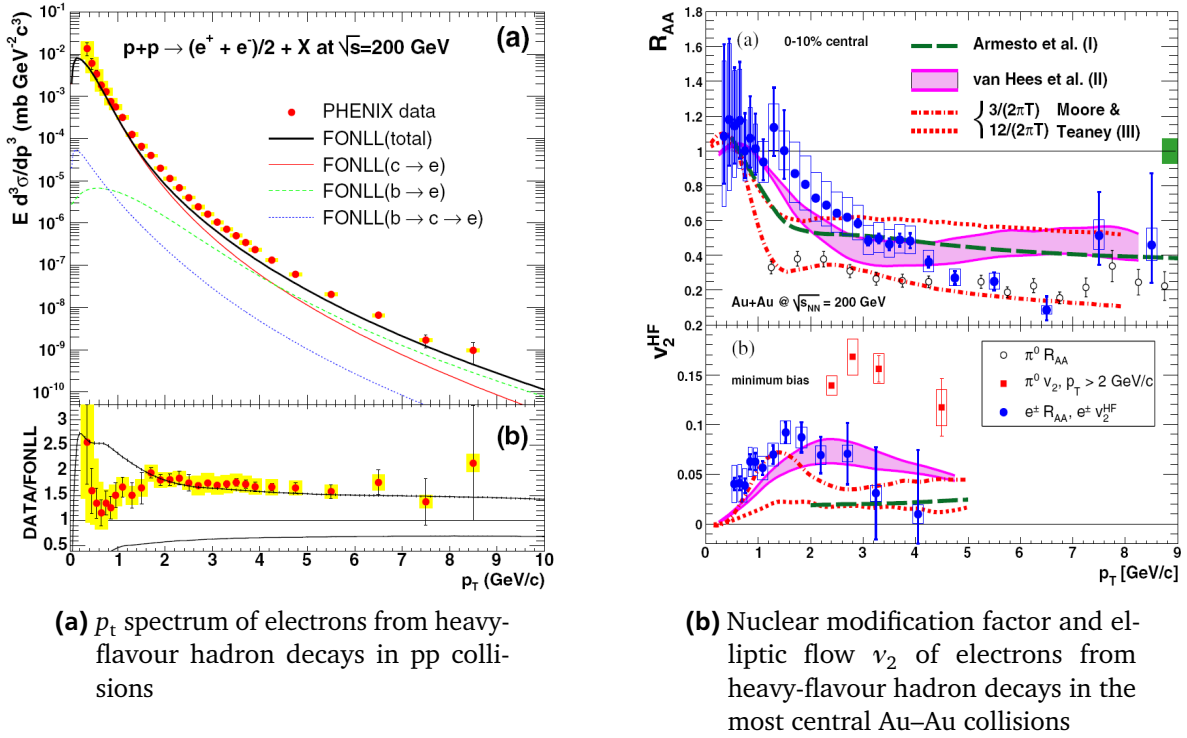
Figure 1.6: PHENIX heavy-flavour measurements in the semi-electronic channels at RHIC: in Fig. (a) the differential cross section of electrons from heavy flavour decays in pp collisions [59] is compared to FONLL. The measured cross section is at the upper limit of the prediction. In Fig. (b) the nuclear modification factor of electrons from heavy-flavour hadron decays in centralAu–Au collisions and the elliptic flow v_2 in minimum bias collisions as function of p_t are shown [63]. The suppression is smaller than for π^0 at low-p_t. The non-zero elliptic flow indicates that charm quarks might thermalise with the medium.

$\sqrt{s_{NN}}$ = 200 GeV [63]. Figure 1.6b shows the nuclearmodification factor in central Au–Au collisions and the elliptic flow in minimum bias collisions as function of p_t. A suppression is seen in the most central collisions for p_t above 2 GeV/c which indicates energy loss of the heavy quark in the hot dense matter. The suppression is weaker than the one observed for π^0 in the p_t region between 2 and 5 GeV/c. Above 5 GeV/c the same suppression is seen as for π^0.

Comparisons to models including only radiative energy loss indicate that this contribution is not enough to explain the suppression experimentally observed. Taking into account also collisional energy loss results in a better agreement with the measured data [68]. However, in the p_t-region where the bottom becomes relevant, the results are still a challenge for the radiative and collisional energy loss models. The *nuclear modification factor R_{AA}* of electrons from heavy flavour decays could also be affected by the modification of the baryon to meson ratio in heavy-ion collisions. Since the branching ratio of Λ_C to electrons is smaller than that of D mesons to electrons [69–71], an enhanced Λ_C/D ratio would lead

to a smaller yield of electrons from heavy flavour decays which would show up as a larger suppression. In addition, a non-zero elliptic flow indicates that the charm quarks might thermalise with the medium.

At the Tevatron[16], CDF[17] measured the charm production cross section in $p\bar{p}$ collisions at $\sqrt{s} = 1.96$ TeV via the reconstruction of charmed hadrons in hadronic decay channels [72]. The measurement was done in the channels $D^0 \rightarrow K^- \pi^+$, $D^{*+} \rightarrow D^0 \pi^+$, $D^+ \rightarrow K^- \pi^+ \pi^+$, and $D_s^+ \rightarrow \Phi \pi^+$. The data are at the upper limit of the predictions. Tevatron experiments had a rich bottom program. In Run I, done at $\sqrt{s} = 1.8$ TeV, CDF measured the cross section of bottom production via the hadrons B^+ (in the channel $B^+ \rightarrow J/\psi K^+$) and B^0 (in the channel $B^0 \rightarrow J/\psi K^*$). Compared to NLO pQCD, the measured cross section was observed to be a factor 3 higher [73][18]. Also data from the D0 experiment in the dimuon channel show an excess compared to theory [74]. In RUN II, the Tevatron experiments were upgraded by new silicon vertex detectors which allowed to trigger on displaced vertices[75]. CDF measured the bottom cross section via the decay of bottom hadrons into J/ψ [76]. These results are in good agreement with the central value of the FONLL calculations.

At the LHC, the production of open charm in pp collisions is studied with *ALICE* (A Large Ion Collider Experiment) via the reconstruction of the hadronic channels $D^0 \rightarrow K^- \pi^+$, $D^+ \rightarrow K^- \pi^+ \pi^+$, $D^{*+} \rightarrow D^0 \pi^+$ (all [77]), and $D_s^+ \rightarrow K^+ K^- \pi^+$ [78]. Measurements of the Λ_C in the channels $\Lambda_C \rightarrow pK^- \pi^+$ and $\Lambda_C \rightarrow \bar{K}_S^0 p$ are in preparation [79]. Figure 1.7 (left) shows the differential cross section of D^0 production in pp collisions at $\sqrt{s} = 7$ TeV. Compared to FONLL, the differential cross section is at the upper limit of the prediction, and compared to GM-VFNS the it is at the lower limit [77]. The same behaviour is observed for the other charmed mesons. In Pb–Pb collisions at $\sqrt{s_{NN}} = 2.76$ TeV, first measurements are done for D^0, D^+, and D_s^+ [80]. The average of the R_{AA} for the three hadron species can be compared to R_{AA} for charged hadrons. The R_{AA} for the D-Mesons appears to be slightly higher than the one of the charged hadrons. However, within the systematic uncertainties, both are still compatible over the full p_t-range. In addition, the R_{AA} of B-Mesons, obtained from non-promt J/ψ decays by CMS [81], is slightly, but not yet significantly, higher than the ones of charged hadrons and D meson, which is a slight indication of the mass ordering of the R_{AA} as discussed above. Further measurements are needed to make a conclusive statement.

In the semi-muonic decay channel, measurements are done by ALICE at forward rapidity ($-4 < \eta < -2.5$) in the p_t-range 2 GeV/c < p_t < 10 GeV/c [82] as well as by ATLAS at midrapidity ($\eta < 2.5$) in the

---

[16] At Fermi National Laboratory, Illinois, USA
[17] Collider Detector at Fermilab
[18] An overview of the developments both in the experiments and on the theory to explain the excess of the bottom hadrons can be found in [51]
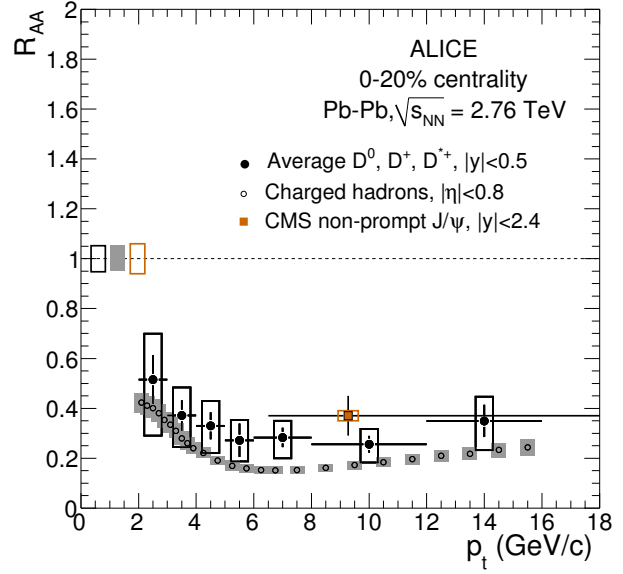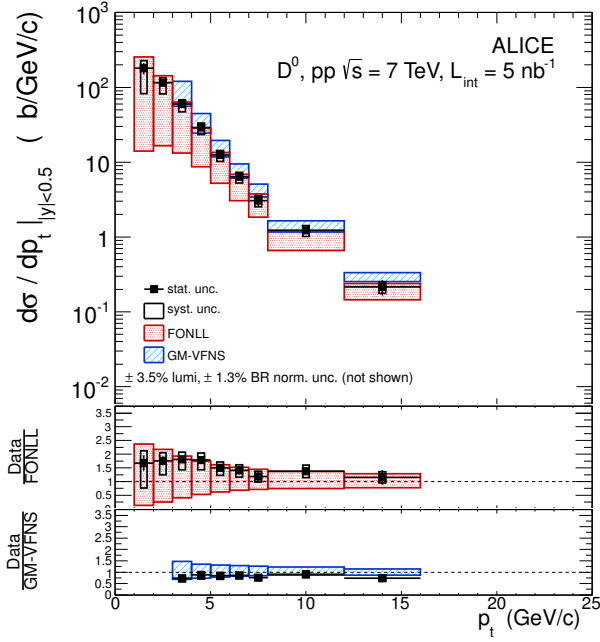
Figure 1.7: Left: D^0 differential cross section as function of p_t measured with ALICE [77] in pp collisions. The differential cross section is at the upper limit of the prediction when comparing to FONLL and at the lower limit of the prediction when comparing to GM-VFNS pQCD calculations. Right: nuclear modification factor of D mesons in central Pb–Pb collisions compared to the nuclear modification factor of charged hadrons [80].

range 7 GeV/c < p_t < 26 GeV/c [83]. Both measurements are in agreement with FONLL predictions. The data from ALICE are at the upper limit of the prediction.

For the semi-electronic decay channel, ATLAS provides a measurement at midrapidity ($|y|$ < 2 excluding 1.37 < $|y|$ < 1.52) in the p_t-range between 7 and 26 GeV/c [83]. In this p_t-region, bottom gives the dominant contribution. Data is in good agreement with the FONLL predictions. The measurement done by ALICE extends the p_t-range covered by ATLAS towards lower p_t, where the dominant fraction of the cross section, especially for charm, resides. Results of this are the subject of this thesis and are discussed in chapter 4.

1.3 ALICE at the LHC

ALICE is one of the four large experiments at LHC besides ATLAS, CMS and LHCb[19]. In contrast to the other experiments, the main focus of ALICE is the investigation of heavy-ion collisions. Therefore, ALICE is designed to cope with high track multiplicities up to 20000 tracks per event, down to a p_t of 100 MeV/c [84]. In order to be able to reconstruct low momentum tracks, the magnetic field of 0.5 T is lower than compared to the other experiments (4 T in CMS [85], 2 T in ATLAS in the central detectors [86]).

---

[19]   LHC beauty
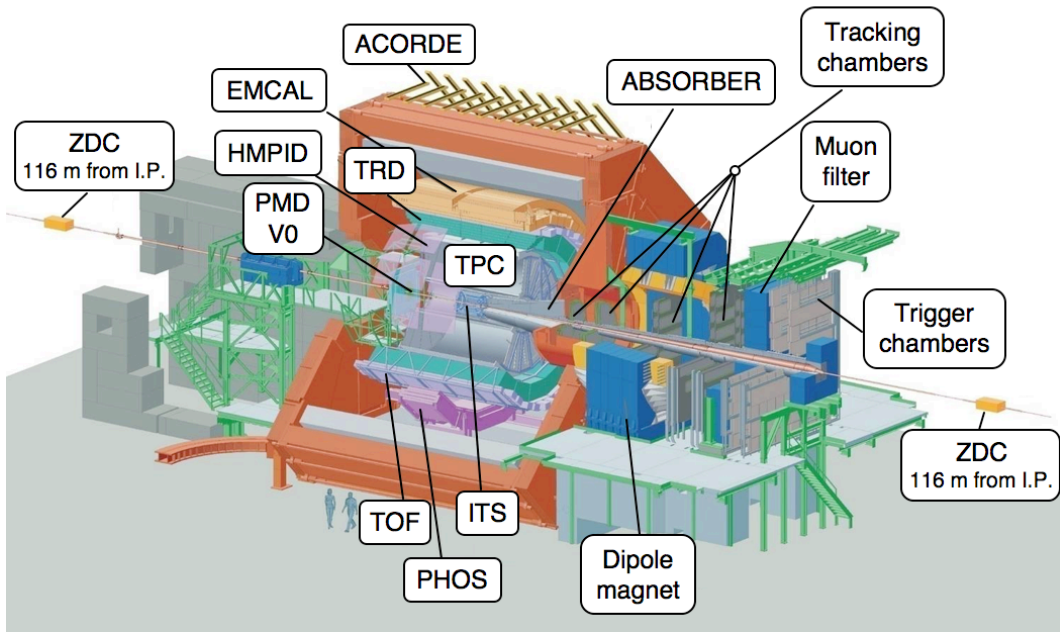
Figure 1.8: Sketch of ALICE (picture taken from [84]): the experiment consists of several detectors for triggering, tracking and particle identification. Detectors located around midrapidity are called central barrel detectors. These detectors are inside a solenoid magnet (red) providing a field of 0.5 T. A muon spectrometer is used for muon measurements at forward rapidity (-4.0 < y < 2.5).

Particle identification in ALICE is optimized to have an excellent separation of kaons, pions, protons, and electrons over a large p_t range. A good track-to-vertex impact parameter resolution is needed to select primary tracks. In addition, it plays an important role in the separation of the components from charm and bottom in the heavy-flavour measurements.

Figure 1.8 shows an schematic representation of the experiment. The spectrometer is separated into a "central barrel" ($|\eta| < 0.9$) and a muon spectrometer used for muon identification at forward rapidity (-4.0 < y < -2.5). The main tracking detectors in ALICE are the *Time Projection Chamber* (TPC) and the *Inner Tracking System* (ITS).

The TPC, with a volume of 90 m^3 the largest gas-filled TPC in the world, is a cylindrical drift chamber with an inner radius of 85 cm and an outer radius of 2.5 m. The TPC has a length of 5 m. The central electrode is placed at $\eta = 0$. As drift gas a mixture of Ne (85.7%), CO_2 (9.5%), and N_2 (4.8%) is used [87]. Charged particles passing the TPC ionise the drift gas and produce electron clusters which travel through the drift field towards the cathode pad plane where the signal is amplified and read out. In total, the TPC has 557568 readout pads [87] organised in 159 rows in radial direction. In all pad rows, space points are reconstructed using the radial and azimuthal position of pads having a signal, and the drift time in beam direction multiplied with the drift velocity as coordinates. These space points, called *clusters*
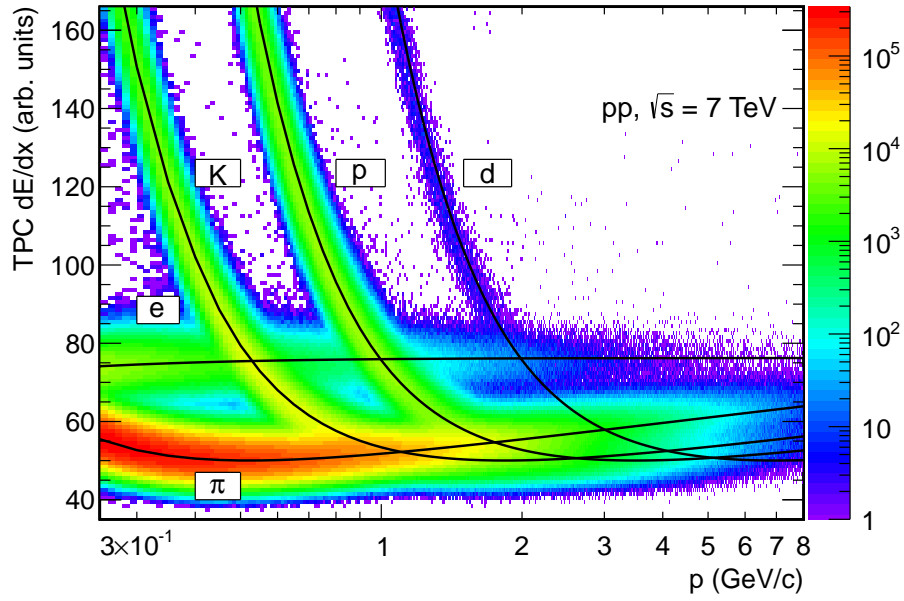
Figure 1.9: Energy loss in the TPC as function of the momentum (Figure taken from [1]): lines indicate the energy loss expected by the Bethe-Bloch formula [89] for electrons, pions, kaons, protons and deuterons.

[20], are used to reconstruct charged particle tracks. The number of rows providing clusters depends on the pseudorapidity coverage: for $|\eta| < 0.9$ all rows can contribute, which leads to a maximum number of clusters of 159. Towards higher η, the number of clusters which can be found for tracks decreases, because the outer pad rows cannot contribute anymore. At $\eta \approx \pm 1.5$ the number of clusters for tracks is at the minimum of 30 clusters, which is the minimum number of clusters required for track reconstruction. The total drift time from the central electrode to the pad plane is 94 μs for a nominal drift field of 400 V/m, sampled in 1000 time steps [88]. The measurement of the ionisation energy loss is used to identify particles, especially kaons, protons and pions [87]. Figure 1.9 shows the energy loss distribution in the TPC. Hadron identification is possible over a large p-range. In momentum regions where the energy-loss distributions of several species cross (indicated as the crossing of the lines showing the expected energy loss calculated by the Bethe-Bloch formula [89]), information from other detectors is needed. As discussed in section 3.3, the TPC energy loss is also used to separate electrons from hadrons.

The ITS is the detector in ALICE closest to the interaction point. As innermost detector the main task is high precision tracking towards the interaction point, for which it needs high granularity in azimuthal and in beam direction. The detector consists of six layers, divided into three subsystems, each with two

---

[20] The signal of a space point is spread over several pads in azimuthal direction as well as several time sample. For one space point three pads in azimuth and three time bins are used. A gaussian distribution of the charge deposit is assumed to calculate the cluster position.

layers: The *Silicon Pixel Detector* (SPD) is the innermost of the ITS subsystems. To provide a precise vertex position, the SPD is the ITS detector with the highest granularity: the innermost of the two SPD layers has $\approx$ 3.3 million pixels, the outer one $\approx$ 6.6 million [84]. Hits in the two SPD layers can be combined to tracklets, which can be used to determine the primary vertex or to measure track multiplicity [90]. Surrounding the SPD, two layers of the *Silicon Drift Detector* (SDD) are placed, with $\approx$ 43k channels in the first layer and $\approx$ 90k channels in the second layer [84]. The drift time is 4.3 to 6.3 μs, sampled with a frequency of 40 MHz [91]. The outermost of the ITS detectors is the *Silicon Strip Detector* (SSD). The SSD has a granularity of $\approx$ 1.1 million strips in the inner and 1.5 million strips in the outer layer [84]. The ITS provides particle identification for low-momentum tracks via their ionisation energy loss in the SDD and the SSD. Charged particles passing the detector layers produce electron-hole pairs, which travel through the electric field applied and produce a measurable current. The amount of electron-hole pairs produced by a charged particle is dependent on the energy deposit.

Track candidates are found in the TPC and are extrapolated towards the vertex using the hits in the six ITS layers which are associated with the tracks. The vertex is either reconstructed using tracks or tracklets in the SPD. In addition to the track candidates already found, a stand alone algorithm in the ITS reconstructs the trajectories of low-momentum particles which do not reach the TPC due to curling in the magnetic field. Track candidates are then extrapolated to the outer detectors via a Kalman filter algorithm [92], where the *Transition Radiation Detector* (TRD), discussed in detail in chapter 2, can contribute to the momentum measurement, in particular at high p_t. Using all central barrel detectors, a p_t resolution of 10% at 100 GeV/c can be reached [93].

Outside of the TRD, at a distance of 3.7 m from the interaction point, the *Time-Of-Flight* (TOF) *detector* is used to separate kaons (up to 1.5 GeV/c) and protons (up to 3 GeV/c) from pions and electrons via a time-of-flight measurement. Due to the mass difference, the heavier kaons and protons have a lower velocity β in contrast to electrons and pions and, therefore, a larger time of flight. For this a precise time-of-flight measurement with a resolution of $\approx$ 160 ps is important. With increasing momentum kaons and protons become indistinguishable in the TOF. The measurement is done using *Multigap Resistive Plate Chambers*(MRPC) [91], gas chambers with a stack of glass plates separated by gaps of 250 μm which are operated at high voltage (HV = 13 kV [94]). Charged particles passing the chamber ionise the gas and introduce a charge on the electrodes. Due to the gap thickness of 250 μm the drift time can be neglected. The use of glass plates as resistors suppresses sparks between the electrodes and allows the chamber to be operated at high efficiency. The time-of-flight is determined as the time measurement in the TOF compared to the time of the collision which can either be determined from the tracks having a

TOF-signal under the assumption of the pion mass or with the *T0* detector which is located close to the collision point in beam direction. In case both methods do not provide a starting time, this information is taken from the time information of the bunch crossing provided by the LHC.

Two electromagnetic calorimeters, the *ElectroMagnetic CALorimeter* (EMCAL) and the *PHOton Spectrometer* (PHOS), are used to identify photons via energy deposit and shower shape. The calorimeters provide a limited coverage in azimuth (EMCAL: $\Delta\phi < 107^{\circ}$ [95], PHOS: $\Delta\phi < 100^{\circ}$ [96]). Also in η the coverage is reduced with respect to the other central barrel detectors (EMCAL: $|\eta| < 0.7$, PHOS: $|\eta| < 0.12$). The EMCAL[21] can also be used to identify electrons with p > 2 GeV/c when combining its energy deposit measurement and the momentum information from the other central barrel detectors.

The *VZERO* detector is used in pp collisions to provide a minimum bias trigger and to reject background from beam-gas collisions [90]. In Pb–Pb collisions the V0 detector is used together with the *Zero Degree Calorimeters* (ZDC) to determine the event centrality.

Measurement of muons is done in the forward direction with the ALICE muon spectrometer. The following physics topics can be addressed [93]:

- Quarkonia (J/ψ, Υ) decays into dimuons

- Single-muons from heavy-flavour hadron decays

- Low-mass vector meson decays (ρ, ω, ϕ) into dimuons

For these topics the ALICE muon spectrometer has a unique coverage in p_t and η in Pb–Pb collisions with respect to the other LHC experiments[22]. The muon spectrometer consists of a front absorber with a length of 4.13 m placed at a distance of 90 cm from the interaction point. Electrons and a major fraction of the hadrons are stopped in the absorber. Background surviving the absorber consists of the fraction of primary hadrons which are not stopped, muons from weak decays of kaons and pions, and secondary hadrons created in interactions of primary hadrons with the absorber material. Four tracking chambers are placed behind the absorber. In order to measure the momentum of the tracks, a dipole magnet providing a magnetic field of 0.7 T is employed. Behind the tracking chambers a second layer of absorber material and 2 trigger chambers with a tunable p_t cut are placed. The trigger threshold, applied to each track, is determined using Monte-Carlo simulations and is set to 500 MeV/c for the measurement of J/ψ [97] and low mass dimuons and to 2 GeV/c for the measurement of Υ and single muons from

---

[21] The same applies in principle also to PHOS, where the energy resolution is even better than in the EMCAL. Due to the small rapidity and ϕ-coverage of PHOS however it is more advantageous to use EMCAL.
[22] For pp collisions LHCb covers the same pseudorapidity range for muon measurements

heavy-flavour[23] [93]. With these trigger p_t thresholds the amount of muons from decays of kaons and pions produced in the absorber, as well as the amount of hadrons which pass the absorber, is reduced (remaining contamination: 10% at 2 GeV/c, decreasing with p_t [98]).

Further detectors in ALICE which are not used in this analysis are:

- *High-Momentum Particle Identification Detector* (HMPID): Cherenkov Detector for hadron identification up to 5 GeV/c

- *Forward Multiplicity Detector* (FMD): Detector measuring the charged particle multiplicity at forward direction (-3.4 $\leq \eta \leq$ -1.7 and 1.7 $\leq \eta \leq$ 5.1)

- *Photon Multiplicity Detector* (PMD): Detector measuring the photon multiplicity at forward direction (2.3 $\leq \eta \leq$ 3.5)

- *ALICE COsmic Ray DEtector* (ACORDE): Trigger for cosmic-ray events

---

[23] The different p_t thresholds for J/ψ and Υ allow the measurement for both particles down to the lowest p_t. The threshold for the single-muon measurement sets the low-p_t cutoff for this analysis.

2 Particle identification with the ALICE Transition Radiation Detector

The TRD plays a major role in the selection of electron candidate tracks. Due to their low mass in comparison to other species, electrons above a momentum of 1 GeV/c produce transition radiation photons while passing a radiator, which are absorbed by the drift gas at the entrance of the drift chamber. The energy from absorption is deposited in addition to the energy from ionisation.

In this chapter, the electron selection with the TRD is presented. After an overview of the detector, the stability of the detector during the data taking in 2010 is discussed. In the end of this chapter, the strategy for electron identification is shown, and the performance in data, obtained with reference samples of electrons and pions, is presented.

2.1 Overview of the ALICE Transition Radiation Detector

The TRD [99], surrounding the beampipe at a radius of 3 m, covers the pseudorapidity range $|\eta| <$ 0.9 and will have an azimuthal acceptance of 360º. The detector is be segmented into 18 supermodules in azimuth, which are further segmented into five stacks per supermodule in beam direction and six layers per stack in radial direction. In total, 540 chambers will be installed. Figure 2.1a shows the segmentation of the detector [91]. Supermodules have a height of 70 cm and a length in beam direction between 6.4 and 7 m, symmetrically around the collision point. In azimuth, supermodules have a width between 90 cm at the innermost layer and 118 cm at the outermost layer. The dimensions are indicated in Figure 2.1b. A chamber itself consists of a radiator with a height of 4.8 cm and a drift chamber with a height of 3.7 cm (see Figure 2.1c). Since transition radiation is produced at the surface of two media with different diffractive indexes, radiators should provide a large amount of surfaces a particle passes. This can be achieved using radiators made of foam or fibres, or as a stack of foils. On the other hand, a large amount of material increases material budget, which affects the momentum reconstruction and increases the conversion probability, which would especially effect the electromagnetic calorimeters, which detect photons. For all six layers together the contribution of the radiator to the material budget should not be more than 15% of a radiation length. The radiator used in the ALICE TRD is a combination of foam and fibres. The outer part of the radiator consist of plates made out of Rohacell foam with the thickness of 8 mm. The inner part of the radiator is filled with polypropylene fibres [99, 100]. Each drift chamber is divided into an amplification region with the height of 0.7 cm and a drift region with the height of 3 cm,
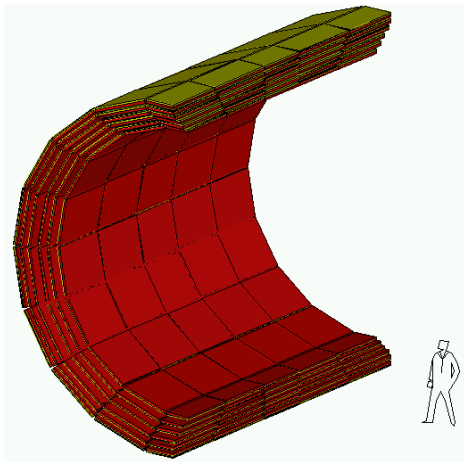
(a) Segmentation of the TRD
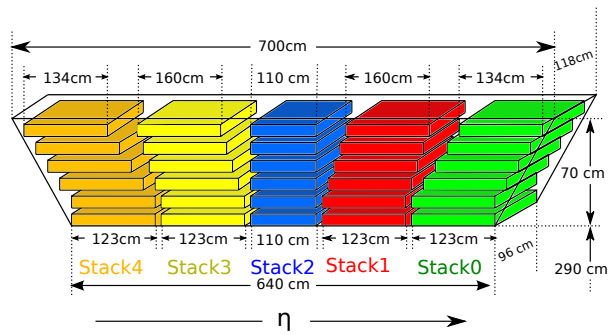
(b) Sketch of a TRD supermodule
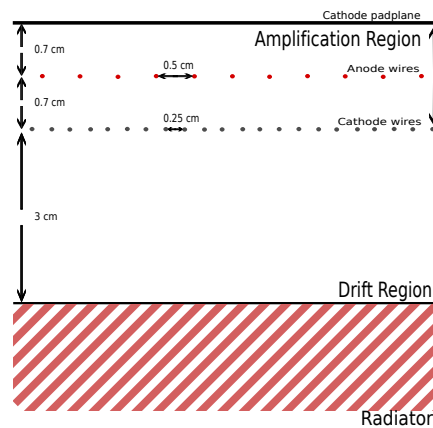
(c) Sketch of a TRD chamber

Figure 2.1: Segmentation of the TRD (a) [91]: the detector is divided into 18 supermodules. Each supermodule consists of 5 stacks in beam direction, which are further divided into 6 layers in radial direction (indicated in (b)). A sketch of a chamber is shown in (c): each chamber consists of a radiator with a height of 4.8 cm and a drift chamber with a height of 3.7 cm, divided into an amplification region with a height of 0.7 and a drift region with a height of 3 cm, separated by the cathode wire plane. The anode wire plane is located in the centre of the amplification region at equal distance between the cathode wire plane and the cathode pad plane.

separated by a cathode wire plane. The anode wire plane is located at equal distance to the cathode pad plane and the cathode wire plane. A pad plane is segmented into 144 pads in azimuthal direction and 16 rows for the outer four stacks, and 12 rows for the central stack. This leads to the total amount of 1.18 million pads for the full TRD. Also the pad size increases with the distance to the beam axis, starting from 6.35 mm in azimuth and 7.5 cm in beam direction in the innermost layer up to 7.85 mm and 9 cm in the outermost layer. In order to improve the position resolution in beam direction, even though the granularity is not as fine as in azimuthal direction, the pads are tilted by an angle $\alpha = 2^{\circ}$.

Particles passing the drift chamber produce electron clusters due to ionisation. In addition, for electrons with a momentum above 1 GeV/c transition radiation photons are produced in the radiator and absorbed
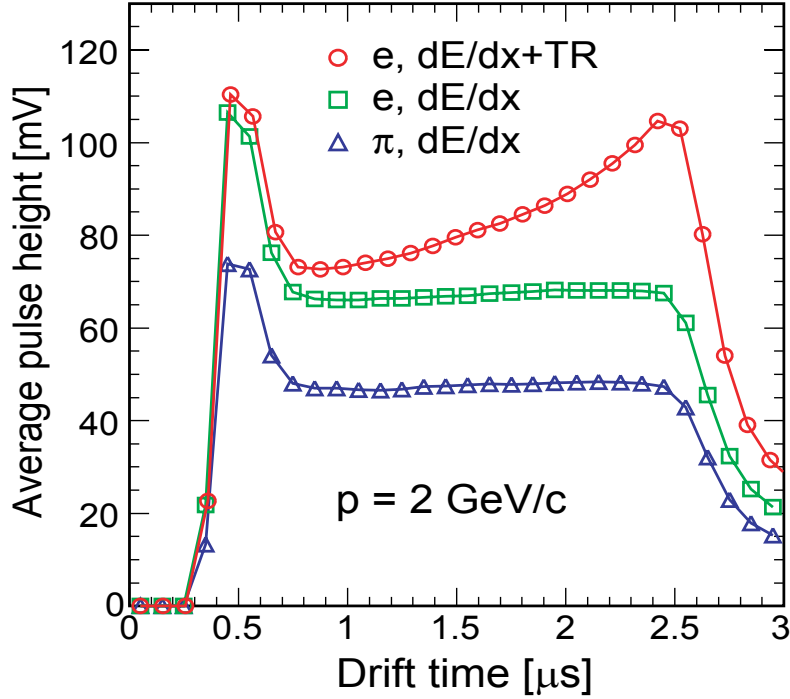
Figure 2.2: Average Pulse Height as function of time[102] for electrons passing a radiator (red), electrons passing no radiator (blue) and pions (green) at a momentum of 2 GeV/c. The peak at timebin five is produced by ionisation in the amplification region (amplification peak). For electrons passing a radiator a second peak is visible, which is produced by absorption of transition radiation photons in the drift gas at the entrance of the drift chamber (TR-peak). The measurement is done with a prototype during the testbeam in 2004.

at the entrance of the drift chamber by the drift gas producing additional electrons. As drift gas a mixture of Xe(85%), providing a good photon absorption, and CO_2 (15%) is used [101]. The electron clusters travel through the drift field (0.7 kV/m) with the drift velocity $v_{drift} = 1.5 cm/\mu s$ to the amplification region, deflected by the Lorentz angle[1] $\gamma = 8°$. In the amplification region an avalanche ionisation created by the electron clusters produces a signal in the pad plane.

The signal in the pad plane is sampled in 30 timebins of each 100 ns. Figure 2.2 shows the dependence of the average pulse height on the drift time for electrons and pions passing a radiator, and for electrons in a special setup without radiator [102]. The figure is done for particles having a momentum of 2 GeV/c. A peak is visible for all cases at timebin five, which is produced by ionisation in the amplification region (amplification peak). In the time period between 800 ns and 2.5 μs the average pulse height is approximately constant for pions and for electrons in the setup without radiator. This will be referred to as "plateau region". Comparing pions and electrons without radiator, the average pulse height for electrons is $\approx$ 1.5 times the one for pions over the full drift time. This is due to the higher energy loss due to ionisation for electrons. When including also a radiator, a second peak at late time bins (around

---

[1]   Effect coming from the crossing of the electric and magnetic field

2.5 μs) is visible. This peak is called "TR-peak" and is produced by the absorption of transition radiation photons at the entrance of the drift chamber.

The TRD can be used as trigger on single electrons, dielectrons and jets [103]. The trigger is based on track segments in single chambers. For every chamber the track segments called tracklets are created by the *Local Tracking Unit* (LTU) as a linear fit to the raw signals. Before applying the linear fit, the pad signals have to be recorded and digital filters removing tails and subtracting the pedestal have to be applied. All components are on *Multi-Chip-Modules* (MCM). Each MCM is connected to 18 pads in azimuth. The *Global Tracking Unit* (GTU) combines tracklets to tracks, which also contain a momentum estimate obtained from the distance of the track extrapolated to radius of the vertex and the nominal collision point, and information to identify particles. Single- or dielectron triggers require at least one or two tracks reconstructed as electron in the event respectively, which have a momentum above a certain threshold. The jet trigger requires a minimum number of tracks with a momentum above a threshold per stack in at least one stack. The trigger decision has to be provided within 6.1 μs to the ALICE central trigger. In case a TRD trigger is required, the TPC would only be read out if the trigger is provided. A delay of 6.1 μs is sufficient in order to not restrict the η range in the TPC. In order to keep the power consumption low, the TRD needs a trigger input in order to wake up the electronics. This input is called *Pretrigger* [104] and has to be provided 500 ns after the interaction. In case the wake up would be too late, the first time bins of the pulse height spectrum would be removed[2]. As input for the pretrigger the fast detectors V0, T0 , and TOF as well as the bunch crossing information from the LHC is used. At the MCM, raw signals are streamed in parallel to the LTU and to an event buffer. From the event buffer the raw data are further streamed to disk or to the *High-Level Trigger* (HLT), a large computing cluster [106]. At the HLT more sophisticated triggers including other detectors can be applied. In addition, the HLT is also used to calibrate the detector.

2.2 Track reconstruction in the ALICE Transition Radiation Detector

The first step towards particle identification with the TRD is the reconstruction of the trajectories of charged particles. The reconstruction can be done propagating outwards tracks found by the TPC (global tracking [93]) or based on track candidates found inside the TRD (stand alone tracking [105, 107, 108]). The global tracking is based on a Kalman Filter, which has the advantage that it can include a correction for the energy loss of a particle passing the detector material. In the stand alone tracking a helix fit, which is adapted to the detector structure, is used.

---

[2]   Examples for this can be found in [105], recorded during the cosmics data taking 2008
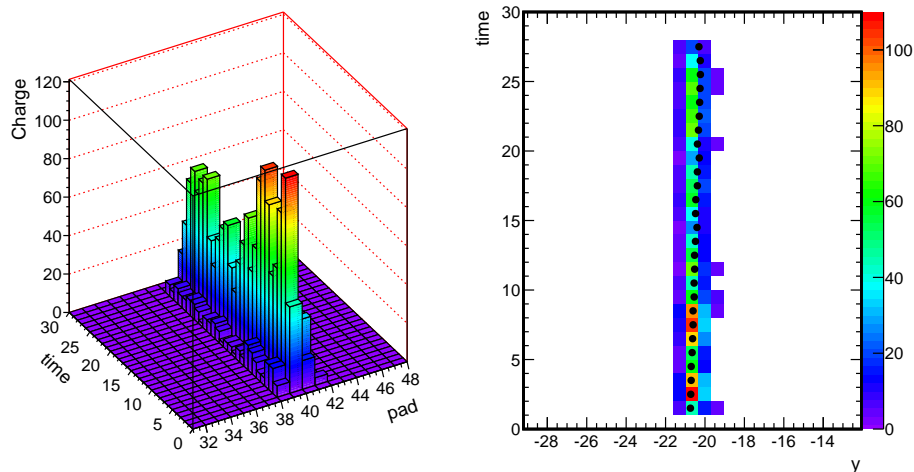
Figure 2.3: Cluster finding in the TRD. The charge deposited by a charged particle passing the drift chamber is shown on the left side. Based on the charge measurement in the different pads, clusters are created. The reconstructed position is shown on the right side.

Charged particles passing a chamber produce electron clusters due to ionisation and TR-absorption which drift in the drift field to the cathode pad plane where a charge deposit is measured in 30 time bins. The signal is spread over several pads, typically three, in a column, steered by the *pad response function* which can be considered as Gaussian. In time the signal is also not a sharp signal, but has a shape called *time response* [3], which comes from the response in the electronics and the mobility of the ions in the amplification region. The time response leads to tails in the charge distribution as function of time, which causes the signal to be distributed over several time bins. These tails have to be removed by a *tail cancellation* mechanism which deconvolutes the contribution from several time bins.

From the raw signals after tail cancellation, *clusters* are created. These clusters store position and charge deposit information for a given time bin. The position of the cluster is calculated in azimuth taking the centre-of- gravity of the three pad charges and in radial direction from the drift time multiplied by the drift velocity. To minimise the amount of clusters created due to detector noise, the charge in the central pad and the ones in the neighbouring pads as well as the sum of the three pad charges have to exceed different thresholds. Figure 2.3 gives an example of the clusters reconstructed for a charged particle passing the detector. In z- direction the pad centre is used as approximation for the cluster position. The cluster position is further corrected for the time offset and the Lorentz- angle. Clusters have a resolution of ≈ 300 μm in azimuthal direction. Summing up the pad charges of the three central pads, the total charge of the cluster is calculated. In the addition to the total charge, the charge of the central pad and the three neighbouring pads in each direction are stored in the cluster.

---

[3] The time response was measured using a ^{55}Fe source irradiating a prototype chamber

For further discussion the ALICE tracking coordinate system [107] is used. In this coordinate system the x-coordinate is along the radius, the z-coordinate the beam direction and, the y-coordinate the ϕ direction. The origin is at the nominal collision point. ϕ is split in 18 sectors adapted to the segmentation of the central barrel detectors (i.e. TRD). The origin in azimuth is in the middle of a given sector. To change to a different sector, the coordinate system needs to be rotated to the new sector. For neighbouring sectors, the x and y coordinate are rotated by the angle $\alpha = 0.35$, which is the angular coverage of a sector.

Clusters in a chamber, produced by a charged particle passing the detector, can be combined to track segments, called tracklets. Due to the small radial size of the drift chamber, tracklets can be considered as linear. In order to create the tracklets, a reference position and a reference inclination is needed. The reference position is obtained using either the extrapolation of trajectories reconstructed in the inner detectors TPC and ITS, which is done using a Kalman Filter, or track candidates found in the TRD with a stand alone tracking algorithm. Tracks candidates from the stand alone algorithm are based on space points which are the centres of gravity of the cluster positions projected to the y-z plane (parallel to the readout plane). These space points are considered as likely produced by a tracklet [108]. Based on the reference position and the inclination, clusters are attached to the tracklet. Appropriate clusters are required to be within a maximum distance to the expected position, where the maximum depends on the uncertainty of both the cluster and the track extrapolation. In certain cases, for example if the particle passes the outer part of a row or the track is very inclined in z-direction, also the neighbouring pad row can contain a part of the signal. For this, also clusters in the neighbouring pad row can be attached to the tracklet. A linear fit to the clusters is performed to obtain a reference position, which is used in the Kalman filter as further space point. At least eight associated clusters are required to accept the tracklet. After updating the Kalman filter, the track is extrapolated to the next chamber. Base on the track fit, a momentum estimation is available for each tracklet. Due to energy loss in the material the momentum can be lower than at the vertex. The track resolution is dependent on the inclination of the track in the xy-plane. The best resolution, which is 120 μm, is obtained at the $\phi = 8°$, which is the Lorentz angle.

In the stand alone tracking the difference in the inclination between tracklet and track can be used to reject fake tracks. On the other side, due to decalibration of the drift velocity, the tracklet can be inclined with respect to the track, which prevents a too strict cut. The track model fit is done in the stand alone tracking to clusters in the tracklets attached. At least four tracklets are needed for a full track fit. The tilting of the pad is used to improve the position in z-direction. For this the helix model which is used in the fit is adapted (see [105]). The adapted model contains the assumption that the tracks are originating from the nominal collision point.
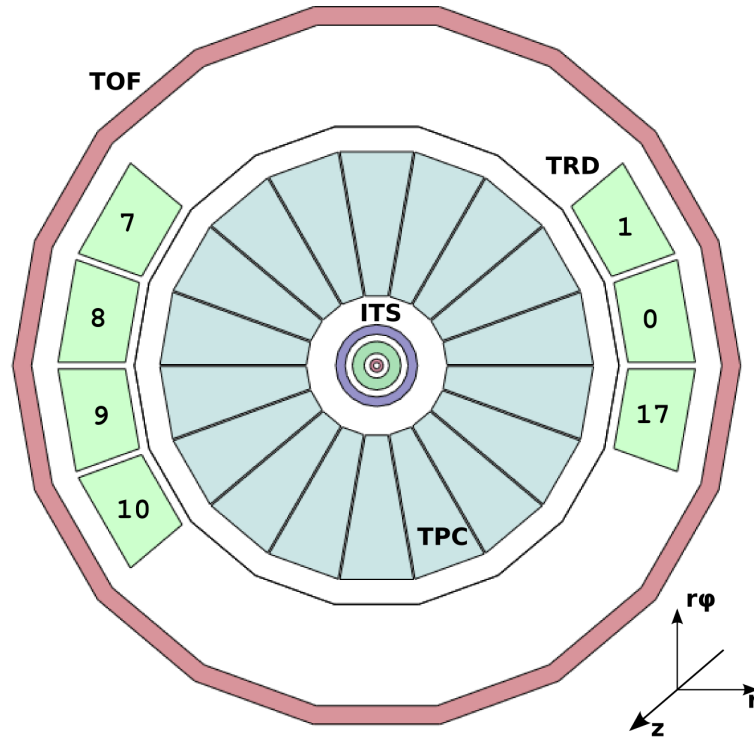
Figure 2.4: Geometry of the central barrel in 2010: seven out of 18 supermodules are installed. Numbers indicate the position of the supermodules in azimuthal direction. A coordinate system indicates the direction of the z-axis. Not shown in this setup are the detectors EMCAL and PHOS, which also were partially installed in 2010.

2.3 The ALICE Transition Radiation Detector in the proton-proton data taking in 2010

The LHC was commissioned in fall 2009. Before the first beams were injected into the collider, a period of cosmic ray data taking took place, starting in August 2009. During this period, the detectors were commissioned and tested. In addition, the data was used to calibrate and align the detector, and to test the status of the software. The TRD participated in this data taking with 7 supermodules. A special trigger setup was used to select events: a fast signal ($\approx 250 \ \mu s$) was provided by TOF requiring hits in opposite sectors of the spectrometer, which indicated a particle passing the detector. In addition, TRD provided a trigger requiring a charge measurement over threshold in at least four layers of a stack. In the first part of the data taking (August to October), a mixture of Ar and CO_2 was used as drift gas, where Xe replaced Ar at the end of October 2009. Events were collected without magnetic field. These events were used to align the detector [109], both chambers within a stack and full stacks relative to the TPC. In case the TRD was running without the other central barrel detectors, the events were only be used for internal alignment.

Table 2.1: Overview over the data taking periods. Shown is the number of minimum bias events for each period

Period	Number of events
LHC10b	28M
LHC10c	100M
LHC10d	178M
LHC10e	164M

In parallel to the cosmic ray data taking, ^{83m}Kr was injected into the TRD gas system. The metastable krypton was obtained by β-decay of ^{83}Rb and decayed itself into stable ^{83}Kr with emission of a photon. The photon has a characteristic energy spectrum with peaks at 9.4, 12.6, 19.6, 29 and 41.6 keV. Due to absorption of the photon in the drift gas, the energy is deposited in the chamber and can be read out. For the read out a random trigger is used. The measurement of the decay spectrum of ^{83m}Kr compared to the known peak positions was used to obtain pad-gain calibration [110].

On November 23rd, 2009, the first collisions were provided by the LHC. In this run, only the SPD and the V0 detectors participated. The regular data taking started on December 6th, 2009. During this period, the beam energy was still the injection energy of 450 GeV provided by the SPS. In total, 492000 events were collected. First checks of the tracking and electron identification performance of the TRD were done, indicating that the detector is in operation and behaves stable [111]. The statistics accumulated does not allow the usage for physics analysis.

In 2010, the proton-proton data taking started in March and lasted until October 2010. It was divided into several data taking periods. The centre- of-mass energy was 7 TeV, with a short interruption having beams at the injection energy. Table 2.1 shows the number of minimum bias events collected in each of the data taking periods. Each data taking period itself consists of several runs. As in 2009, seven out of 18 supermodules were installed. The installed supermodules were situated in the sectors 0, 1, 7, 8, 9, 10 and 17. Altogether the geometrical acceptance in ϕ was 0.38, covering $340^{o} < \phi < 40^{o}$ and $140^{o} < \phi < 220^{o}$. Figure 2.4 indicates the setup available in 2010. Due to problems with the drift voltage several chambers had to be excluded from the analysis. These chambers are listed in Table 2.2. The problems happened at different times, partially even during a run. To guarantee a constant acceptance over a full period, the chambers are excluded from the analysis for all runs available in a periods. For this, the number of tracks above $p_t = 2$ GeV/c having a tracklet in a given layer was compared to the number of selected TPC tracks as function of η and ϕ. With the help of η and ϕ, stacks and sectors can be identified. In case the chamber was operational over the whole period, this ratio should be close to

Table 2.2: Chambers with high-voltage problems in different sectors (18 out of 210). Out of the 35 stacks installed in 2010, four stacks have four good chambers, 14 stacks have five good chambers, and 17 stacks have six good chambers.

sector	chamber number
0	5, 15, 16, 27
1	32, 50
7	212, 227, 228, 231
8	265
9	287
10	318
17	520, 524, 532, 533, 539

the tracking efficiency in the TRD in the centre of the chamber. A significant deviation indicates problems with the chamber, and the chamber has to be excluded from the analysis. In order to exclude tracklets in problematic chambers from the analysis, the chamber number has to be calculated for each tracklet. For this, tracks are extrapolated to the TRD layers, and the azimuthal angle is recalculated. Based on cuts on η and ϕ, the chamber number is identified. In case the chamber is in the list of those to be excluded, the charge information is set to 0 and the number of tracklets is lowered by one. The procedure to calculate the chamber number is checked with tracks which contain additional reconstruction information, among them the chamber number. It turns out that the method works reliably for p_t above 700 MeV/c with an efficiency of close to 100%. Below 700 MeV, the efficiency drops. In the low-p_t region, where tracks are stronger curved, the extrapolation is less precise due to energy loss correction. Consequently, this procedure is applied only for tracks with p_t above 700 MeV/c. The same procedure is applied to the dedicated Monte-Carlo samples used for efficiency correction. Due to this, when requiring a certain minimum number of tracklets for a track, the acceptance is further reduced.

Before data analysis, the Transition Radiation Detector has to be calibrated and aligned to the TPC [109]. As discussed above, one source for the alignment procedure was the cosmic ray data taking in 2009. In addition, in spring 2010, for a short period the magnetic field was switched off. This provided a high statistics sample of straight tracks from collisions which are preferentially used in the alignment procedure. In addition, each chamber has to be calibrated for variations in the drift velocity, the starting time of the signal and the chamber gain factor. These quantities are calibrated run-by-run using tracks [111, 112]. This means, that in order to obtain the calibration constants, events have to be reconstructed first, either with default calibration constants, or with those from the previous run. In a second reconstruction, the calibration parameters can be applied. The start time of the signal can be directly obtained

from the time bin of the amplification peak. Several methods are available for the calibration of the drift velocity: either the pulse height spectrum can be used measuring the time duration of the plateau structure after the amplification peak, or the drift velocity can be obtained from the difference between track and tracklet angle. As third option, also a *GOOFIE*[4] provides a drift velocity measurement, which is already available during the run, however useful only for monitoring purposes. Chamber gain factors are derived from the charge deposit distribution assuming the dominating contribution is from pions. This assumption is especially problematic in case the events triggered either by the TRD or by the EMCAL enhancing electrons in the sample, which implies the necessity of minimum bias events for calibration purpose. Alternatively the chamber gain factor can be obtained from the pulse height spectrum, which is however connected to the drift velocity.

During the data taking in 2010, the trigger capabilities of TRD as discussed in section 2.1 were not applied. The commissioning of the trigger was performed in 2011 [103] and will be applied during the data taking periods in 2012, where also more supermodules are available (10 in 2011, 13 in 2012). The analysis discussed here was performed using minimum bias events.

2.4 Performance of the Transition Radiation Detector in proton-proton collisions

To assure a good data quality the behaviour of the TRD during the data taking was monitored run-by-run. The monitoring is done in the *AliRoot* (ALIce ROOT) Software package PWG1. Several quantities are monitored run-by-run.

- Tracking efficiency for positive and negative charged particles with respect to the number of TPC tracks

- Tracklet charge for single layers

- Average pulse height versus drift time

- Number of tracklets/track

- Number of clusters/track

- Sum of the cluster charges

These variables are sensitive to the calibration of the TRD. Distributions of the trending variables are combined to four summary figures which are discussed in the following.

---

[4]   A GOOFIE (Gas prOportional cOunter For drIfting Electrons) contains an α source and a detection mechanism. From the time difference the drift velocity can be determined. For more information see[113]
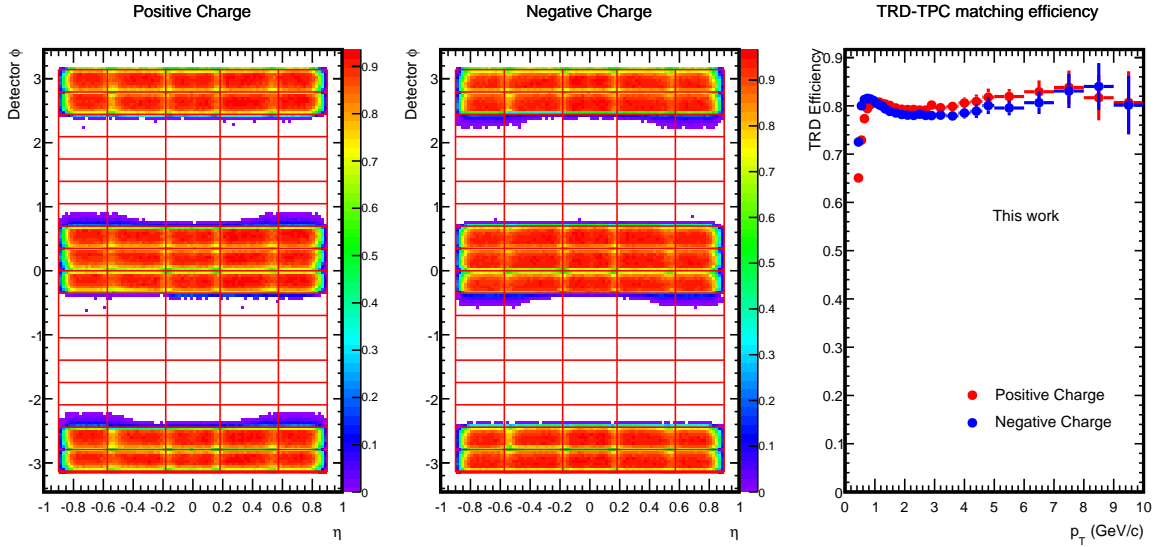
Figure 2.5: Matching efficiency between TPC and TRD for positive charged tracks and negative charged tracks for run 126088 (LHC10d) for tracks having at least 1 tracklet: Left and middle plots show the η-ϕ profile of the matching efficiency. Red lines indicate the detector segmentation, where sector 0 starts at 0 in ϕ. The white area is due to missing supermodules. The right plot shows the matching efficiency versus the transverse momentum. Deviation from 1 results from the definition of the acceptance area.

Figure 2.5 shows the TPC-TRD matching efficiency for run 126088 from period LHC10d. Reference tracks in the TPC have to fulfil the following conditions:

- Refitted in the TPC

- Have at least 100 TPC clusters

- *Distance of closest approach* (DCA) to the primary vertex

    – in xy: < 40 cm

    – in z: < 15 cm

In the left and middle plot the dependence of the matching efficiency on η and ϕ is shown integrated over all transverse momenta above 0.3 GeV/c for tracks having at least one TRD tracklet. Red lines indicate the segmentation of the TRD. The white area is due to supermodules which were not installed yet. The matching efficiency is highest with $\approx$ 0.9 in the centre of a chamber and drops towards the chamber borders. On the right side the matching efficiency is shown as function of the transverse momentum for tracks in the acceptance. The acceptance is defined as the area in η and ϕ, where above a p_t of 1 GeV/c counts in the TRD are registered. The granularity of the binning[5] chosen resulted in an overlap of active

---

[5] Due to technical reasons a finer binning could not be chosen

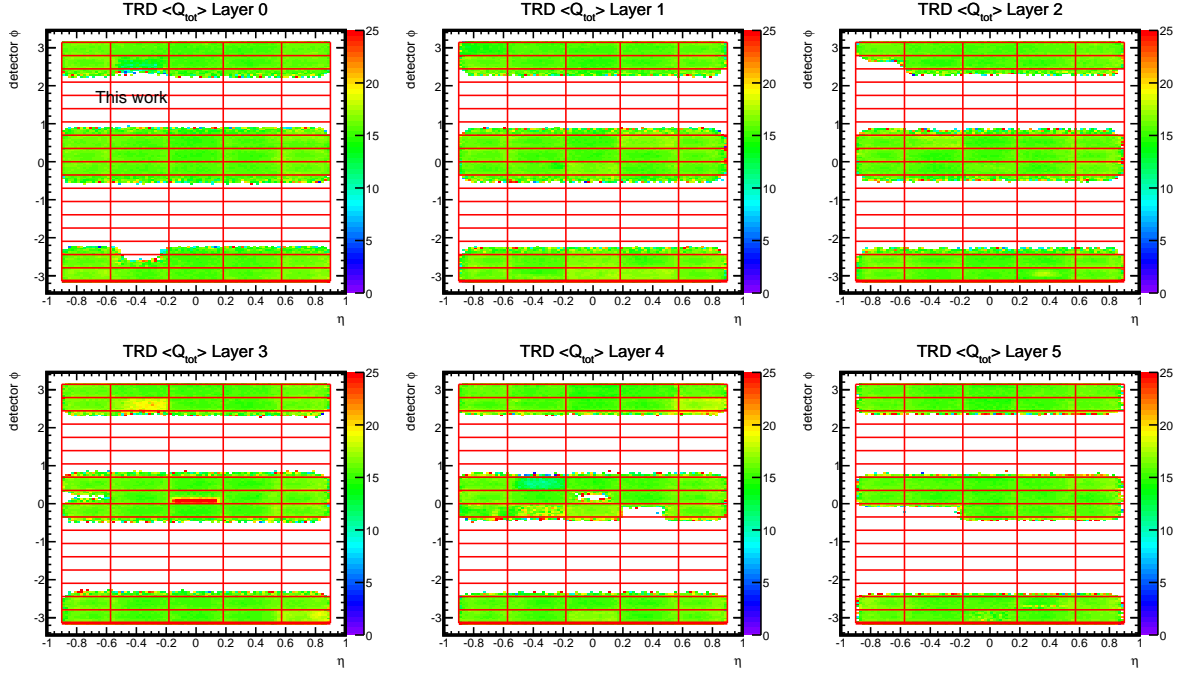**Figure 2.6:** Charge deposit as function of η and ϕ for the 6 TRD layers for run 126088. Red lines indicate sector borders. White areas are due to inactive area (missing supermodules) or masked half chambers.

area with dead area (chamber borders, not installed sectors). This leads to a slightly lower efficiency (0.8) shown in here with respect to the chamber centres.

Figure 2.6 shows the charge deposit as function of η and ϕ for run 126088. This quantity is sensitive to chamber and pad gain. After calibration a uniform distribution is expected. Chambers with too low or too high gain would be visible as outliers in the charge distribution. Decalibration in the pad gain would be visible as a non-uniform structure within a chamber. Apart from one halfchamber (layer 3, sector 0, stack 2) and one full chamber (layer 3, sector 7, stack 3) with a too high gain one can see that the charge deposit is uniform over the detector within 15%.

Figure 2.7 shows the average pulse height as function of the drift time. On the left side it is shown as a function of time bin. The amplification peak has its maximum in the third time bin, with an average pulse high approximately twice the average pulse height of the plateau region (timebins 10 to 15). The different time bin of the amplification peak compared to Figure 2.2 results from adjustments in the pretrigger timing which were done before the data taking. On the right side the pulse height distribution is shown versus time. The pulse height distribution for a single timebin has the shape of a Landau distribution, as shown in Figure 2.8. This is reflected by the white markers which indicate the most probable value of a Landau fit to the pulse height distribution within one time bin.
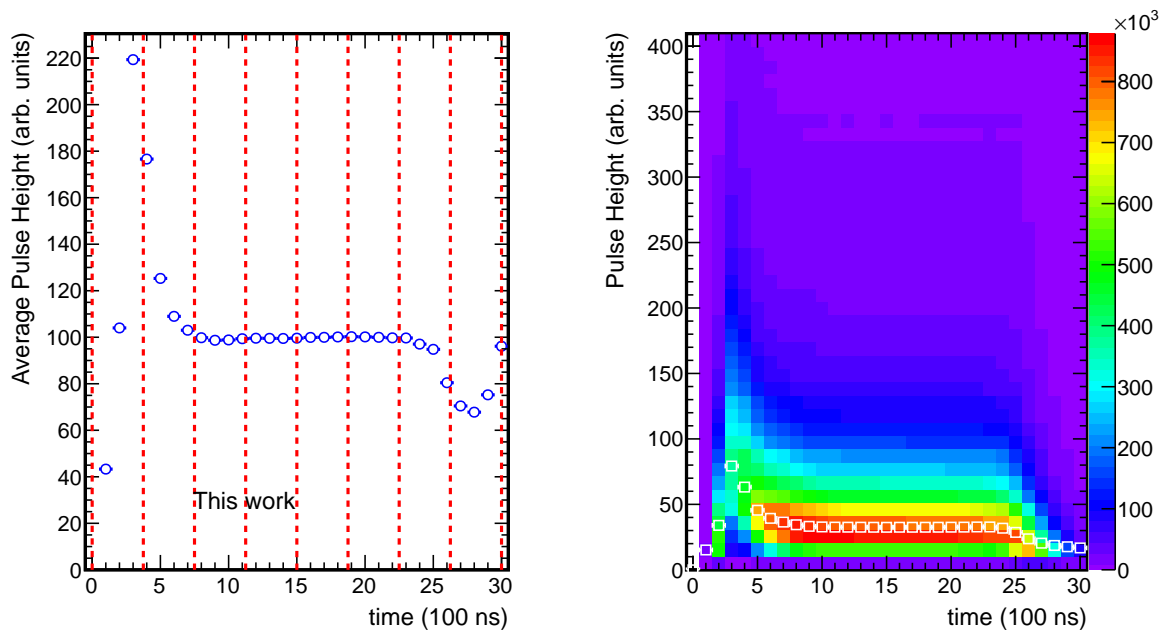
Figure 2.7: Average pulse height (left) as function of the drift time for run 126088. Red lines indicate time slices. On the right side the pulse height distribution is shown versus the drift time. The white markers indicate the most probable value derived from a fit of a Landau function to the pulse height distribution of a single timebin.

Figure 2.9 gives an overview over further track quality variables. In the top left plot the distribution of the number of tracklets integrated over all momenta is shown. Tracks with few tracklets are tracks leaving a sector towards a dead area. These are mostly low-momentum tracks which are curved. For high-momentum particles which are straight at the TRD level, tracks are expected to have a high number of tracklets. This can be seen in the top middle figure where the momentum dependence of the number of tracklets is shown. In the low-momentum region, tracks in average have few tracklets. At 500 MeV/c tracks are expected to have 5 or 6 tracklets. For tracks passing chambers which are not operational or excluded, the number of tracklets is lower by the amount of excluded layers passed by the particle. The distribution of the number of clusters per tracklet is shown in the top right plot. As can be seen from the pulse height spectrum, the length of the signal is 24 timebins. For this the peak of the distribution is expected at 24 clusters. Thresholds during the cluster finding can lead to the fact that for certain tracks fewer clusters are reconstructed. This is the reason for the tail towards lower number of clusters per tracklet. The tail towards high number of clusters per tracklets is produced by tracks crossing pad rows where clusters are reconstructed for more than one pad row. In the bottom left plot the distribution of the number of clusters per track is show. This distribution is a convolution of the distribution of the number of clusters per tracklet and the number of tracklets per track. The distribution of the cluster charge and
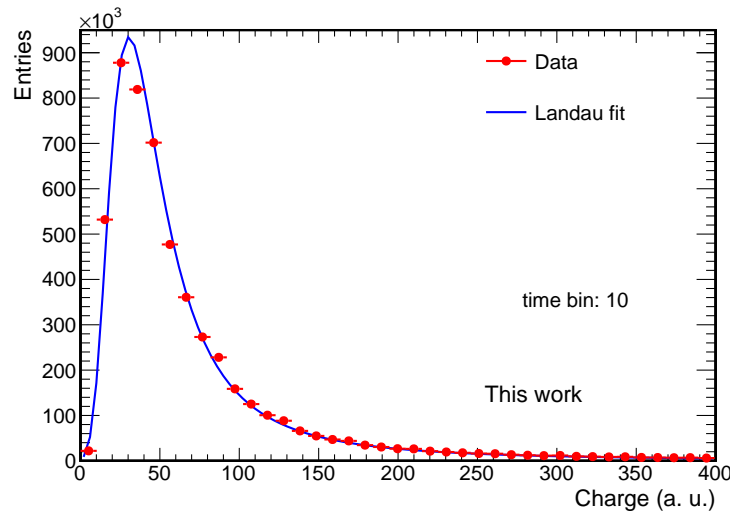
Figure 2.8: Charge deposit distribution in a time bin. The charge deposit follows a Landau distribution. This is indicated by a fit of a Landau function, shown in blue.

the sum of the cluster charges are shown in the bottom middle and right plots. Both distributions have the shape of a Landau function.

From the distributions discussed above, trending variables are derived, which are monitored versus the run number. These trending variables are:

- Timebin of the amplification peak

- Plateau value of the average pulse height derived from a linear fit to the timebins 10 to 15

- Mean number of clusters per tracklet

- Mean number of tracklets per track

- Average sum of the cluster charges

Figure 2.10 gives an overview of the trending variables for period LHC10d. The plateau height (a) is stable around 100, variations are within 10%. The timebin of the amplification peak, defined as timebin where the average pulse height has its maximum, is stable at 3. Also the mean number of clusters and mean number of tracklets are stable at 24 and at 4, respectively. For the mean of the sum of the cluster charges fluctuations can be seen towards the end of the period. These fluctuations are within 10% of the mean value of the sum of the cluster charges.
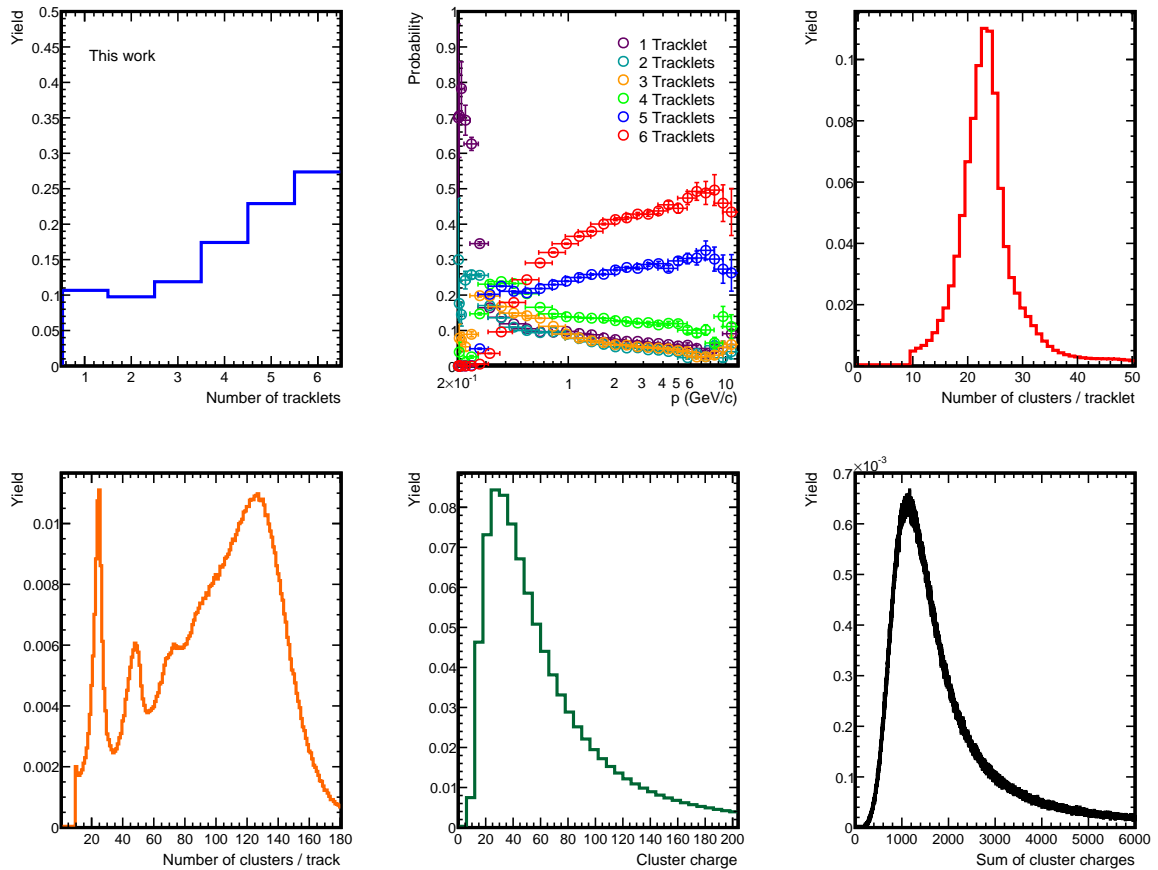
Figure 2.9: Track quality monitoring for run 126088: Shown are the distributions of the number of tracklets (top left), the p_t dependence of the number of tracklets (top middle), the distributions of the number of clusters per tracklet (top right) and per track (bottom left), the distributions of the cluster charge (bottom middle) and the sum of the cluster charges (bottom right).

2.5 Particle identification strategy

Particles are identified using a Bayesian approach: for every tracklet the probability to be of a given particle species is calculated, where the species are electrons, muons, pions, kaons, and protons. Several methods to obtain the probability for a single tracklet can be applied:

- 1D Likelihood method [93]

- 2D Likelihood method [93]

- Neural Network method [114, 115]

Here the 1D Likelihood method, which is discussed in detail in the following sections, is applied to data from pp collisions. The performance is slightly inferior to that of the other two methods. However it is more robust, since it does not depend on the quality of the drift velocity and the time offset calibration.
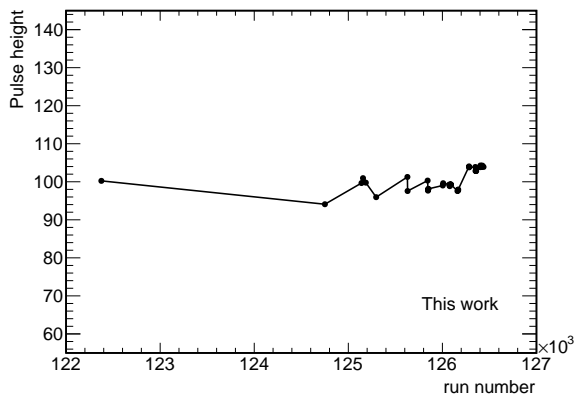
(a)
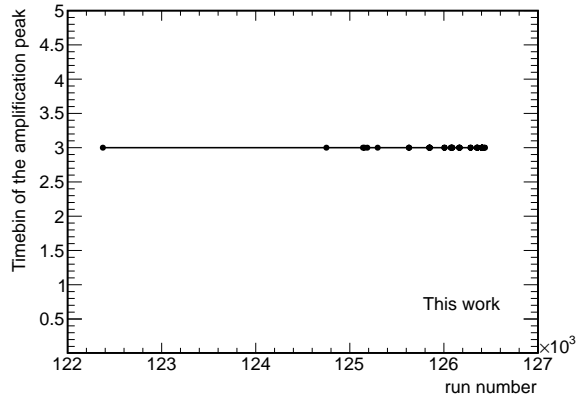
(b)
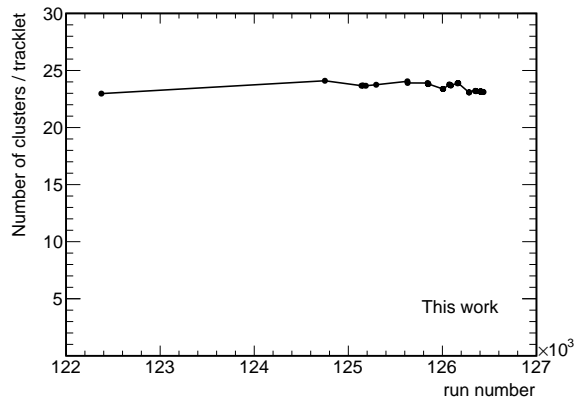
(c)
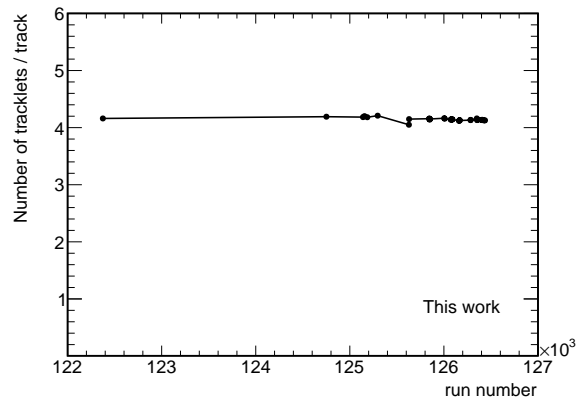
(d)
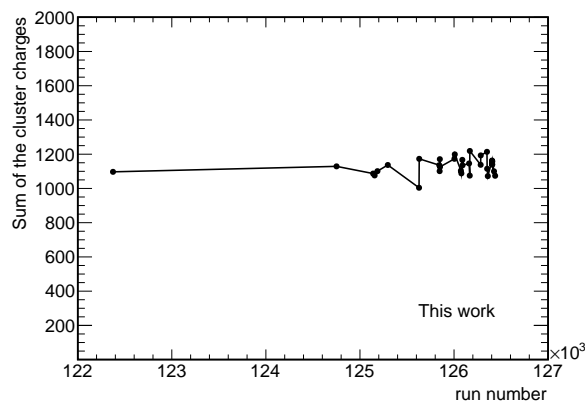
(e)

Figure 2.10: Overview of the trending variables in the TRD versus the run number for period LHC10d. Shown are the plateau height (a), the timebin of the amplification value (b), the mean number of clusters per tracklet (c), the mean number of tracklets per track (d), and the mean sum of the cluster charges (e).

Based on the probabilities obtained in each tracklet individually with one of the methods listed above, the probability for a track to be of a certain particle species is calculated via the Bayesian formula

$$P(i) = \frac{\prod_{j=1}^{6} P_j(i)}{\sum_{k \in e, \mu, \pi, k, p} \prod_{j=1}^{6} P_j(k)}, \qquad i \in e, \mu, \pi, k, p \tag{2.1}$$

where $P_j(i)$ is the probability obtained in layer j to be of species i. The method is assuming independent measurements $P_j(i)$ in the different chambers. However energy loss leads to a reduction of the momentum. This is especially important for electrons which have a higher energy loss. Due to this, $P_j(i)$ is obtained for the momentum reconstructed in chamber j.

2.5.1 Charge deposit in a tracklet

Charge deposit in the TRD is measured as a function of the drift time as discussed in section 2.1. The charge is divided into 8 slices, as indicated in Figure 2.7, according to the drift length:

$$Q_{slice} = \frac{\sum_i q_i}{dx * \sqrt{1 + \frac{dy}{dx}^2 + \frac{dz}{dx}^2}} \tag{2.2}$$

where q_i are the clusters within the drift length segment of the slice. The normalisation takes into account differences in the tracklet length due to the tracklet inclination: this leads to higher charge deposit for tracks with stronger inclination. These slices serve as input for the neural network method. The total charge used for the 1D-Likelihood method is calculated as the sum of slices.

Reference charge deposit distributions are derived using a clean sample of electrons from γ conversions, pions from K_S^0- and protons from Λ-decays. The criteria to obtain these samples are listed in Table 2.3 [116]. Additionally a cut on the Armenteros variables is applied (see Appendix D). For γ-conversion candidates, a cut on the angle Ψ_{pair} is applied. Ψ_{pair} is defined as:

$$\Psi_{pair} = \sin^{-1} \frac{\Delta \Theta}{\xi} \tag{2.3}$$

Table 2.3: Overview of the selection criteria used to obtain the reference samples of electrons, pions and protons[116]. Listed are the topological cuts used to identify the mother species. The χ^2/NDF is taken from a Kalman fit of the secondary vertex by the two daughter tracks constraining the mother track to originate from the primary vertex.

	γ	K_S^0	Λ
cos of the pointing angle	[0,0.03]	[0,0.03]	[0,0.03]
Ψ_{pair}	[0,0.05]	–	–
DCA between daughter tracks (cm)	[0,0.25]	[0,0.02]	[0,0.02]
Radius of the secondary vertex (cm)	[3,80]	[2,30]	[2,30]
Max. χ^2/NDF from the Kalman fit	7	5	5
Invariant mass (GeV/c^2)	<0.05	[0.486,0.508]	[1.11,1.12]

where Θ is the difference of the polar angles between the daughter tracks, and ξ is the angle between the momentum vectors of the daughter tracks. This cut was introduced by PHENIX [117] and makes use of the fact that the magnetic field only affects the opening angle in the plane perpendicular to the magnetic field, not the polar angle component. So for γ-conversions, where the daughters are emitted under a small opening angle, Ψ_{pair} should be close to 0, while for other decays (i. e. Dalitz decays) a flat distribution is expected. In order to further clean up the electron sample, a cut on the TPC dE/dx, expressed as difference to the expected dE/dx for electrons at the given momentum normalised to the dE/dx-resolution is applied. Electron candidate tracks are required to have a dE/dx within [-1.43, 2.57]σ. The asymmetric range accounts for a shift in the mean dE/dx from 0 which was observed for electrons from γ conversions. The shift results from daughter tracks which are not separated enough at the entrance of the TPC. In this case, the charge distribution produced by the two tracks, which is read out, overlaps, and shared clusters containing contributions from both tracks are produced. Since the dE/dx calculation in the TPC is based on the truncated mean, the resulting dE/dx is biased by the shared clusters. This happens for γ conversions in the outer ITS layers or the entrance of the TPC. The shift is not observed for tracks requiring a hit in the SPD.

Figure 2.11 shows the charge deposit of electrons from conversions and from pions from K_S^0-decays as explained above. The distributions are obtained for tracks with a momentum of 2 GeV/c at the TRD. A good agreement to testbeam measurements from 2004 can be seen.

The stability of the charge deposit in the TRD as function of time is checked using the most probable value and the width of the energy loss distribution for pions having a momentum of 2 GeV/c. The amount of pions is high enough that the charge deposit can be studied run-by-run, which especially for short runs having only up to 10000 events is not possible for electrons due to limited statistics. Figure 2.12 shows
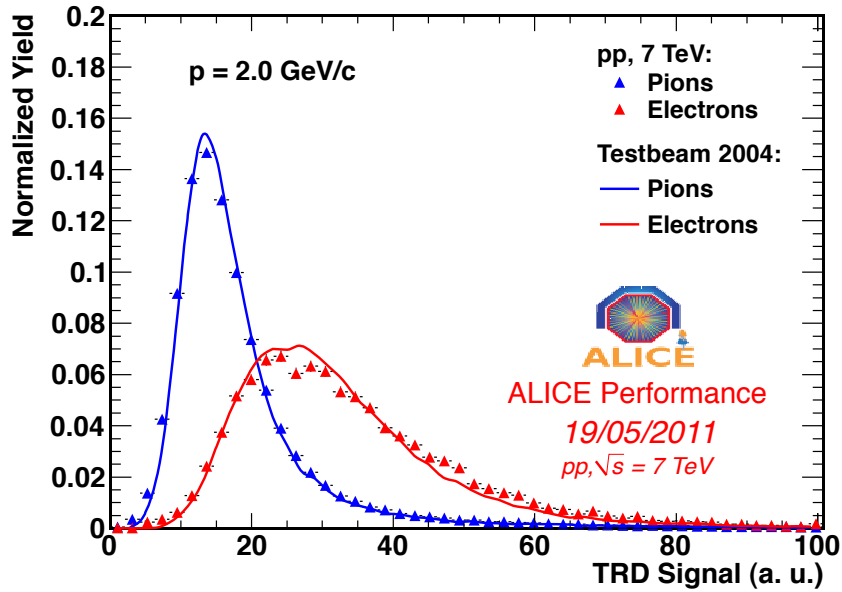
Figure 2.11: Charge deposit for electrons (red) and pions (blue) at a momentum of 2 GeV/c (taken from [118]). Lines indicate the charge distributions measured in the testbeam 2004.

the time dependence of the most probable value and the width of the charge deposit distribution. For comparison also the mean and the RMS are shown. Run numbers below 127000 are from period LHC10d while runs with higher run numbers are from period LHC10e. As can be seen from the figure, both most probable value and width are stable in time for LHC10d. Variations are below 10%. In period LHC10e a slight increase in the most probable value with the run number is visible while the width is stable in time.

2.5.2 Reference distributions from the testbeam in 2004

In 2004 tests with a prototype stack of the ALICE TRD were performed using a testbeam provided by the *CERN*[6] *Proton Synchrotron* (PS)[7] [119]. A beam consisting of electrons and pions was directed to the stack for momenta from 1 to 10 GeV/c in integer momentum steps, with an additional step at 1.5 GeV/c. Electrons and pions were identified using a combination of a Cherenkov detector and a lead glass calorimeter. Only events containing one track were considered. For both species the charge deposit distribution in a TRD chamber was obtained at each given momentum value.

Figure 2.13 shows the comparison of the charge deposit distribution for electrons and pions between pp collisions and the testbeam. In pp collisions electrons are taken from γ conversions and pions are taken from K_S^0-decays. The charge deposit distributions from pp collisions were rescaled by a common

---

6   European Organisation for Nuclear Research
7   at CERN, Geneva, Switzerland
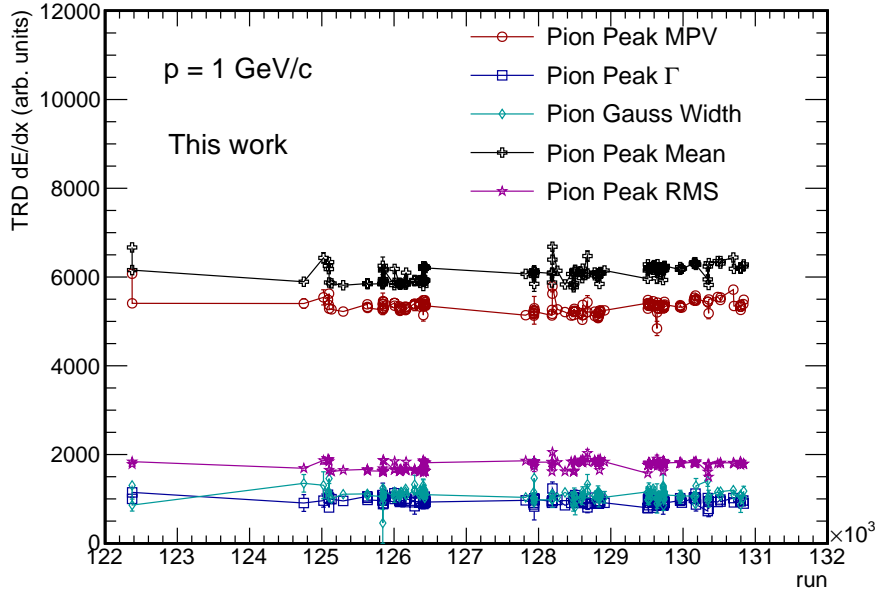
Figure 2.12: Time stability of the charge deposit in the TRD, studied using the most probable value and the width of the charge deposit distribution of pions having a momentum of 2 GeV/c. For comparison also the mean and the RMS are shown.

scaling factor which is obtained by comparing the maximum of the charge deposit distribution in data and testbeam for pions at a momentum of 1 GeV/c. This is done in order to account for differences in the absolute normalisation between the two samples.

The charge deposit distributions obtained in the testbeam are fitted with a convolution of a Landau function times an exponential, and a Gauss function:

$$f(x) = A \int_0^\infty L(x - \xi, MPV, \Gamma) * e^{-\lambda * (x - \xi)} g(x, \xi, \sigma) d\xi \qquad (2.4)$$

with the normalisation constant A, the slope parameter λ, the *most probable value* MPV. L represents the Landau function, G the Gauss function. Results of the fit are shown in Appendix C in Figure C.1. A good agreement can be seen.

Reference distributions for protons and kaons are derived via a scaling method. For this the charge deposit as function of γ is used. Figure 2.14 shows the most probable value of the charge deposit distribution as function of γ. The values are expressed relative to the most probable charge deposit for *minimum ionising particles* (MIP) , obtained here from pions at a momentum of 500 MeV/c. The black line shows the energy loss spectrum from *GEANT3* with a modified Fermi plateau derived in [101]. Since
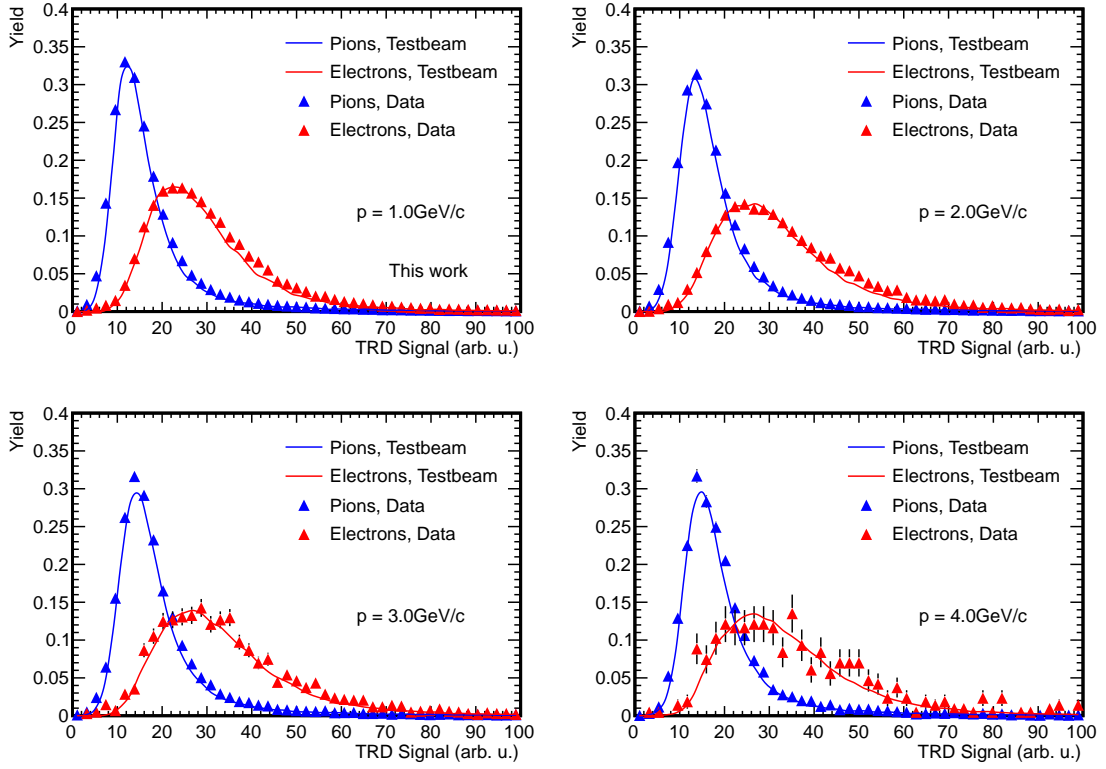
Figure 2.13: Comparison of the charge distribution between testbeam 2004 and pp data for electrons (red) and pions (blue) for the momentum steps from 1 to 4 GeV/c. Lines show the distributions from testbeam. In pp collisions electrons are taken from γ conversions and pions from K_S^0-decays. The distributions are normalised to the integral. A global scale factor is applied to account for differences in the overall normalisation of the charge deposit.

this spectrum contains only energy loss from ionisation, it saturates at the Fermi plateau and the contribution from transition radiation is not visible. This spectrum is compared to the most probable value of the charge deposit distributions for electrons from γ conversions, pions from K_S^0 decays and protons from Λ decays at different momentum values. Due to the different masses of the species, the distributions cover different γ-ranges. For electrons additionally to the energy loss, the energy deposit due to absorption of transition radiation photons can be seen. The most probable energy loss values for hadrons are in agreement with the energy loss parameterisation from GEANT3. For the scaling, the charge deposit distribution for pions at 1 GeV/c was used. The MPV and γ are scaled with

$$scale(\Gamma) = \frac{dE/dx(\Gamma)}{dE/dx(\Gamma_{ref})} \tag{2.5}$$

Using the parameterisations derived by this method, reference histograms for the 5 different species and 11 momentum values are created.

Figure 2.14: Energy loss in the TRD as function of γ for electrons (red) from γ conversions, pions (blue) from K_S^0 decays and protons (black) from Λ decays. The black line shows the energy loss spectr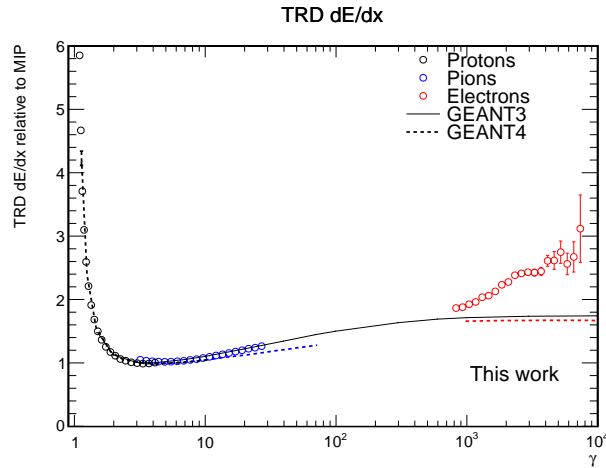um from GEANT3 [120] with a modified Fermi plateau [121], and dashed lines indicate the energy loss spectrum from *GEANT4* [122]. In addition to ionisational energy loss, energy deposit due to the absorption of transition radiation photons in the drift gas is included in the total energy deposit for electrons, which is shown in the difference of the electron most probable value to the energy loss parameterisation.

2.5.3 Verification of the particle identification performance

The performance of the particle identification is checked using reference samples of electrons from γ-conversions and pions from K_S^0-decays as discussed in Section 2.5.1. For tracks passing the TRD, likelihood values are calculated via the Bayesian formula using the references from the testbeam 2004 and renormalised to the sum of the likelihood values for electrons and pions. Only tracks with at least four tracklets are considered in this analysis. The likelihood values of those tracks are monitored as function of the momentum, separately for tracks with four, five and six tracklets. In order to select electron candidates, a minimum cut (*threshold*) on the electron likelihood is applied. Thresholds are determined in a way that the efficiency of the electron selection stays constant for all momenta. The determination is done using the electron likelihood distribution of the reference electrons. Efficiency values which are foreseen are 70%, 75%, 80%, 85%, 90% and 95%. Since the electron selection performance strongly depends on the number of tracklets, thresholds are calculated for each case separately. For example, a if threshold calculated for tracks with four tracklets is applied to tracks with six tracklets, the efficiency would be significantly underestimated. Also a threshold calculated for a minimum number of tracklets can lead to an under or overestimated efficiency in case the relative abundance of tracks with four, five and six tracklets is different in different samples. So for every number of tracklets, separate thresholds are provided. In order to evaluate the rejection performance, the thresholds obtained from the electron
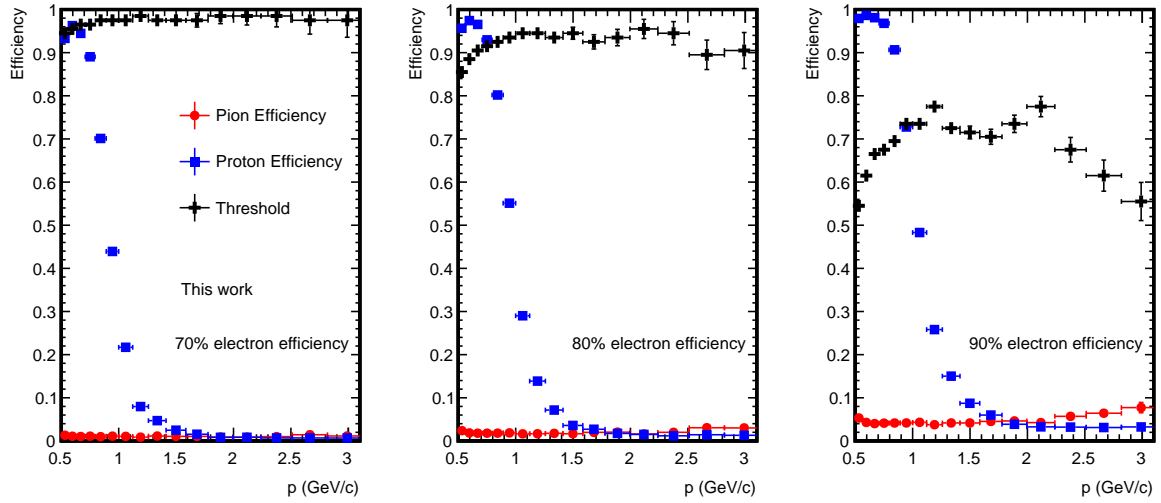
Figure 2.15: Performance of the TRD determined using reference samples from γ conversions and decays of neutral particles for the electron efficiency steps 70%, 80% and 90% for tracks having 6 tracklets: Pion (blue) and proton (red) efficiency are derived using the given thresholds (black)

reference sample are applied to the pion reference sample. The pion efficiency can be calculated as the fraction of pions having an electron likelihood value larger than the threshold value. Figure 2.15 shows the pion and proton efficiency for the electron efficiency steps 70%, 80% and 90% , for tracks having 6 tracklets. The pion efficiency is lowest at p = 1.2 GeV/c and increases towards higher momenta. This results from the fact that electrons are at the Fermi plateau and additional charge deposit due to transition radiation saturates, however the pions are at the relativistic rise and charge deposit is approaching the charge deposit for electrons. The proton efficiency is highest at momenta below 1 GeV/c. At these momenta protons are below the MIP region and therefore have a high charge deposit in the detector. Since the pion probability is almost 0 in this charge deposit region, this leads to a high electron likelihood. When approaching the MIP region, which is at a higher momentum for protons than for pions due to the higher mass, the electron likelihood becomes lower and the pion efficiency decreases. Above MIP, the behaviour is similar to the one of pions above MIP.

The threshold is parameterised as function of the momentum by fitting the following formula to values obtained:

$$f(p) = 1 - a_1 - a_2 p - a_3 e^{-a_4 p} \tag{2.6}$$

where $a_1...a_4$ are free parameters. The shape of the function has its maximum at the momentum where the separation is highest. For lower momenta the threshold rises due to the improved separation due
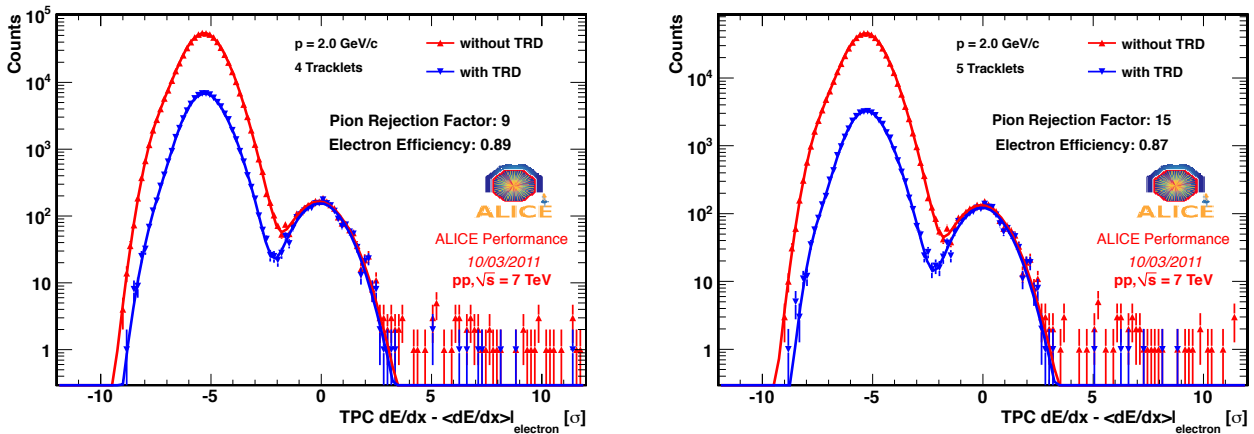
(a) 4 Tracklets

(b) 5 Tracklets
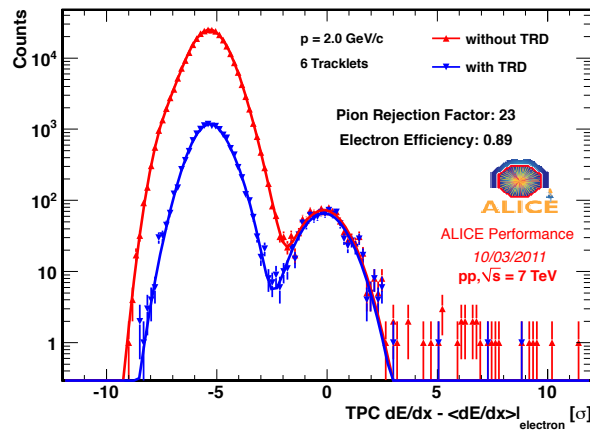
(c) 6 Tracklets

Figure 2.16: TPC dE/dx spectrum before (red) and after (blue) particle identification in the TRD for tracks having at least four (a), five (b) and six (c) tracklets at a momentum of 2 GeV/c. Pion and electron efficiency can be derived by comparing the integrals of fits of Gaussian functions for electrons and pions to the TPC dE/dx spectrum before and after particle identification in the TRD.

to the onset of transition radiation, for higher momenta the thresholds decrease since pions are at the relativistic rise.

The performance of the particle identification can also be checked by comparing the TPC dE/dx spectrum for a given momentum slice before and after selection in the TRD. This method works with all electron and pion candidates after TOF selection[8] and does not depend on reference samples. However thresholds for the electron selection have to be available. Figure 2.16 shows the TPC dE/dx spectrum for

---

8   Selection of electron candidates is used in TOF is applied before electron selection in the TRD to reject contributions of kaons and protons for momenta where the energy loss of these particles is similar to the one of electrons, and the species become indistinguishable. The rejection of kaons and protons with TOF is discussed in section 3.3

tracks having at least four (a), five (b) and six (c) tracklets at a momentum of 2 GeV/c. A sum of two Gaussian functions is fitted to the TPC dE/dx spectrum. Of these two Gaussian functions one contains the contribution from electrons and the other one contains the contribution from hadrons. Since the spectrum is taken after rejection of protons and kaons in the TOF detector, the hadrons are mainly pions. Using the fit results, the electron efficiency can be calculated as

$$\epsilon_{el} = \frac{\int_{-\infty}^{\infty} g_{el,a}(x, \mu_{el}, \sigma_{el})dx}{\int_{-\infty}^{\infty} g_{el,b}(x, \mu_{el}, \sigma_{el})dx} \tag{2.7}$$

with the Gaussian functions containing the electron contribution before $g_{el,b}$ and after $g_{el,a}$ particle identification in the TRD. Mean and width of the Gaussian function for electrons were kept as free parameters during the fits. The pion rejection factor, the inverse of the pion efficiency, is calculated via

$$\epsilon_{\pi}^{-1} = \frac{\int_{-\infty}^{\infty} g_{\pi,b}(x, \mu_{pi,b}, \sigma_{\pi,b})dx}{\int_{-\infty}^{\infty} g_{\pi,a}(x, \mu_{pi,a}, \sigma_{\pi,a})dx} \tag{2.8}$$

with the Gaussian functions containing the pion contribution before $g_{\pi,b}$ and after $g_{\pi,a}$ particle identification in the TRD. Mean and width of the pion contribution were kept as free fit parameters as for the electrons. As can be seen from Figure 2.16, the rejection power of the TRD is strongly dependent on the number of tracklets available. Figure 2.17 (left) shows the pion rejection factor as function of the minimum number of tracklets for tracks with a momentum of 2 GeV/c. As can be seen in the figure, the rejection power increases with the number of tracklets. Since every tracklet includes additional information, the separation is improved when having more tracklets. On the other side, due to dead or bad chambers which are not used in the PID, the acceptance gets reduced when requiring more tracklets (Figure 2.17 right). Therefore, a cut on the number of tracklets needs to be a compromise between high purity and good statistics. A good compromise can be the request of at least five tracklets and a stronger cut on the electron efficiency (i. e. 80%).
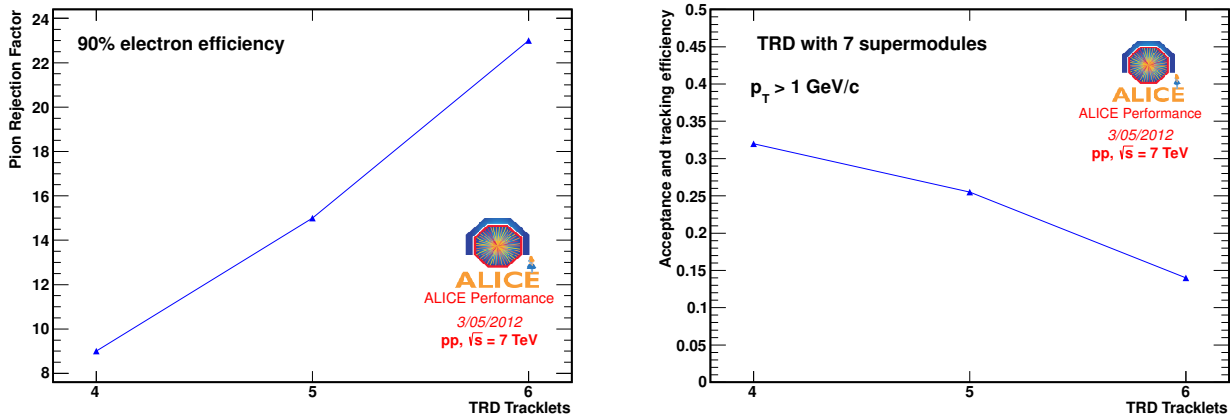
Figure 2.17: Pion rejection factor (left) and track acceptance and tracking efficiency (right) as function of the minimum number of tracklets. The pion rejection factor is derived from a fit of two Gaussian functions to the TPC dE/dx spectra with and without particle identification. The acceptance, integrated for $p_t > 1$ GeV/c having at least a minimum number of tracklets, is for the setup with seven supermodules (geometrical acceptance $\approx 38\%$).

3 Measurement of electrons from heavy-flavour decays

As discussed in section 1.2, the measurement of the p_t-spectrum of electrons from the decays of heavy-flavour hadrons is a complementary way to measure the open-charm cross section with respect to the measurement in the hadronic channels and the muon channels, and for the bottom cross section with respect to the measurement of non-prompt J/ψ. The branching ratios into electrons are known to be $\approx$ 10.3% for charm hadron decays, $\approx$ 10.8% for electrons directly produced in bottom hadron decays, and $\approx$ 9.6% for electrons from bottom hadrons decaying into charm hadrons which decay semi-electronically [123]. The measured inclusive electron spectrum contains the contributions from heavy-flavours as well as components from background sources. After subtraction of the background electrons, the remaining p_t-spectrum contains electrons from both charm and bottom. The bottom component can be quantified via several methods (selection of electron candidate tracks with a large distance to the primary vertex [124], electron-hadron correlations [64]) and subtracted so that the charm component remains.

The main steps in the analysis are:

- Selection of events and tracks

- Identification of electrons

- Subtraction of the residual hadronic background due to misidentification

- Correction for acceptance and efficiency

- Evaluation of the systematic error on the inclusive electron spectrum

- Subtraction of the electron background via the cocktail method

These steps will be discussed in the following sections.

The analysis is done for two cases, i. e. with and without the requirement of TRD electron identification. The two cases are called "TPC-TRD-TOF" when requiring the TRD, and "TPC-TOF" without TRD requirement. Both methods overlap in the p_t region between 1 and 4 GeV/c. In the analysis including the TRD, the effect of the momentum cutoff below 1 GeV/c implied by the reference distributions becomes visible. On the other hand, in the analysis without the TRD, additional rejection power is needed at higher p_t where the electron and pion dE/dx-bands overlap in the TPC. As it will be discussed in section 3.6, the

use of the TRD increases the systematic uncertainty significantly, so it is advantageous to waive the additional rejection power of the TRD in the p_t region where the separation using TOF and TPC is sufficient. The final inclusive electron spectrum is obtained combining the two analyses, where below 4 GeV/c only the measured points from the TPC-TOF are used, while above 4 GeV/c only those from the TPC-TRD-TOF analysis are taken.

3.1 Analysis Software

The analysis software, called `HFE`, is part of AliRoot, the ALICE analysis and reconstruction framework. It makes use of the *ALICE Correction Framework* (`CORRFW`) [125]. The software package contains

- the track selection module

- the electron selection module

- container classes

- a class containing the code to correct the inclusive electron spectrum [126]

- utility classes

- the analysis task

The analysis tasks `AliAnalysisTaskHFE` selects electron candidate tracks and fills a multi-dimensional histogram for every selection step. For this a container class `AliHFEcontainer`, which is based on the existing container class `AliCFContainer`, is used. The container provides histograms for all track selection and electron identification steps and for all Monte-Carlo true electrons. For the filling the class `AliHFEvarManager` is used, which ensures that the container is filled with the same quantities in every part of the code. The histogram has five dimension, filled with the variables (p_t, η, ϕ, Z, mother), where mother is the mother species of the electron and Z is the charge number. The information on the mother species is only filled when analysing Monte-Carlo samples.

For the efficiency correction, the container is also filled with Monte-Carlo information for electron tracks created within a radius of 3 cm from the interaction point in the xy-plane in case Monte-Carlo information is available.

The track selection module uses the track selection classes implemented in the Correction Framework. Criteria which are not defined in the Correction Framework are implemented in a separate class `AliHFEextraCuts`. Cuts are arranged in different selection steps. A Correction Framework

Manager is used to filter tracks and select candidate tracks. All cut values applied are stored in an object of the class `AliHFEcuts`.

The electron identification module is designed in a way to allow combinations of different detectors or methods for the electron identification. For this an abstract base class `AliHFEpidBase` defines an interface which all detector PID classes have to implement. Two functions are important: `Initialise` contains possible initialisation code, `IsSelected` contains the electron identification code and returns the PDG[1] code for electrons in case the track could be an electron candidate. All detector PID classes are treated as independent. The class `AliHFEpid` does the steering of the electron selection by calling the functions `Initialise` for the initialisation and `IsSelected` for the candidate selection. The selection is applied in consecutive order as requested for the analysis so that candidates which are rejected by one detector are not taken into account in the following ones. The following detectors provide a electron selection class:

- TPC(`AliHFEpidTPC`)

- TRD(`AlIHFEpidTRD`)

- TOF(`AliHFEpidTOF`)

- EMCAL(`AliHFEpidEMCAL`) [127]

The use of a combined PID based on the bayesian approach is in preparation [128]. However, in order to study the behaviour of the different detectors in the electron selection on the first data, a combination of individual detectors as described above was chosen for this analysis.

In order to check the detector response, a quality assurance class containing histograms with basic information is implemented for every detector. The histograms are filled before the candidate selection in the detector and for selected tracks.

3.2 Selection of events and tracks

The analysis in proton-proton collisions at $\sqrt{s} = 7$ TeV is based on a dataset collected in summer 2010. This dataset consists of 185M minimum bias triggers. As trigger condition called "CINT1B", at least one hit in the SPD or in any of the V0 scintillators is required [90]. In addition, to reject background, the time measured for particles crossing the V0 detectors with respect to the nominal bunch crossing time
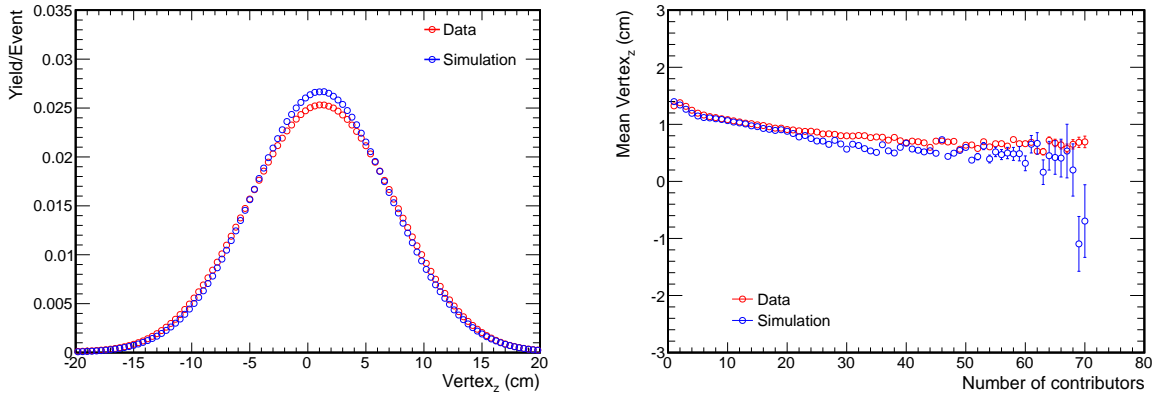
---

[1]   Particle Data Group

Figure 3.1: The distribution of the z-position of the primary vertex for data (red) and PYTHIA simulation (blue) is shown on the left side. Events are selected if the primary vertex is within $|z| < 10cm$. The right plot shows the mean position of the vertex in z-direction as function of the number of contributors to the vertex fit in data (red) and simulation (blue).

is requested to be positive. Events not fulfilling this condition are rejected. In total 125M events are selected.

For the remaining events further requirements are applied: pileup events, which contain more than one collision per event, are identified by the SPD and rejected in the analysis. A primary vertex must have been reconstructed, either with global tracks or with ITS tracklets with at least one contributor. Fig. 3.1 shows the distribution of the z-position of the primary vertex for Data and PYTHIA simulation. As can be seen from the plot, the measured distribution is reasonably well described in simulations. The distribution has a Gaussian shape, where the mean is slightly shifted by 1 cm from the centre of the experiment. Considering the mean of the distribution as function of the number of contributors to the vertex, a trend can be observed, which is also visible in simulations. The width of the distributions slightly differ (data: 6.22 cm, simulation: 6.02 cm). Events are selected if the z-position of the primary vertex is within $|z| < 10$ cm around the nominal collision point. This cut combined with the different width of the distributions result in slightly different event selection efficiencies in data and simulation. The fraction of events with a primary vertex selected by this cut is 88.6% in data and 89.7% in simulation.

Tracks are required to fulfil a set of selection criteria assuring a good track quality. These cuts are combined into selection steps. Cut steps making restrictions to particle identification detectors are applied only in case the detector is used in the analysis. The cut steps are:

- Basic track cuts in the ITS and the TPC:

  - Track is refitted in the TPC and the ITS

  - $\chi^2/TPCcluster < 3.5$

- At least 3 clusters in the ITS

- At least 70 clusters in the TPC

- Rejection of kink tracks. Electrons are stable particles, so they are not expected to produce kink tracks[2]. In some rare cases tracks are misidentified as kinks. In order to avoid double counting, kink daughter tracks are excluded. In case of misidentified kinks the kink mother contains only a fraction of the true number of TPC clusters. Since this has an impact on the electron identification, kink mother tracks are also excluded.

- DCA to the primary vertex. Tracks with a large DCA to the primary vertex in the order of one cm are not considered as a possible source of signal. Among those tracks could be fake tracks or cosmic ray particles passing the detector while an event is recorded. The DCA cut has to be loose enough so that it does not affect the signal. In this analysis tracks are required to have a maximum a DCA to the primary vertex of 1 cm in the in the radial plane and 2 cm in longitudinal direction.

- Requirement of a hit in the SPD. The requirement of a hit in the SPD has an influence on the amount of background electrons from γ-conversions in the detector material. If a hit in the first SPD layer is required, only electrons from photon conversions in the beampipe and a fraction of γ-conversions in the first layer where the daughter tracks produce a hit in this layer are selected. In case the requirement is a hit in the second or in any of the two SPD layers, then also electrons from γ-conversions in the first SPD layer and a fraction γ-conversions in the second layer are selected. In order to keep the amount of background electrons as low as possible, a hit in the first SPD layer is required.

- Requirement of a minimum number of tracklets in the TRD. As discussed in section 2.5 the performance of the pion rejection in the TRD depends on the number of tracklets assigned to a track. For the analysis including TRD, only tracks having at least four tracklets are considered.

Figure 3.2 shows the distribution of positively charged tracks with $p_\mathrm{t} > 2$ GeV/c as function of η and ϕ for the selection steps RecKineITSTPC (basic track quality cuts), Primary (rejection of kink tracks), HFEITS (requirement of the first SPD pixel) and HFETOF (acceptance in TOF). The distribution for negatively charged tracks looks similarly, however shifted in ϕ-direction by $\Delta\phi \approx 0.1$ due to the bending of tracks in the magnetic field. After the track quality cuts the sector structure of ALICE is visible showing

---

[2] When passing material, in particular the beampipe and the ITS, electrons emit bremsstrahlung, which could lead to kinks. Kinks however are reconstructed in the TPC, so a bremsstrahlung emission which happens before the TPC will not be reconstructed as a kink
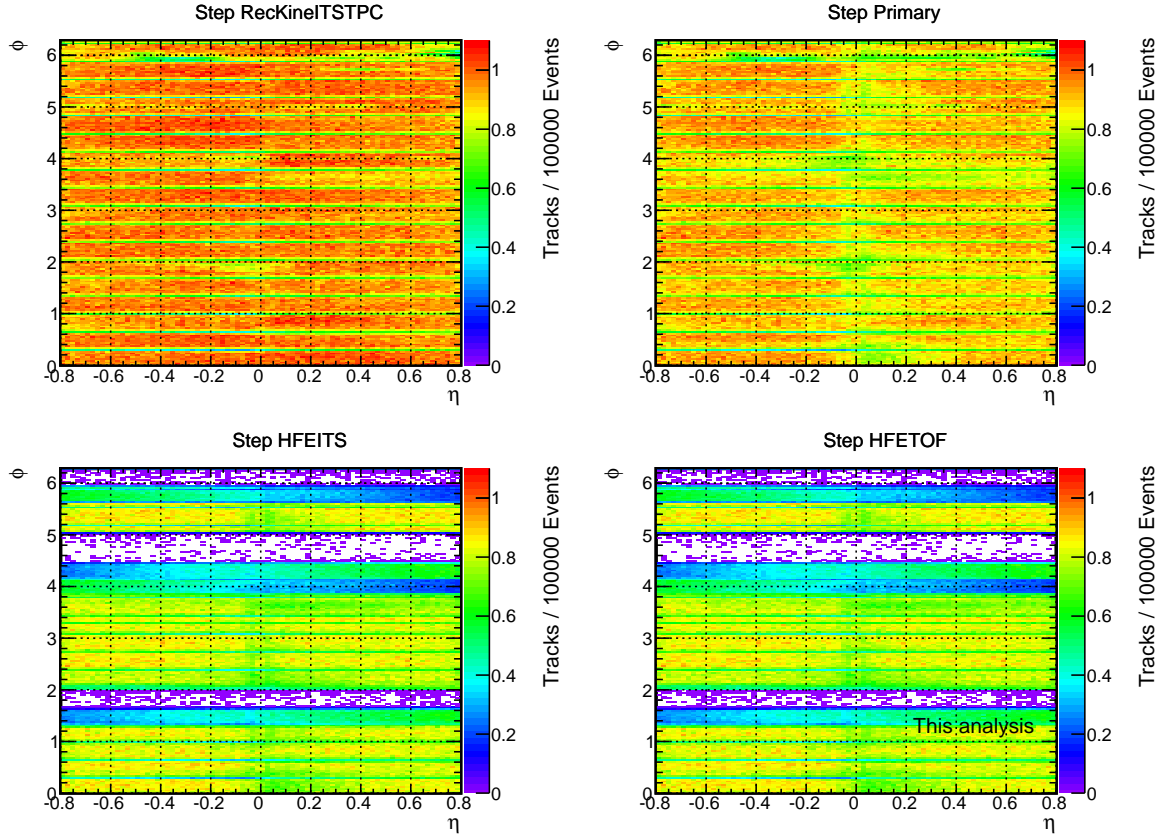
Figure 3.2: Distribution of tracks as function of η and ϕ after the selection steps RecKineITSTPC (basic track quality cuts), Primary (rejection of kink tracks), HFEITS (requirement of the first SPD pixel) and HFETOF (acceptance in TOF) for tracks with positive charge and $p_t > 2$ GeV/c.

fewer selected tracks in the sector borders. Dead areas are visible after the requirement on the first SPD pixel, where the total fraction of inactive pixels in this layer is 20% in 2010. One of the areas with inactive pixels is in front of an active TRD sector, namely number 17, which covers $5.93 < \phi < 6.28$. Figure 3.3 shows the distribution of positive charged tracks with $p_t > 2$ GeV/c for tracks with four, five and six tracklets after the previous track selection cuts. As can be seen from the plot, only few track in sector 17 (azimuthal coverage: $\Delta\phi < 0.05$) at the sector border contribute to the measurement. In the remaining acceptance, tracks with six tracklets are most abundant in the inner three stacks while in the outer two stacks the dominant fraction tracks have five tracklets.

3.3 Identification of electron tracks

After selecting candidate tracks which fulfil the selection criteria discussed above, electron candidates are selected using the ALICE central barrel detectors TPC, TRD and TOF. The detectors cover different momentum regions in which they are used for hadron rejection or electron selection.
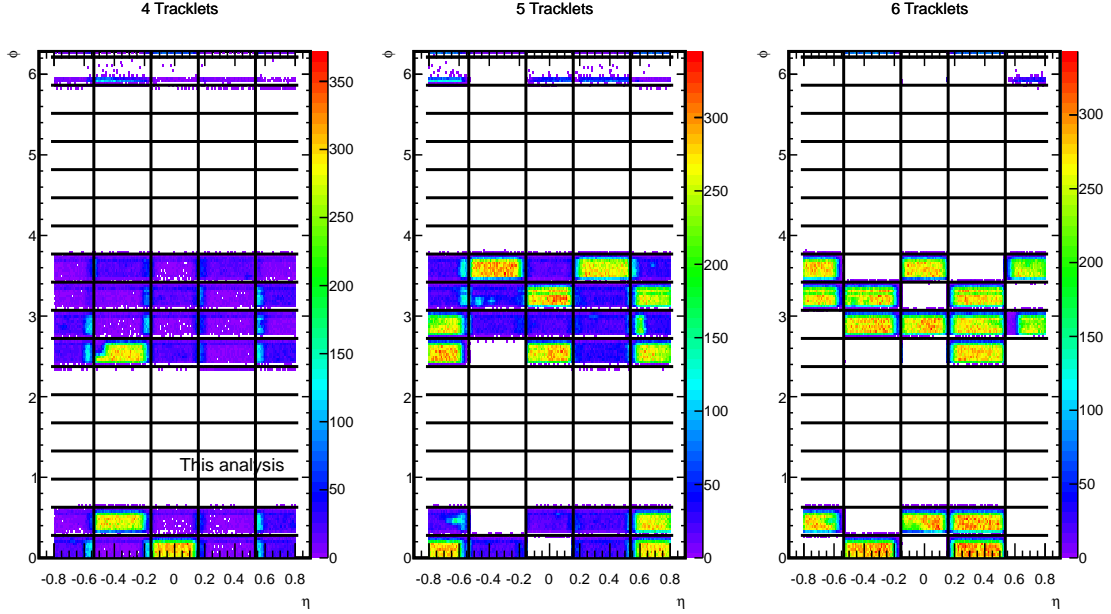
Figure 3.3: Distribution of tracks with positive charge and $p_\mathrm{t} > 2$ GeV/c in the TRD for four, five and six tracklets after the previous selection steps. Sector borders are indicated as black lines. White areas indicate holes, either sectors where TRD supermodules are not yet installed, or stacks where one or more chambers are inactive.

As a first step, TOF is used for the rejection of kaons and protons in the low-momentum region. This is important since their dE/dx bands cross the dE/dx band for electrons in the TPC and the TRD, making kaons and protons indistinguishable from electrons in the respective momentum regions. The crossing in the TPC happens for kaons at p $\approx$ 0.7 GeV/c and for protons at p $\approx$ 1 GeV/c.

The time-of-flight is measured for particles reaching TOF with a precision better than 100 ps. From this measurement the start time of the event t_0 has to be subtracted. The t_0, as described in section 1.3, is either obtained from the T0 detector or, if no information from the T0 detector is available, is calculated using the time-of-flight information from the tracks itself. In case neither of the two methods provide a measurement, t_0 is taken from the bunch crossing time provided by the LHC. The resolution of the t_0 determination has to be included in the time-of-flight resolution. For the selected data sample, the time-of-flight resolution is $\approx$ 160 ps [77]. The resulting time-of-flight t_{TOF} can be compared to the time-of-flight hypothesis t_{exp} for the different particle types electron, pion[3], proton and kaon, which is calculated based on the track length obtained in the reconstruction. The distribution of $t_{TOF} - t_{exp}$ for tracks from a given species has a Gaussian shape around 0, in case t_{exp} for the corresponding particle species is used [93].

---

[3]   A time-of-flight hypothesis is also calculated for muons. Due to the similar mass, it is indistinguishable from the time-of-flight hypothesis for pions.
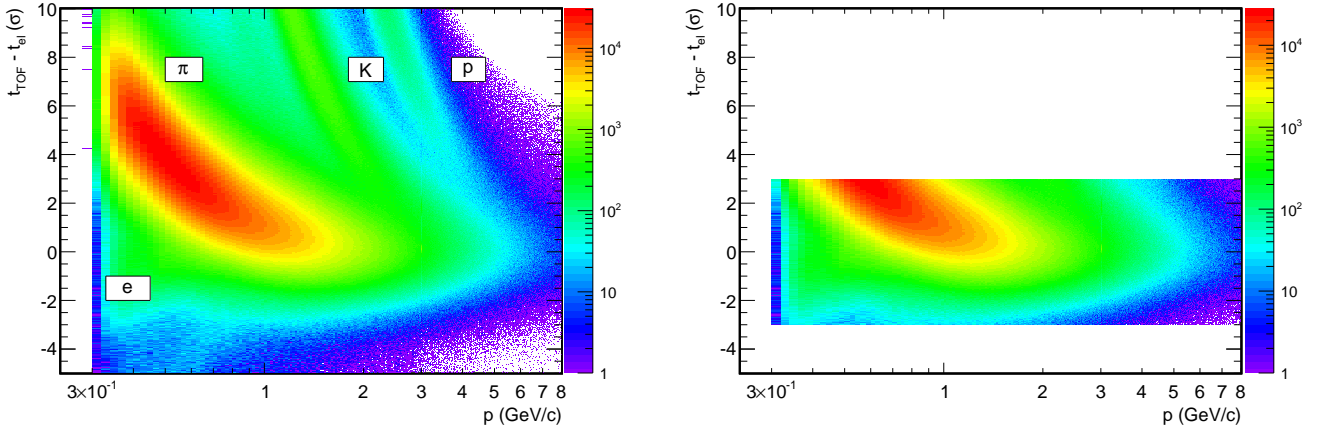
Figure 3.4: Time-of-flight signal expressed in numbers of σ to the time-of-flight hypothesis for electrons before (left) and after (right) cut (taken from [1]): lines indicate contributions from electrons+pions, kaons and protons. A 3σ-cut around the time-of-flight hypothesis for electrons is applied to derive the right plot.

For the rejection of protons and kaons a cut on the time-of-flight signal expressed in numbers of σ_{TOF} from the time-of-flight hypothesis for electrons is applied, where σ_{TOF} is the time-of-flight resolution. Figure 3.4 (left) shows the time-of-flight spectrum as function of the momentum. Due to the larger mass, kaons and protons have a larger time-of-flight than electrons at the same momentum and can be discriminated by the larger number of σs to the time-of-flight hypothesis for electrons. However, as soon as they become relativistic, they become indistinguishable from electrons by the time-of-flight measurement. This happens for kaons above a momentum of $\approx$ 1.5 GeV/c and for protons above $\approx$ 3 GeV/c. Pions become indistinguishable from electrons already at a very low momentum. A 3σ cut around the electron hypothesis is applied to select electron candidates. The time-of-flight distribution for selected tracks is shown in Figure 3.4 (right).

For tracks selected by TOF, the TRD electron likelihood calculated as described in section 2.5 renormalised to the sum of the electron and pion likelihood is used to reject a considerable fraction of pions. Figure 3.5 (left) shows the TRD electron likelihood for tracks having six tracklets as example. A cut providing an electron efficiency of 80% (see section 2.5.3) is applied to select electron candidates. The sample of selected electrons is shown in Figure 3.5 (right). Similar cuts are applied to tracks with four or five tracklets.

The final selection of electrons is done in the TPC. Figure 3.6 shows the energy loss in the TPC with respect to the electron hypothesis, normalised to the energy loss resolution $\sigma_{\text{TPC}-dE/dx}$. Due to the pion rejection provided by the TRD, electrons and pions are separated up to the highest momenta considered in the analysis. A cut on TPC dE/dx, which is defined as the mean of the dE/dx distribution of electrons, is applied. This cut, called "top-half TPC dE/dx cut", is indicated as lower black line in the plot. The
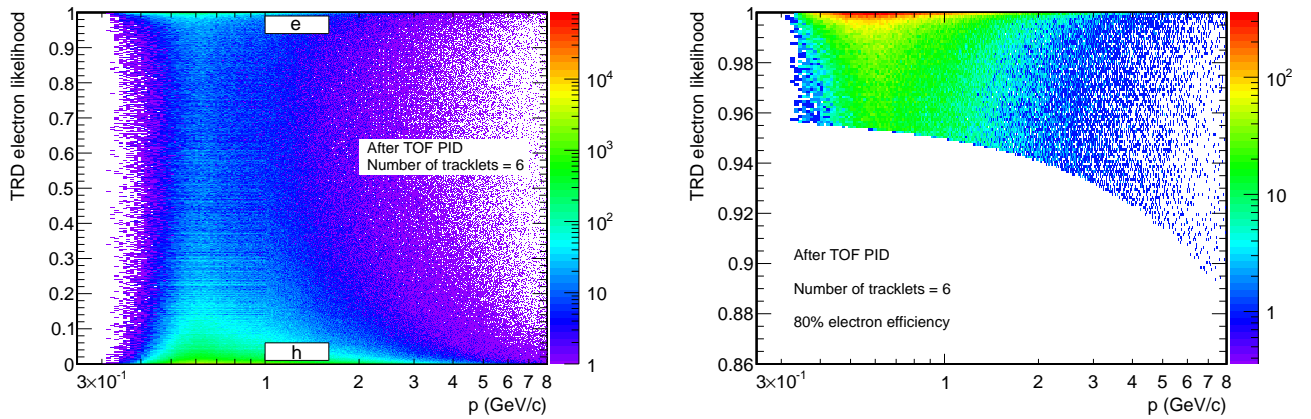
Figure 3.5: Electron identification in the TRD (taken from [1]): the electron likelihood distribution (see section 2.5) for tracks having six TRD tracklets after particle identification in TOF is shown in the left plot. A cut on the electron likelihood value providing 80% electron efficiency is applied to select electron candidates. The likelihood distribution of tracks surviving the cut is shown in the right plot.

Figure 3.6: Electron selection in the TPC (taken from [1]): the energy loss in the TPC with respect to the energy loss hypothesis for electrons and normalised by the dE/dx-resolution is shown versus the momentum for tracks selected by TOF and TRD. Lines indicate the selection band. The distributions are shown for tracks with six tracklets in the TRD after a cut providing an electron efficiency of 80% in the TRD.

Figure 3.7: η-dependence of the energy loss in the TPC for electron tracks with a momentum between 1 and 2 GeV/c.

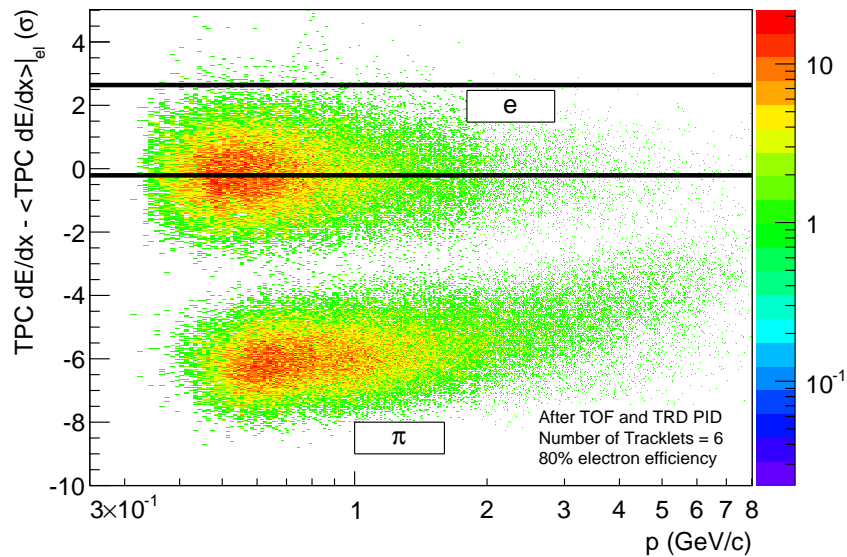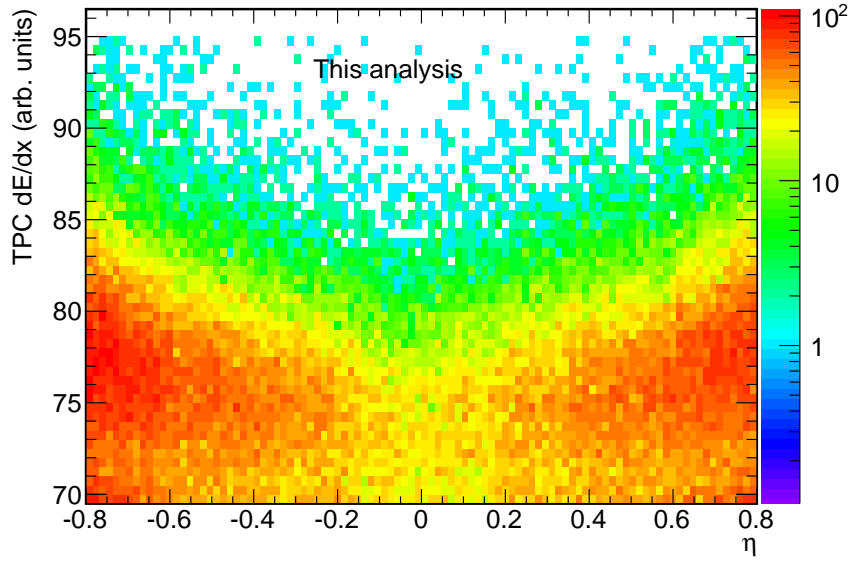cut is verified to be stable with the momentum and obtained from a multi-Gaussian fit performed in the p_{t}-range between 1 and 2 GeV/c [129]. The upper cut is defined to be at a distance of 3σ from the lower cut, indicated as the upper black line. Also the σ is derived from the multi-Gaussian fit. Particles with an energy loss within this band are finally selected as electrons.

Figure 3.7 shows the dependence of the energy loss in the TPC for electrons on η in the momentum range between 1 and 2 GeV/c for data. The energy loss for electrons is larger at larger η. This has an effect on the electron selection in the TRD: In case the whole η-range ($|\eta| < 0.8$) would be used in this analysis, then the mean of the dE/dx-distribution is moved to a higher value compared to using only a more central η-range (like $|\eta| < 0.5$). Consequently a dE/dx-cut as described above, which is tuned for the full η-range, prefers tracks at a larger η where the mean energy loss is larger. Since the outer stacks have a larger amount of bad chambers than central stacks, the relative abundance of tracks with 5 tracklets is increased by the cut on the TPC dE/dx. In order to avoid this effect, the analysis is restricted to $|\eta| < 0.5$. A correction of the dependence of dE/dx on η is in development [130].

The mean of the energy loss distribution for electrons in the TPC depends on the number of clusters used in the energy loss calculation for a given track [131]: the cluster charge in the TPC follows a Landau distribution. Out of the cluster charges for a single track, the energy loss is calculated using a truncated mean, using the lowest 60% of the clusters charges [132]. This cut removes the tail of the distribution and leads to a Gaussian dE/dx shape. In the energy loss calculation, clusters which are at the sector borders are not taken into account. They are only used for track reconstruction. Clusters can also be
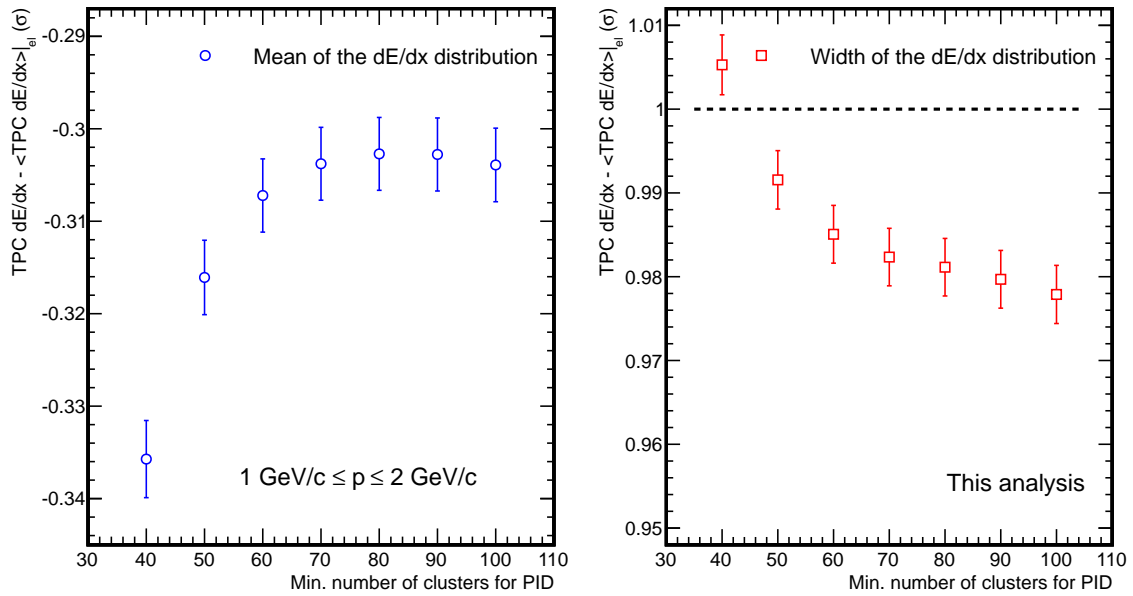
Figure 3.8: Dependence of the energy loss of electrons in the TPC on the number of clusters used in the energy loss calculation: in the left plot the mean of the energy loss distribution for electrons is shown as function of the minimum number of clusters used in the energy loss calculation. The width of the energy loss distribution is shown in the right plot. Mean and width are derived from a fit of a Gaussian function to the energy loss distribution in the momentum interval between 1 and 2 GeV/c.

missed in the reconstruction if the charge is below a given threshold. In this case for a given pad row a cluster is assumed to be produced if the neighbouring pad rows themselves contain clusters. A cluster is then created for this pad row with the charge of the threshold. These clusters are used only in the energy loss calculation and not in the tracking. When having fewer clusters available for the calculation of the truncated mean, the truncation artificially shifts the dE/dx to lower values [133].

Figure 3.8 shows the dependence of the mean energy loss for electrons in the TPC with $|\eta| < 0.5$ on the minimum number of clusters used for the energy loss calculation. Mean and σ are extracted from a fit of a single Gaussian function in the momentum interval between 1 and 2 GeV/c. As can be seen from the figure, the mean energy loss is increasing with the number of clusters used for the energy loss calculation until a saturation is reached.

A correlation between the number of clusters in the TPC and a requirement on the number of tracklets in the TRD has been observed. For momenta above 1 GeV/c, the curvature of tracks is small enough that tracks can be considered as straight. In this case, a requirement on the TRD prefers tracks which are in the centre of the sector, which have a higher number of clusters for dE/dx calculation than those at the sector borders. So the amount of tracks at the sector borders is reduced in this case compared to not
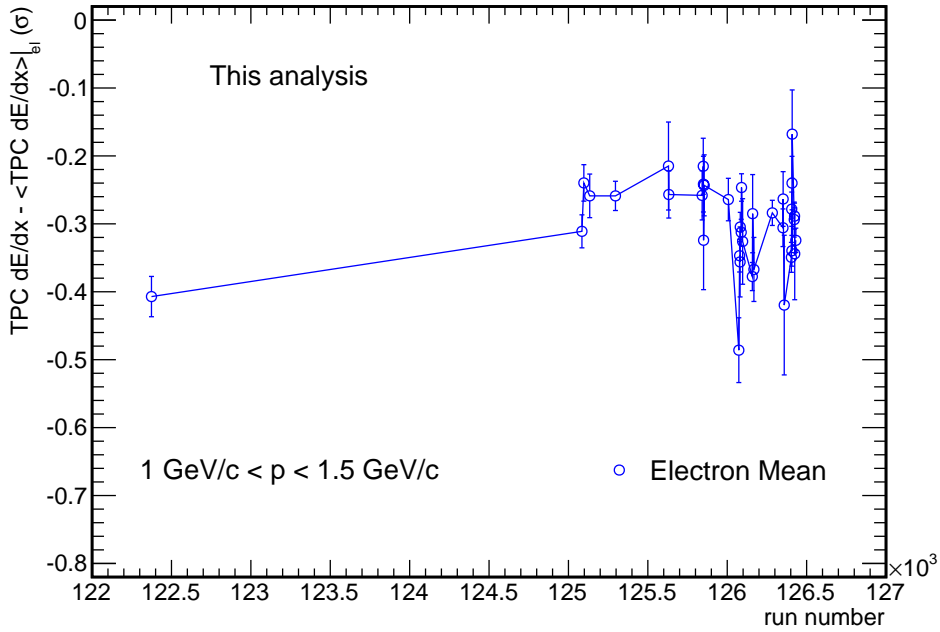
Figure 3.9: Dependence of the mean TPC dE/dx for electrons, obtained from a single-Gaussian fit of the TPC dE/dx in the p_t region between 1 and 1.5 GeV/c, on the run number.

applying requirements on the TRD [134]. This effect produces a difference in the energy loss distribution for electrons which shifts the mean. To have comparable energy loss distributions, tracks are required to have at least 80 clusters used for the energy loss calculation. With this cut, mean and width have been found to be compatible for the analysis with and without TRD.

The time-stability of the TPC dE/dx was checked for the sample used in this analysis in the momentum region between 1 and 1.5 GeV/c. Figure 3.9 shows the mean of the TPC dE/dx-distribution, obtained from a single Gaussian fit to the TPC dE/dx in the given momentum region, as function of the run number. A low-momentum region was chosen in order to have enough statistics to perform a good fit of the electron Gaussian on a run-by-run basis. The fit range for the single Gaussian fit was set to the range from -2.5σ up to 2.5σ. As can be seen from the plots, the points scatter around -0.3. Apart from the first run (122374), where the mean of the electron Gaussian is 3 σ away from the mean of the other runs, all runs are compatible within the errors.

The remaining hadron contamination is estimated from a fit of a function containing the dE/dx-contribution of different species to the dE/dx-spectrum. The electron component is described by a Gaussian function. Also for the kaon and proton component a good description by a Gaussian function is observed. For the sum of the pion and muon component, a Landau function multiplied with an exponential function was found to provide the best description of the tail in the dE/dx-distribution of
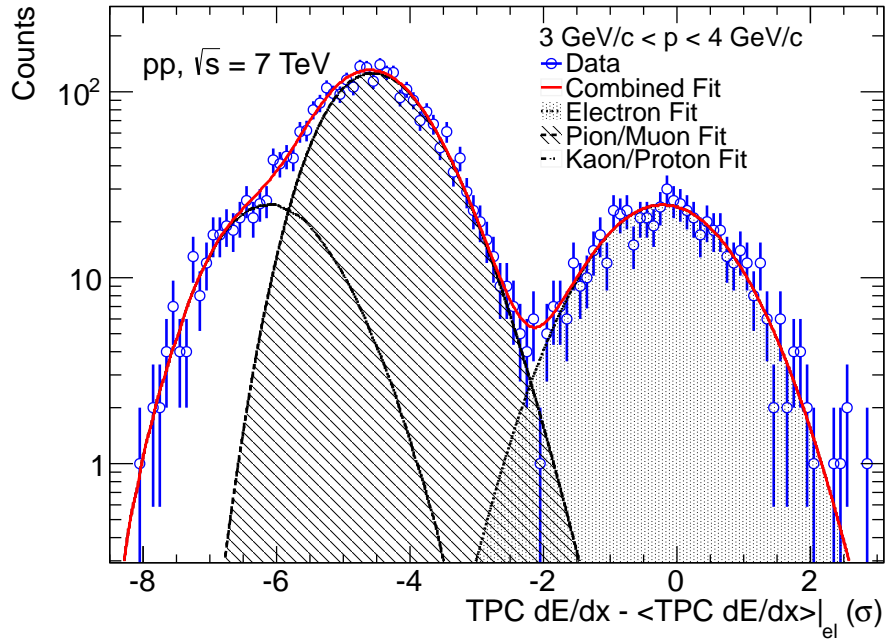
Figure 3.10: Example fit used to determine the hadron contamination (taken from [1]): the black line shows the combined fit. Contributions from the single components are indicated as shaded areas.

pions, which is the dominant component of hadronic background. Figure 3.10 shows an example of the fit applied to the momentum range 3 GeV/c < p < 4 GeV/c. As can be seen from the plot, the dE/dx distribution is well described by the combined fit, from which the single components are extracted. The hadron contamination is calculated as the ratio of the integral over the sum of all background components in the dE/dx-region used for the electron selection to the integral over the sum of all components in the same integration range. With the cuts applied in this analysis, the contamination is observed to be less than 2% up to 8 GeV/c [1]. For momenta above, the amount of candidate tracks is too small to derive a contamination value. In the further analysis, contamination is not subtracted.

3.4 Efficiency evaluation

We need to determine the efficiency of the track selection and the efficiency of the electron identification. The evaluation of the track selection efficiency including the electron identification with TOF is based on Monte-Carlo simulations. Two Monte-Carlo samples were used for the efficiency evaluation: a pp minimum bias sample and a signal-enhanced pp sample. Both samples are produced with the PYTHIA [135] event generator (version 6.421) using the tune *Perugia0* [136]. The detector simulation is done using GEANT3 (version 1.12). The signal-enhanced sample contains pp events where in addition to the
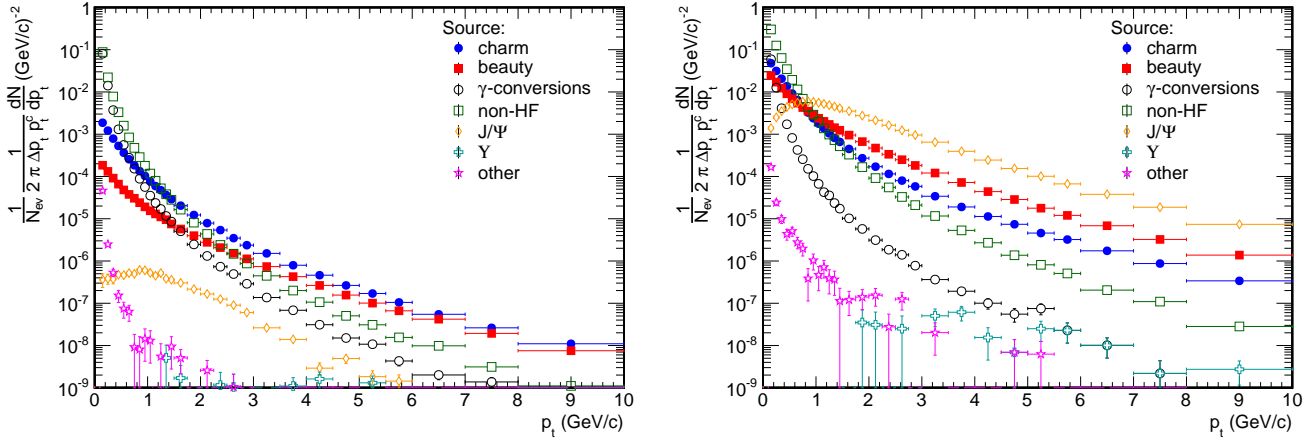
Figure 3.11: p_t distribution (generated electron-p_t) of true electrons in the minimum bias left and the signal-enhanced sample (right) based on Monte-Carlo information. p_t distributions are shown for electrons from open charmed and bottom hadron decays, γ conversions, other non-heavy-flavour background coming from sources described in section 3.8, quarkonia (J/ψ, Υ) and other background.

minimum bias condition one heavy-flavour quark pair (either charm or bottom) is produced, and where after the fragmentation at least one heavy-flavour hadron decays into an electron within $|y| < 1.2$. The advantage of the signal-enhanced sample is that it provides a high-statistics electron sample up to the highest p_t bins used in the analysis with a relatively small number of events (5.3 million events, compared to 153 million events in the minimum bias sample).

The efficiency is calculated as the number of selected electrons in a p_t-bin divided by the number of true electrons in the p_t-bin. Due to the short lifetime of heavy-flavour hadrons ($c\tau \approx 300\mu m$ for charmed hadrons and $\approx 500\mu m$ for bottom hadrons), electrons from heavy-flavour sources can be considered as primary. However, the electron sample also contains electrons from background sources which are eventually subtracted. These have to be included in the number of true electrons. Due to the requirement of the SPD first pixel, the production vertex of the electron has to be within 3 cm in radial direction from the primary vertex. Reconstructed tracks are only used in the efficiency calculation if the associated Monte-Carlo tracks fulfil the same conditions. Figure 3.11 shows the p_t-distribution of true electrons from various sources in the minimum bias sample (left) and the signal-enhanced sample (right). Electron sources are separated into open charm hadrons, open bottom hadrons, γ conversions, other non-heavy-flavour sources containing the Dalitz decays of π^0, η, η' and the dielectron decays of ρ, ω, ϕ (see Section 3.8), J/ψ, Υ and other electron sources, which are mainly decays of neutral and charged kaons, called K_{e3} (see Section 3.8). The enhancement of electrons from charm and bottom hadron decays can be seen in the signal-enhanced sample.
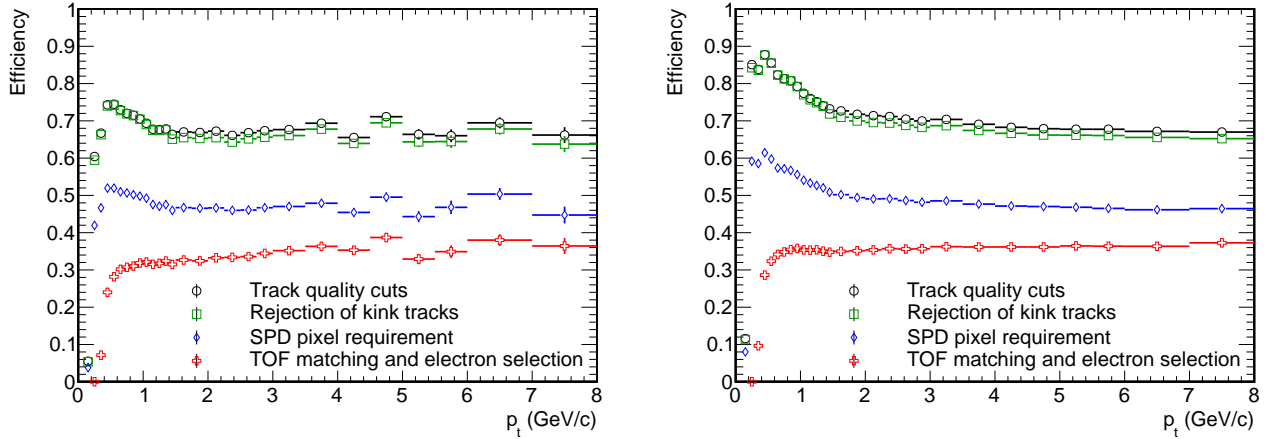
Figure 3.12: Track selection efficiency after the cut step for track quality, kink rejection, SPD pixel requirement and matching and electron selection in TOF. The efficiency is always expressed with respect to the number of true primary electrons based on the primary selection criterion. The left plot shows the efficiency derived from the minimum bias sample, the right plot the one from the signal-enhanced sample

Figure 3.12 shows the electron selection efficiency as described above for several cut steps for the minimum bias sample (left) and for the signal-enhanced sample (right). The cut steps are the basic track quality cuts, kink rejection, requirement of the first SPD pixel and the electron identification with TOF. At every selection step, the reconstructed p_t is taken for reconstructed tracks while for Monte-Carlo tracks the true p_t is taken. Electrons, however, loose energy due to Bremsstrahlung when passing detector material, in particular in the beam pipe and in the ITS, which leads to a measured p_t which on average is lower than the p_t with which the electrons are produced. As a consequence, the efficiency is higher at lower momenta since the number of reconstructed electrons in lower p_t bins also contains electrons produced with a higher momentum than actually measured. This can be seen from Figure 3.13. Here the ratio of the number of electrons in a given p_t bin with the reconstructed p_t over the amount of electrons with the true p_t in the same p_t bin is shown for the minimum bias and the signal-enhanced sample. Above 1 GeV/c the ratio is below 1, and it is increasing with decreasing p_t, which means that a certain amount of electrons produced with a given p_t is reconstructed in a lower p_t bin. In order to correct for this effect, the unfolding procedure described in section 3.5 has been applied. Comparing the two samples it can be seen that the shape of the distribution is different between the two samples, especially in the region between 1 and 3 GeV/c. The difference is coming from the different p_t shape of the minimum bias and the signal-enhanced sample. Due to the enhancement of electrons from the signal sources, the amount of electrons with higher p_t is larger in the signal-enhanced sample than in the minimum bias sample, which leads to a slight increase of electrons in the measured-p_t region around 1 GeV/c. Since the p_t-distribution is not known a-priori, this effect is included in the systematic error.
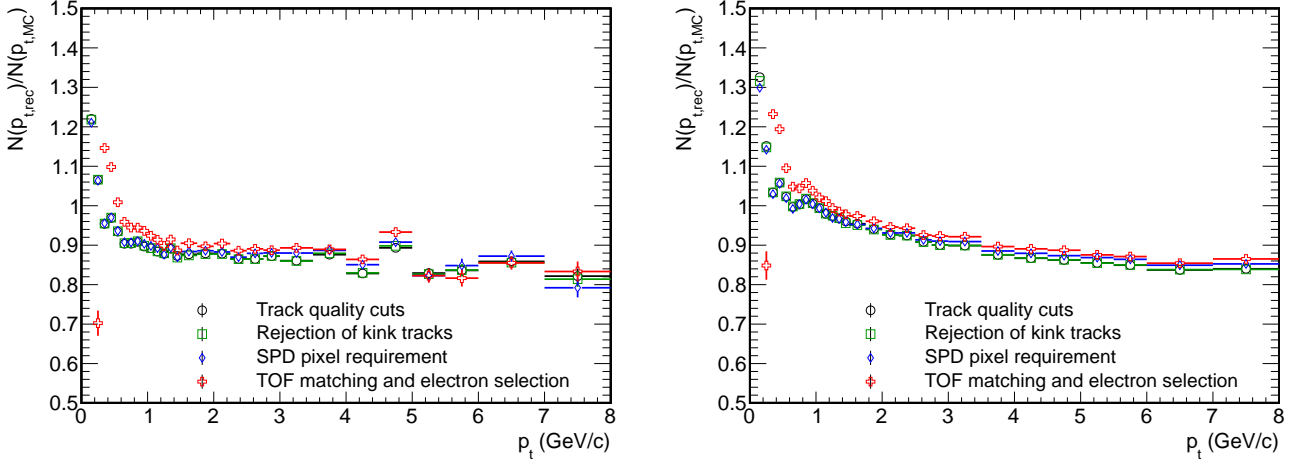
Figure 3.13: Influence of p_t reconstruction on the efficiency: shown is the ratio of the number of electrons with a given reconstructed p_t to the number of electrons with the true p_t for a given p_t bin for the minimum bias sample (left) and the signal-enhanced sample (right) for different selection steps.

When the TRD information is used, the efficiency for the cut on the number of TRD tracklets has to be included. Figure 3.14 shows the fraction of electron tracks selected in the previous steps (basic track cuts, kink rejection and SPD cluster requirement), which have four, five or six TRD tracklets, obtained from the minimum bias Monte-Carlo sample. This quantity can be interpreted as the efficiency of the cut on the number of TRD tracklets.

The efficiency of the electron identification is taken from data itself. As described in section 3.3, the TRD electron identification cut is tuned using electrons from γ-conversions so that the cut provides a flat efficiency versus p_t. We choose 80%. For the electron selection in the TPC the selection cuts are chosen to be the mean of the electron dE/dx distribution and $+3\sigma$, where σ is taken from a fit of a Gaussian function to the electron dE/dx distribution. From this an efficiency of 0.495 for the electron selection in the TPC is obtained. This leads to a total fixed electron selection efficiency of 0.396 which is used in the efficiency correction.

3.5 Correction of the inclusive electron spectrum

The p_t-differential invariant yield of inclusive electrons is calculated as

$$\frac{1}{2\pi p_t}\frac{d^2N}{dp_t dy} = \frac{1}{N_{MB}}\frac{1}{2\pi p_t^{cent}\Delta p_t}\frac{1}{N_{ch}}\frac{N_{el}(p_t)}{\epsilon_{reco}} \tag{3.1}$$
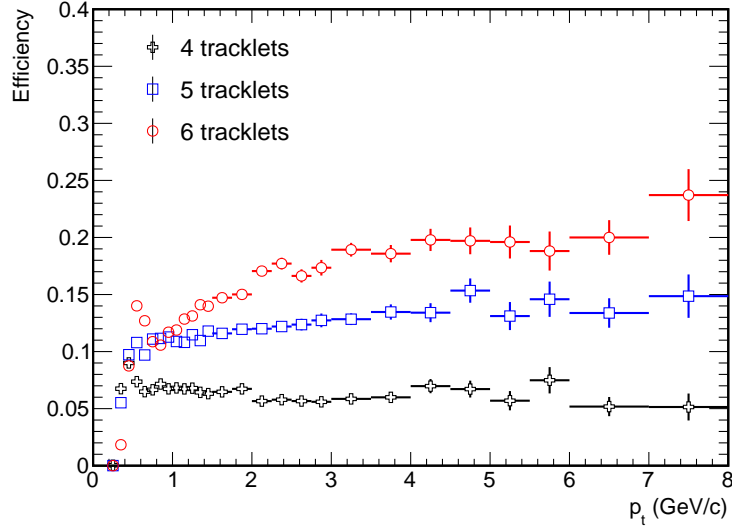
Figure 3.14: Efficiency of the requirement on the number of tracklets in the TRD: the fraction of electron tracks, selected by the previous cut steps (basic track quality, kink rejection and DCA, SPD pixel requirement and TOF selection), which have four, five and six tracklets is shown. The plot is done with the minimum bias Monte-Carlo sample. The geometrical acceptance of the TRD in the sample is 0.38.

where $N_{ch} = 2$ (number of charges), $N_{el}(p_t)$ is the raw number of electrons in a given p_t bin, ϵ_{reco} is the reconstruction efficiency, which includes the acceptance, and N_{MB} is the number of minimum bias events.

The efficiency is estimated as described in section 3.4. The total efficiency is the product of track selection and electron identification efficiency. In addition to the correction for efficiency, an unfolding procedure has to be applied because electrons loose energy in the detector material due to Bremsstahlung (section 3.4) The unfolding is based on the Bayesian theorem [137] and is done in an iterative approach. One starts with an arbitrary p_t-spectrum as a guess for the true p_t-spectrum. In this analysis, the true electron p_t-spectrum from simulation is used. A correlation matrix describes the correlation between measured and true p_t. Figure 3.15 shows the correlation matrix obtained with the minimum bias Monte-Carlo sample. The correlation matrix is created for true electrons before the electron identification step. Besides the diagonal elements describing tracks where the reconstructed p_t is in the same p_t bin as the true p_t, off-diagonal elements describing tracks where the measured p_t is in a lower or a higher[4] p_t bin

---

4   Due to the detector p_t resolution the measured p_t can also be slightly higher for a fraction of tracks. These tracks contribute to the neighbouring bins of the diagonal elements.
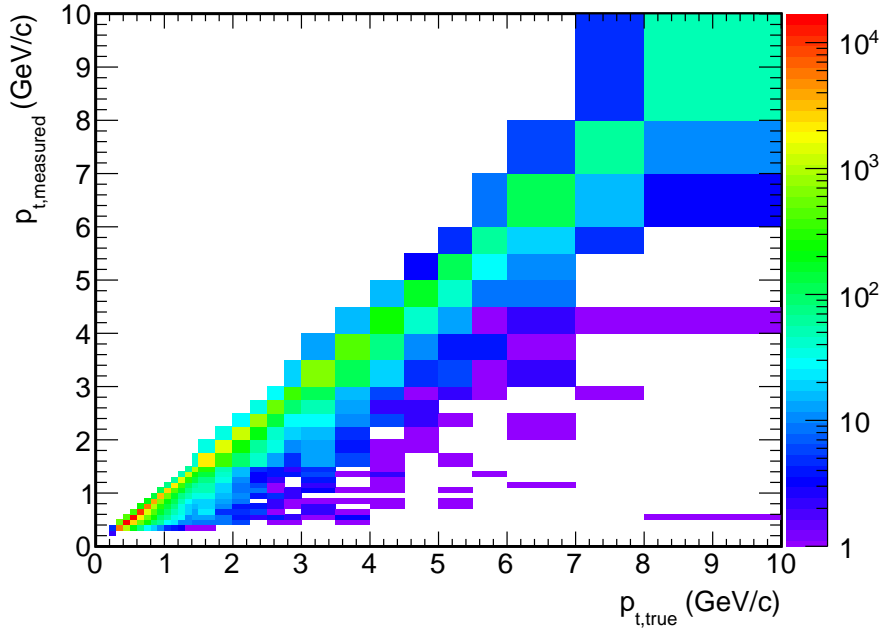
Figure 3.15: The correlation between measured and true transverse momentum p_t. The correlation is obtained from the minimum bias Monte-Carlo sample.

than the true p_t are visible too. Using the correlation matrix, the p_t spectrum in the next iteration step can be calculated as [137]

$$n_{t,i+1}(p_\mathrm{t,k}) = \sum_{j=1}^{n_{p_\mathrm{t}}} n_m(p_\mathrm{t,j}) * \frac{C(p_\mathrm{t,j}, p_\mathrm{t,k}) n_{t,i}(p_\mathrm{t,k})}{\sum_l^{n_{p_\mathrm{t}}} C(p_\mathrm{t,j}, p_\mathrm{t,l}) n_{t,i}(p_\mathrm{t,l})} \tag{3.2}$$

Here $n_{t,i}(p_\mathrm{t,k})$ is the true number of electrons in the k$^\mathrm{th}$ p_t bin in iteration step i, $n_m(p_\mathrm{t,k})$ is the measured number of electrons in the corresponding p_t bin and $C(p_\mathrm{t,l}, p_\mathrm{t,m})$ is the correlation between the measured p_t in bin l and the true p_t in bin m. The case i = 0 refers to the input p_t spectrum. After 10 iterations the procedure is stopped. In this analysis, this happens after five iteration steps. The unfolding procedure is implemented in the Correction Framework [138].

In the TPC-TRD-TOF analysis, the corrected inclusive electron p_t spectrum is produced for tracks with four, five and six tracklets separately. The final inclusive electron spectrum is obtained from the three independent spectra using an error-weighted mean.

In order to obtain the p_t-differential cross section of electrons from heavy-flavour hadron decays, the invariant yield of inclusive electrons after subtraction of the background has to be scaled with the minimum bias cross section. The minimum bias cross section was measured in a van der Meer scan in autumn 2010 [139, 140]. In a van der Meer scan [141] the *luminosity* is measured via the rate R of a reference

process as function of the separation of the two beams in x- and y- direction. The cross section of the reference process can be obtained via

$$\sigma_R = \frac{R(0,0)}{L} \tag{3.3}$$

As reference process a hit in both V0 detectors is required (V0AND). The cross section for the reference process σ_{V0AND} is determined to be 54.34 ± 1.9 (sys.) mb [142]. The minimum bias cross section is calculated via

$$\sigma_{MB} = \frac{N_{MB}}{N_{V0AND}} \sigma_{V0AND} \tag{3.4}$$

where N_{MB} is the number of minimum bias events and N_{V0AND} is the number of events for the reference process. The number of events has to be corrected for the event selection efficiency. After event selection cuts, 146M events are selected for the analysis. Out of these events, 125M events fulfil the V0AND condition. The event selection efficiency due to the restriction of the z-range of the vertex is 0.8814. Events which do not fulfil the V0AND condition do not have a reconstructed vertex. Therefore, the number is not corrected for the restriction in the z-range. The corrected number of minimum bias events is 159M, out of which 142M fulfil the V0AND condition. From this one obtains for the minimum bias cross section $\sigma_{MB} = 62.2$ mb.

3.6 Estimation of the systematic uncertainty

In order to estimate the systematic uncertainty on the inclusive electron spectrum, several cuts are modified with respect to the default configuration as described in section 3.2 and section 3.3. The spectra derived from this are corrected as described in section 3.5. For the correction the signal-enhanced Monte-Carlo sample is used. In the TPC-TRD-TOF analysis, apart from the electron selection in the TRD, the studies are done only for tracks with six tracklets.

Table 3.1 shows the cut variations applied in the TPC-TRD-TOF analysis. For the TPC, the lower cut on the dE/dx is chosen in a way that certain efficiency values (60%, 55%, 45%, 40%) are provided. The upper dE/dx cut is adapted as well. The results after cut variation are compared to the reference cut. As example, the comparison for the TRD electron identification cut is shown in Figure 3.16. In the left plot the comparison of all inclusive electron spectra including the reference spectrum is shown, in the right plot the ratios of the spectra with varied cuts to the reference spectrum is shown. As can be seen, the

Table 3.1: Cut variation for the determination of the systematic uncertainty: each cut is varied compared to the default configuration.

| Selection criterion	Default cut	Lower cut	Upper cut
Number of clusters in the ITS	4	3	5
Number of clusters in the TPC	120	100	140
Number of clusters for TPC dE/dx calculation	80	80	100, 120
DCA in radial direction (mm)	1	0.3, 0.5	2
DCA in z-direction (mm)	2	0.5, 1	4
TOF electron identification (nσ)	3	2	4
TPC electron identification lower cut (nσ)	-0.21	-0.45, -0.33	-0.09, 0.02
TRD electron efficiency cut	80%	75%	85%
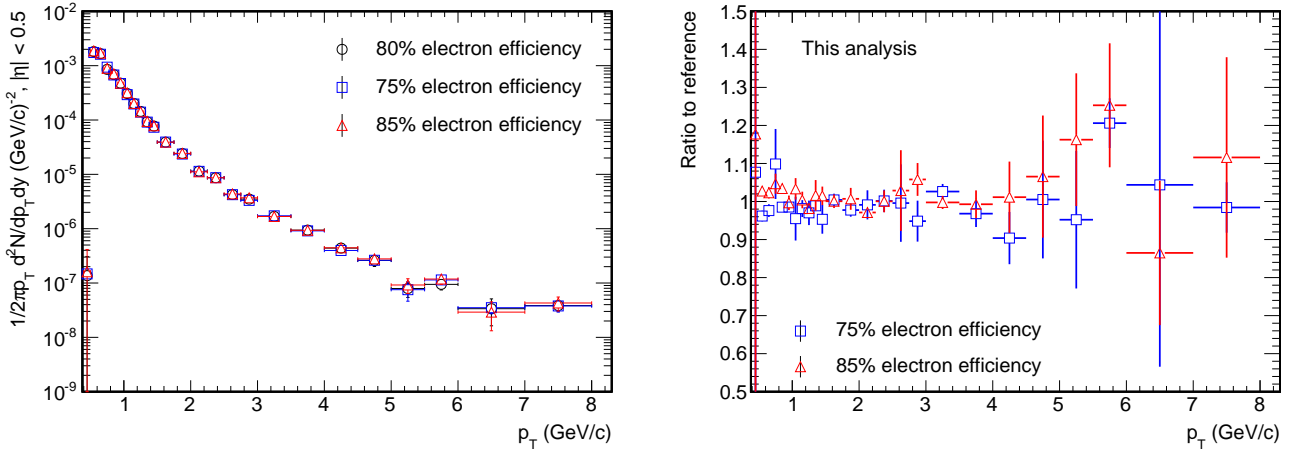
Figure 3.16: Comparison of the inclusive electron spectra using different TRD electron selection cuts to the reference spectrum: in the left plot the comparison of the corrected inclusive electron spectra is shown. The reference cut provides an electron efficiency of 80%. In the right plot the ratios of the spectra with the modified cut to the reference cut are shown.

spectra agree within 5% which is taken as systematic uncertainty of the cut. Ratios for the other selection criteria are shown in the appendix in section B.

The systematic uncertainties assigned to the selection criteria are listed in Table 3.2. For the one of the electron selection in the TPC a linear increase within 4 and 8 GeV/c is assumed. In Table 3.2 only the upper and lower value for this uncertainty is listed. In order to get a systematic uncertainty for the η range and the charge, the sample is split into two parts (positive and negative) for both cases. The resulting spectra are then compared to the reference spectrum done in the full η-range containing both positive and negative charge tracks. From this, a systematic uncertainty of 10% for both η and charge is deduced. A systematic uncertainty of 5% is assigned to the unfolding procedure. The total systematic uncertainty is calculated as the quadratic sum of the single components and is within 20% at 4 GeV/c

Table 3.2: Systematic uncertainties assigned to the selection criteria in the TPC-TRD-TOF analysis:

Selection Criterion	Systematic uncertainty (%)
Matching between TPC and ITS	2%
Number of clusters in the TPC $p_t < 6$ GeV/c	5
$p_t > 6$ GeV/c	10
Number of clusters for TPC dE/dx calculation	< 1
Number of hits in the ITS	5
DCA to the primary vertex in xy (z)	< 1
TOF electron identification	5
TPC electron identification $p_t = 4$ GeV/c	10
$p_t = 8$ GeV/c	16.7
TRD electron identification	5
Charge	10
η	10
Unfolding	5
Total: $p_t = 4$ GeV/c	20
$p_t = 8$ GeV/c	26

and 26% at 8 GeV/c. Since the final inclusive spectrum is combined from the TPC-TRD-TOF and the TPC-TOF spectrum, the systematic uncertainties from the TPC-TRD-TOF analysis are taken into account only in the p_t-range where TRD is applied in addition to TPC and TOF, which is within 4 and 8 GeV/c.

The same analysis is done for the TPC-TOF analysis in the p_t-range between 0.5 and 4 GeV/c [143]. Table 3.3 lists the uncertainties obtained. A total systematic uncertainty of 13% is obtained.

In addition to the systematic uncertainty on the inclusive electron spectrum, a systematic uncertainty of 3.5% [142] on the minimum bias cross section which is used in the normalisation has to be taken into account. Sources of the systematic uncertainty as described in [139] are the beam intensity, which is the dominant source of uncertainty, the beam separation in the luminosity determination, and the stability of the cross section of the reference process with respect to the bunch crossing index. This uncertainty is not included in the total systematic uncertainty for both analyses.

3.7 Invariant yield of inclusive electrons

The yield of inclusive electrons obtained after correction and normalisation (section 3.5) is shown for the TPC-TOF analysis in the p_t-range 0.5 GeV/c < p_t < 4 GeV/c and for the TPC-TRD-TOF analysis in

Table 3.3: Systematic uncertainties from the TPC-TOF analysis: The uncertainties are determined in the same way as done in the TPC-TRD-TOF analysis

Selection Criterion	Systematic uncertainty (%)
Matching between TPC and ITS	2
Number of clusters in the TPC $p_t < 0.7$ GeV/c	-6, +3
$p_t > 0.7$ GeV/c	3
Number of clusters for TPC dE/dx calculation	< 3
Number of hits in the ITS $p_t < 1$ GeV/c	-2, +4
$p_t > 1$ GeV/c	2
DCA to the primary vertex in xy (z) $p_t < 0.6$ GeV/c	-2, +0.5
$p_t > 0.6$ GeV/c	0.5
TOF electron identification	5
TPC electron identification	4
Charge	negligible
η	negligible
Unfolding	3
Total	≈ 8.5

the p_t-range 1 GeV/c < p_t < 8 GeV/c in Figure 3.17. The two spectra agree within the uncertainties in the p_t-range where the analyses overlap. The final p_t-differential invariant yield of inclusive electrons is constructed based on the two analyses, using the results from the TPC-TOF analysis in the p_t-range 0.5 GeV/c < p_t < 4 GeV/c and the ones from the TPC-TRD-TOF analysis in the p_t-range 4 GeV/c < p_t < 8 GeV/c.

3.8 Electrons from background sources

In addition to the electrons from heavy-flavour hadron decays, the inclusive electron spectrum contains electrons from other sources. These electron sources are:

- Dalitz-decays (π^0, η, η')

- Dielectron decays of light vector mesons (ϕ, ω, ρ)

- Dielectron decays of heavy vector mesons (J/ψ, Υ)

- Conversion of decay photons

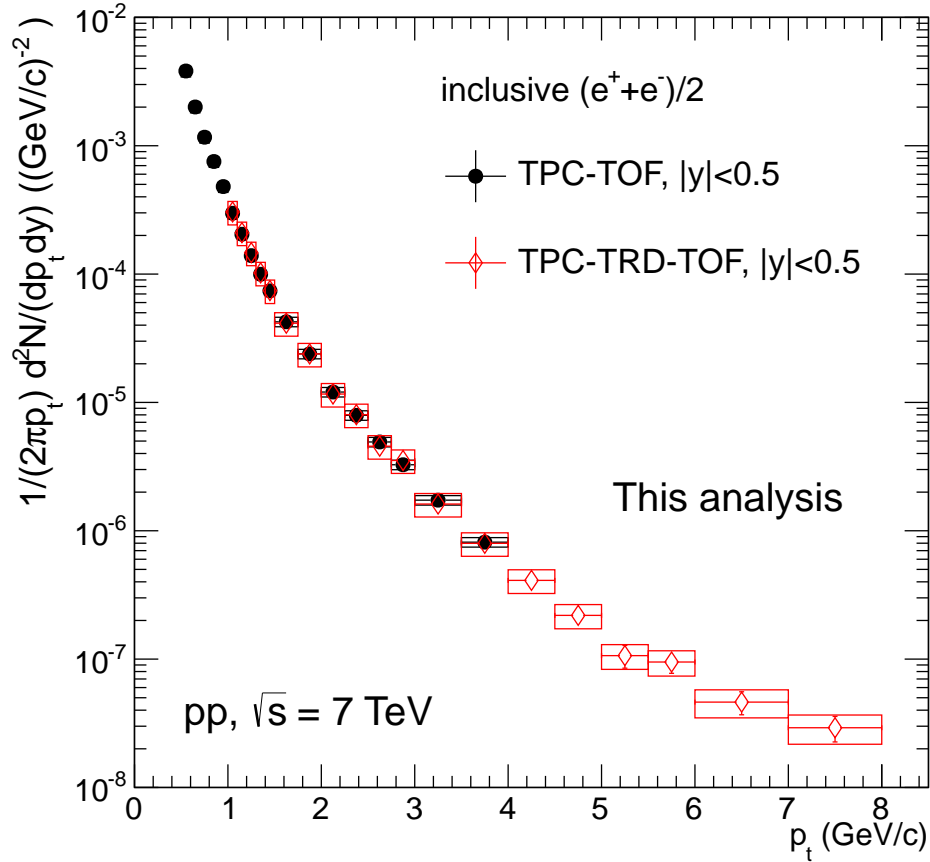- Conversion of real and virtual direct photons

Figure 3.17: p_t-differential yield of inclusive electrons, shown for the TPC-TOF (black) and the TPC-TRD-TOF analysis (red). The yield of inclusive electrons contains contributions from heavy-flavour hadron decays and from various background sources.

- Semi-electronic decay of the kaon

The amount of background electrons is determined with a statistical method. For this, a cocktail, which includes electrons from all the background sources mentioned above, is generated [144]. The cocktail generator is implemented within the AliRoot framework. Particles of each species are generated based on given p_t and y parameterisations. Parameterisations for p_t are discussed in this section, for y a flat distribution is assumed. Generated particles are decayed into electrons and other products by PYTHIA. Each electron track is weighted with the p_t-integrated cross section of the particle species. The p_t-spectrum of each component is normalised by the number of generated mother particles and divided by $\sigma = 62.2$ mb, which is the minimum bias cross section, to convert the p_t-differential invariant cross section into p_t-invariant inclusive yields. After generation, the cocktail of background electrons is subtracted from the inclusive electron spectrum to derive the heavy-flavour electron spectrum. The method is described in [1]. Figure 3.18 shows the multiplicity of background electrons as function of p_t. The contributions from

Table 3.4: Decay channels of light mesons included in the cocktail: the channels are sorted into dielectron decays, Dalitz decays and four-body decays. Branching ratios are quoted in brackets [3].

species	dielectron decay	Dalitz-decay	four-body decay
π^0	–	$\pi^0 \to \gamma e^+ e^-$ (1.17%)	–
η	–	$\eta \to \gamma e^+ e^-$ (7×10^{-3})	$\eta \to \pi^+ \pi^- e^+ e^-$ (2.68×10^{-3})
η'	–	–	$\eta' \to \pi^+ \pi^- e^+ e^-$ (2.4×10^{-3})
ω	$\omega \to e^+ e^-$ (7.28×10^{-5})	$\omega \to \pi^0 e^+ e^-$ (7.7×10^{-4})	–
ϕ	$\phi \to e^+ e^-$ (3×10^{-4})	$\phi \to \eta e^+ e^-$ (1.15×10^{-4})	–
ρ	$\rho \to e^+ e^-$ (4.72×10^{-5})	–	–

different sources, which are indicated as coloured lines, are discussed below.

For light mesons the cocktail is based on the π^0 p_t-spectrum measured with ALICE [145] in the decay channel $\pi^0 \to \gamma\gamma$. The measurement is done either using the electromagnetic calorimeter PHOS to detect the photons or reconstructing γ-conversions in the detector material with charged particle tracks in the TPC. The second method is especially important at low-p_t where calorimetry is difficult. With this a wide p_t-range from 0 up to 25 GeV/c is covered. The π^0 p_t-spectrum is fitted with a Tsallis-function [146]:

$$E\frac{d^3\sigma}{dp^3} = \frac{\sigma_{pp}}{2\pi}\frac{dN}{dy}\frac{(n-1)(n-2)}{nT(nT+m(n-2))}(1+\frac{m_t-m}{nT})^{-n}$$

(3.5)

with the free fit parameters n, T and dN/dy. m_t is the transverse mass defined as $m_t = \sqrt{m_0^2 + p_t^2}$, where m_0 is the rest mass of the π^0. The p_t-spectrum of the η-meson measured with ALICE [145] is treated in the same way. In order to include other light mesons (η', ω, ϕ, ρ) into the cocktail, m_t-scaling [147] is used. Table 3.4 gives an overview of the decay channels of the light mesons included in the cocktail. In the parameterisation obtained for the π^0 the mass m_0 is replaced by the mass of the meson. The p_t-spectra for the different mesons are normalised in the way that at 5 GeV/c the following ratios are obtained:

- ρ/π^0: 1.0 ± 0.3 [3]

- η'/π^0: 0.25 ± 0.075 [3]

- ω/π^0: 0.9 ± 0.27 [148]

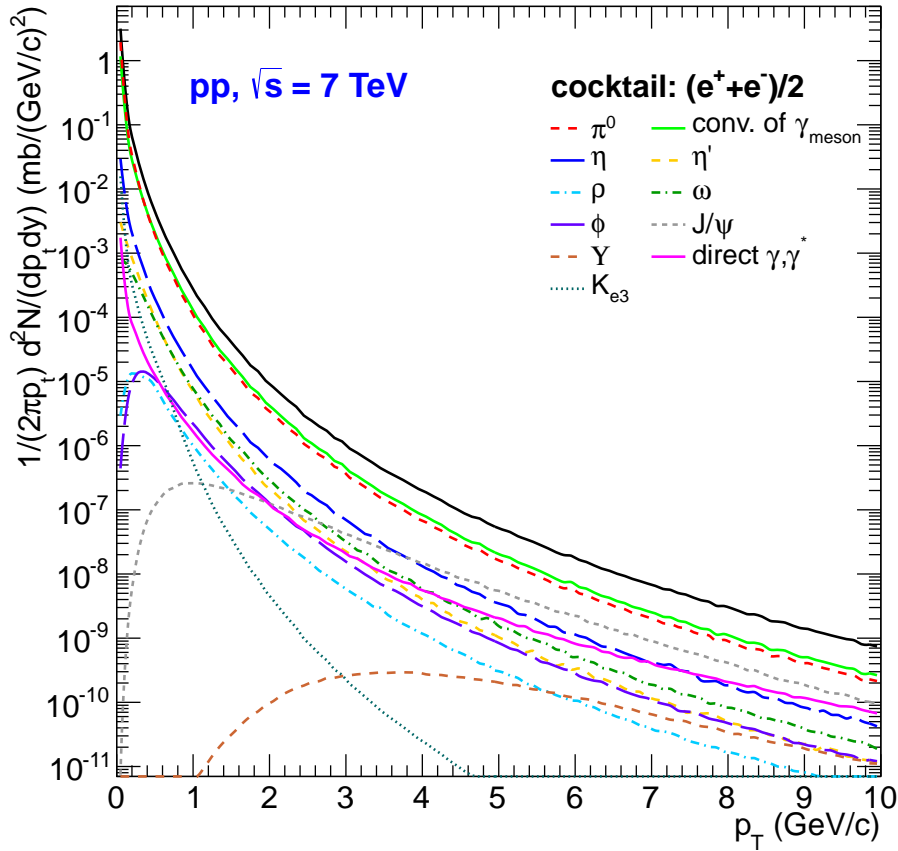- ϕ/π^0: 0.4 ± 0.12 [149]

Figure 3.18: Contribution of the different sources to the total electron background (taken from [1]): coloured lines show the yield of electrons from the various background sources, which are included in the cocktail, as function of p_t. The black line shows the sum of all background sources.

The ratios ω/π^0 and ϕ/π^0 are measured by PHENIX at $\sqrt{s} = 200$ GeV, the ratios ρ/π^0 and η'/π^0 are not measured in high-energy pp-collisions but are taken from jet fragmentation under the assumption that the particle ratios are the same also in pp-collisions at high-p_t. The main contribution from light mesons to the cocktail, as can be seen from Figure 3.18, is the π^0 input.

In addition to electrons from dielectron-, Dalitz- and four-body decays, light mesons also contribute to the cocktail via conversions of photons from the diphoton-decays. Compared to other decay channels, the branching ratio into two photons is large (π^0: 98.82%, η: 39.3% [3]). However, the conversion probability depends on the material budget relevant for the analysis. The material budget is studied using γ-conversions reconstructed with TPC tracks. Comparisons between conversions reconstructed in data and in Monte-Carlo simulations show that the detector material is well described in simulations, where the agreement is on a level of 4.5% [145]. Due to the requirement of the first pixel in the analysis, only γ-conversions in the beam pipe and part of the first SPD-layer contribute to the inclusive electron

spectrum. The fraction of the first SPD layer material contributing to the relevant material budget is obtained from a Monte-Carlo simulation to be 45%. The effective thickness of the first ITS layer is determined to be $X/X_0 = 1.14\%$, so an effective thickness of 0.513% is included into the converter material relevant for this analysis. The effective thickness of the beampipe is $X/X_0 = 0.26\%$. This leads to a total effective thickness of $(0.77 \pm 0.07)\%$.

The amount of electrons from photon conversions for a given meson is determined by the ratio

$$\frac{Conv}{Dalitz} = \frac{BR^{\gamma\gamma} \times 2 \times (1 - e^{\frac{7}{9}\frac{X}{X_0}}) \times 2}{BR^{Dalitz} \times 2} \tag{3.6}$$

where $BR^{\gamma\gamma}$ and BR^{Dalitz} are the branching ratios for the diphoton and the Dalitz decay, respectively, and $1 - e^{\frac{7}{9}\frac{X}{X_0}}$ is the conversion probability. The electron p_t-spectra from the contributing background sources (π^0, η, η') are scaled based on this formula.

In order to include the contribution from heavy-flavour quarkonia to the cocktail, the J/ψ p_t-spectrum measured by ALICE [97] and the Υ p_t-spectrum measured by CMS [150] are fitted with equation 3.5 and the parameterisation is included into the cocktail.

Direct photons, produced in hard scattering processes are not yet measured with any of the LHC experiments in the low-p_t region[5]. A parameterisation is motivated by NLO calculations [153]. The points derived are fitted with equation 3.5. The obtained parameterisation is included into the cocktail.

Weak decays of charged kaons ($K \rightarrow \pi^0 \nu_e e$), and neutral kaons ($K_L^0 \rightarrow \pi^\pm e^\mp \nu_e$), called K_{e3}, are a minor contributor to the background cocktail and only relevant in the low-p_t region below 1 GeV/c. Due to the lifetime of the kaon ($c\tau \approx 3.7$ m for charged kaons, ≈ 15.34 m for K_L^0 [3]) and the requirement of the first SPD layer in the analysis, only a little fraction of the decays give a contribution to the electron background. A parameterisation is obtained from a full Monte-Carlo simulation, including also the reconstruction.

In order to evaluate the systematic uncertainty of the cocktail, the points of the π^0-spectrum, which is also the dominant contributor to the uncertainty, are shifted up and down by its systematic error. The shifted spectra are fitted with equation 3.5. The parameterisations for J/ψ, Υ are treated in the same way. For the light mesons the ratios used for the normalisation are shifted by the systematic errors of the ratio. The systematic uncertainty of the conversions is based on the uncertainty of the material budget,

---

[5] CMS provides a measurement of direct photons for $p_t > 20$ GeV/c [151, 152]. Results are compatible with NLO pQCD calculations in this p_t region.

Table 3.5: Systematic error at a momentum of 5 GeV/c for different cocktail inputs.

Source	lower error	upper error (%)
γ-conversions	-3.5	3.5
π^0	-6	5.5
η	-2.8	3.2
η'	-0.8	0.8
ω	0.9	0.9
ϕ	-0.5	0.5
ρ	-0.2	0.2
J/ψ	-2.1	2.1
Υ	-0.4	0.4
direct photons	-1.9	1.9
K_{e3}	≈ 0	≈ 0
total	-8	7.9

which is directly propagated into the cocktail. A systematic error of 100% is assigned to the K_{e3}. For direct photons a systematic error of 50% is assigned.

After every variation, the cocktail is compared to the reference cocktail. The systematic errors for each ingredient are added in quadrature as done for the inclusive electron spectrum. Table 3.5 gives an overview of the systematic error of the different cocktail ingredients. As can be seen, the major contribution to the systematic error comes from the π^0 input spectrum. The total systematic error at this p_{t} region is $\approx 8\%$. Below 1 GeV/c the systematic error is largest and reaches $\approx 20\%$.

4 Results

4.1 Inclusive electron spectrum

As described in chapter 3 the inclusive electron spectrum is measured in pp collisions at $\sqrt{s} = 7$ TeV. In the low-p_t region up to 4 GeV/c the measurement is done with the "TPC-TOF" strategy while above 4 GeV/c the "TPC-TRD-TOF" analysis is used. Altogether a p_t-range from 500 MeV/c up to 8 GeV/c is covered. The spectrum contains contributions from electrons from heavy-flavour hadron decays as well as contributions from electrons from various background sources, calculated as described in section 3.8.

Figure 4.1 shows the comparison of the inclusive electron spectrum with the various cocktail sources. As can be seen from the plot, the dominant contribution at low-p_t comes from the π^0 Dalitz-decay and the photon conversions. Other contributions are so low in yield that they practically do not affect the inclusive electron spectrum. Towards higher p_t the dielectron decay of the J/ψ becomes important, too. The measured inclusive electron spectrum exceeds the background cocktail as expected. The excess originates from the semi-electronic decay of heavy-flavour hadrons. In the lower panel the ratio inclusive electrons over cocktail is shown. Towards low p_t this ratio approaches unity, meaning that the signal is small compared to the background. The ratio is increasing with p_t. At $p_t \approx 2$ GeV/c signal and background are of the same order, at higher p_t the contribution from signal is dominating. The systematic uncertainty of the ratio is calculated as quadratic sum of the relative systematic uncertainties of the inclusive electron measurement and the background in the given p_t-bin. The increase of the systematic uncertainty at 4 GeV/c is due to different systematic uncertainties of the TPC-TOF and the TPC-TRD-TOF analysis.

In order to obtain the p_t-differential cross section of electrons from heavy-flavour hadron decays, the background yield is subtracted from the yield of inclusive electrons. The systematic uncertainties of the yield of inclusive electrons and of the background cocktail are added in quadrature. The resulting invariant yield of electrons from heavy-flavour hadron decays is multiplied with the minimum bias cross section. Figure 4.2 shows the p_t-differential cross section of electrons from heavy-flavour hadron decays from this analysis (red).

In a separate analysis, called "TPC-EMCAL" the heavy-flavour electron spectrum is obtained using the detectors TPC and EMCAL for electron identification. The measurement is performed in the p_t-range 3 GeV/c < p_t < 7 GeV/c and in the rapidity range |y| < 0.6. In 2010, four out of ten EMCAL super-
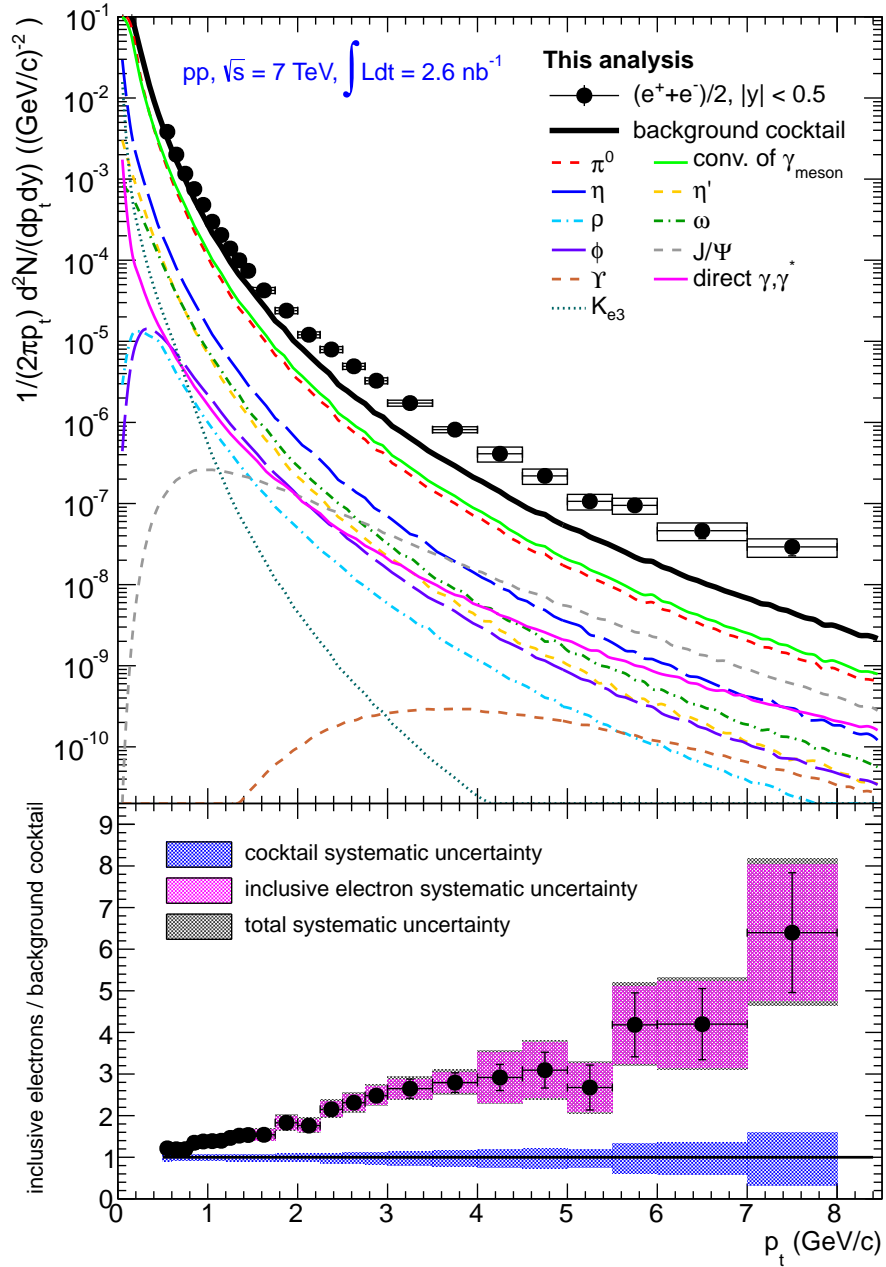
Figure 4.1: Inclusive electron spectrum from the TPC-TOF/TPC-TRD-TOF analysis compared to the cocktail of various background sources. Boxes indicate the systematic uncertainty on the inclusive electron measurement. Contributions from background sources are shown as lines. The ratio of inclusive electrons over the cocktail is shown in the lower panel.
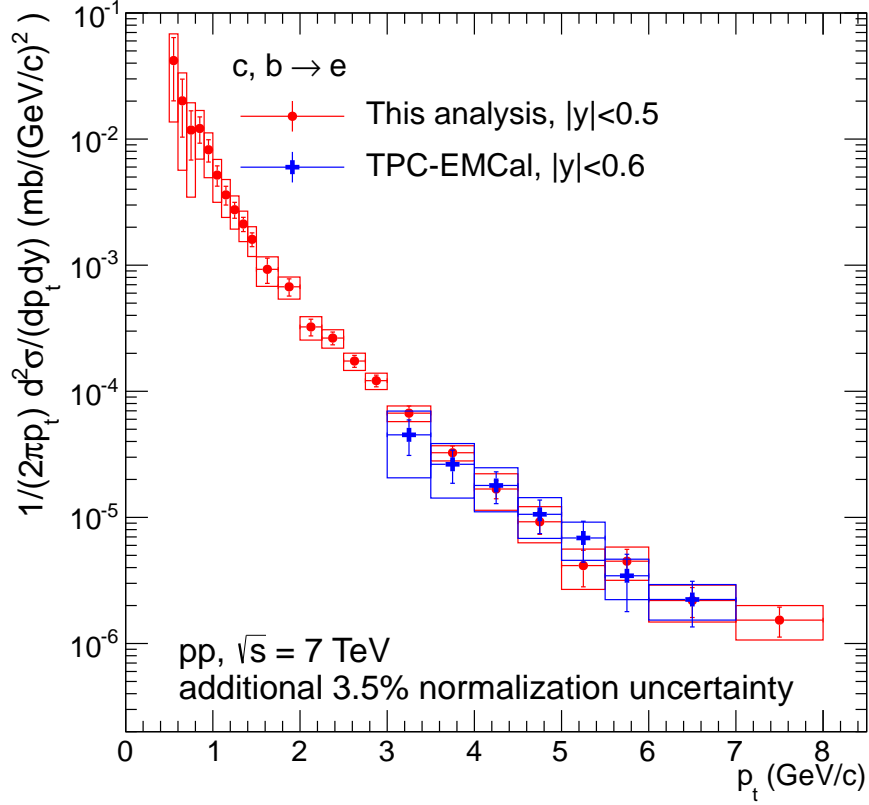
Figure 4.2: p_t-differential cross section of electrons from heavy-flavour hadron decays obtained with this analysis (red) and with the "TPC-EMCAL" analysis (blue). Boxes indicate the systematic uncertainty.

modules in two sectors were installed, leading to a coverage in ϕ of 40°. Since in front of the EMCAL a large fraction of pixels in the first SPD layer is inactive, a hit in either the first or the second pixel layer is required. This leads to a larger electron background from γ conversion due to the larger material budget which in this case includes the full first SPD layer and most of the second SPD layer. As done in the TPC-TOF/TPC-TRD-TOF analysis, the p_t-differential cross section of electrons from heavy-flavour hadron decays is obtained by the subtraction of the electron cocktail, adapted to the increased material budget, from the yield of inclusive electrons. The comparison between "TPC-EMCAL" analysis and the analysis described in detail in this thesis is shown in Figure 4.2. Both spectra agree within the uncertainties.

4.2 Comparison to the FONLL prediction

The p_t-differential cross section of electrons from heavy-flavour hadron decays is compared to a FONLL prediction [52, 154, 155]. The FONLL prediction is the sum of the predictions for charm quarks fragmenting into D-hadrons which subsequently decay semi-electronically (c $\rightarrow$ e), bottom quarks fragmenting

into B-hadrons which decay semi-electronically (b → e), and bottom quarks fragmenting into B-hadrons decaying into D-hadrons with a subsequent semi-electronic decay (b → c → e). The calculation is done in the pt range 0.5 GeV/c < p_t < 30 GeV/c and in the rapidity range |y| < 0.5. As set of *parton distribution functions* (PDF) CTEQ6.6 [57] is used. The fragmentation of bottom quarks into hadrons is based on the non-perturbative fragmentation function from Kartvelishvili [155–157]. For charm quarks the fragmentation function into D^0 or D^+ is model based on the fragmentation function into D^* [155, 158]. Based on the D^+/D^0 ratio measured by ALICE [77], the contribution from D^0 is 67.5% and the contribution from D^+ is 32.5%, where both D^0 and D^+ include contribution from D^* [158]. Contributions from D_s and Λ_c are not included [155]. The decay of hadrons containing a heavy quark into electrons is based on measured decay electron spectra [159]. The branching ratios are assumed to be 10.3% for D → e, 10.86% for B → e, and 9.6% for B → D → e [123]. The renormalisation and factorisation scales are set to $\mu_{r,f} = \mu_0$ with $\mu_0 = \sqrt{m^2 + p_t^2}$. As default values for the heavy quark masses, 1.5 GeV/c^2 is taken for the charm quark and 4.75 GeV/c^2 is taken for the bottom quark mass. In order to get a systematic uncertainty of the prediction, the renormalisation and factorisation scales and the quark masses are varied: as limits for the renormalisation and factorisation scales $1/2\mu_0$ and $2\mu_0$ with the constraint $1/2 < \mu_R/\mu_f < 2$ are chosen. For the heavy quark masses, the limits are 1.3 and 1.7 GeV/c^2 for the charm quark and 4.5 and 5 GeV/c^2 for the bottom quark.

The electron measurement is done with p_t bins of variable size. However, the FONLL prediction is a continuous function, evaluated at discrete steps. In order to be able to compare measurement and prediction, the prediction has to be converted into the binning applied for the measurement. To calculate values for FONLL in the binning applied, a parameterisation for the central prediction and the upper and lower limit was obtained. This is done by fitting a Tsallis function as shown in equation 3.5 to the central value of the FONLL prediction at $\mu = \mu_0$, the lower limit of the prediction at $\mu = \mu_0/2$ and the upper limit of the prediction at $\mu = 2\mu_0$. Figure 4.3 shows a comparison of the Tsallis fit to the FONLL prediction. The upper and central values of the prediction are described very well by the Tsallis fit over the full p_t range, with deviations of 5% at maximum. For the lower limit of the prediction, deviations up to 10% for p_t > 0.4 GeV/c have be observed, below 0.4 GeV/c the deviations become even larger, so that in this p_t-region the fit values are not reliable anymore. In case a modified Hagedorn function is used for the fit, the deviations are larger in all three cases, especially for p_t below 1 GeV/c.
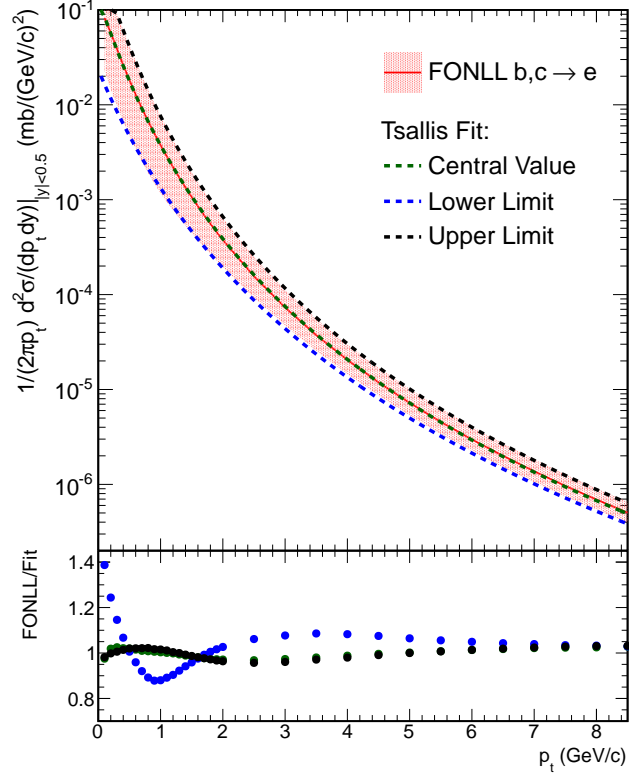
Figure 4.3: Comparison of the Tsallis fit to the FONLL prediction. Errors are assumed to be 1% of the value. The fit is done separately for the upper, lower and central value of the prediction. In the lower panel the ratio FONLL/Fit is shown for the three cases.

The bin value of the prediction at a given bin centre p_t^c for a binwidth Δp_t is calculated as

$$f^i = \frac{1}{\Delta p_t p_t^c} \int_{p_t^{min}}^{p_t^{max}} p_t g(p_t) dp_t \tag{4.1}$$

where the integration limits p_t^{min} and p_t^{max} are the p_t-limits of the bin and $g(p_t)$ is the result of the Tsallis fit. The bin error is calculated as the difference between upper respectively lower limit and the central value of the prediction.

Figure 4.4 shows the comparison between the measured p_t-differential cross section and the prediction from FONLL. The lower panel of the plot shows the ratio between the measurement and the prediction. Here the systematic uncertainty does not contain the uncertainty of the FONLL prediction, which is shown as a band around one. A good agreement of the prediction with the data is observed. At $p_t > 4$ the systematic uncertainty of the measurement is of the same size as the one of the FONLL prediction. From the ratio plot it can be seen that at low-p_t the measurement tends to be at the upper limit of the prediction.
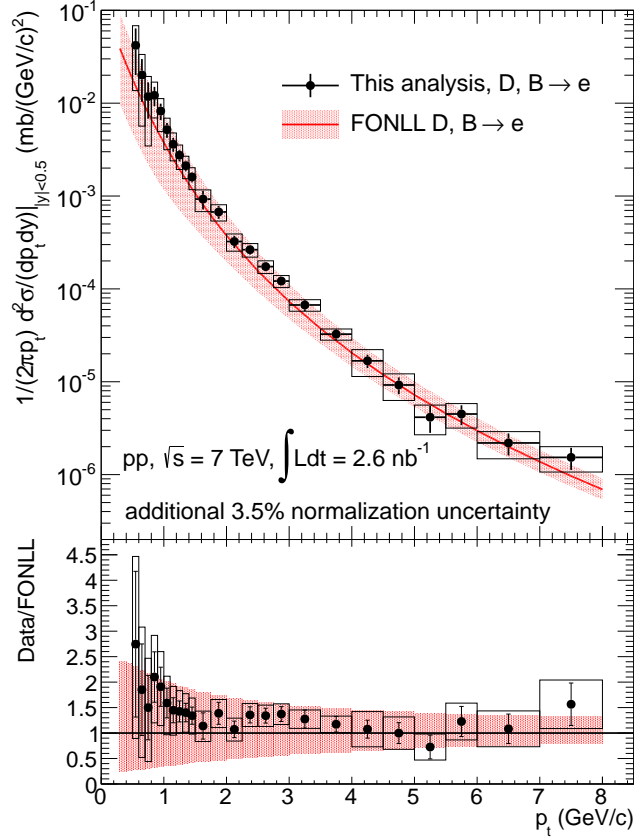
Figure 4.4: Heavy-flavour electron spectrum compared to the FONLL prediction. Boxes indicate the systematic uncertainty of the heavy-flavour electron spectrum. The prediction is shown as red band. In the lower panel the ratio data over FONLL is shown. The systematic uncertainty of the ratio does not contain the systematic uncertainty of the FONLL prediction.

The p_t-differential cross section of muons from heavy-flavour hadron decays was measured by ALICE at forward rapidity ($2.5 < y < 4$, five rapidity bins) [82]. The p_t-range of the muon measurement is $2~\text{GeV}/c < p_t < 12~\text{GeV}/c$, where the lower limit is implied by the muon trigger requirement the measurement (see section 1.3). In order to calculate y-differential cross sections of electrons or muons from semi-leptonic heavy-flavour decays in the p_t-range where the analyses overlap ($2~\text{GeV}/c < p_t < 8~\text{GeV}/c$), the p_t-spectra of both measurements are integrated in the corresponding p_t-range and normalised by the width of the rapidity intervals. Figure 4.5 shows $d\sigma/dy$ for the 3 rapidity bins from the two measurements, where the bin at -4 < y < -2.5 is obtained by reflecting the bin at positive rapidity with respect to 0. In the given pt-range the rapidity distributions from FONLL and from this analysis are in agreement.

In order to get the total charm cross section, the visible cross section at midrapidity, in the p_t-range $0.5~\text{GeV}/c < p_t < 8~\text{GeV}/c$, obtained from this analysis has to be extrapolated in the p_t down to $0~\text{GeV}/c$ and in rapidity. The visible cross section is
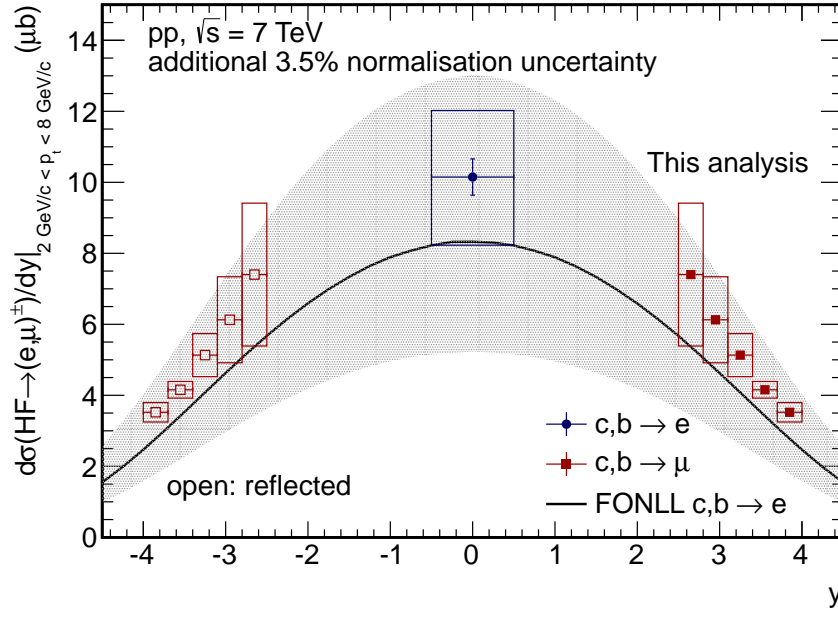
Figure 4.5: $d\sigma/dy$ of electrons and muons [82], integrated in the p_t-range $2\ \text{GeV}/c < p_t < 8\ \text{GeV}/c$, as function of the rapidity. Boxes indicate the systematic uncertainty. The grey band indicates the FONLL prediction.

$$\frac{d\sigma_{vis}(HF \to e)}{dy} = 37.7 \pm 3.2(\text{stat})^{+13.3}_{14.4}(\text{sys}) \pm 1.3(\text{norm})\mu\text{b}$$

The extrapolation was done using the p_t- and y-shape from FONLL. The FONLL curves for the central prediction and the mass, scale, and PDF variations were fitted using a Tsallis parameterisation. The parameterisations obtained were then fitted to the measured p_t-spectrum in the range $0.5\ \text{GeV}/c < p_t < 6\ \text{GeV}/c$ to get the normalisation. The fit was repeated for the central value after shifting the data points by the systematical uncertainty. The measured p_t-spectrum was integrated in the p_t-range $0.5\ \text{GeV}/c < p_t < 8\ \text{GeV}/c$, while the parameterisation was integrated in the p_t-range $0\ \text{GeV}/c < p_t < 0.5\ \text{GeV}/c$. The cross section of electrons from heavy-flavour hadron decays was found to be

$$\frac{d\sigma(HF \to e)}{dy} = 93 \pm 3.2(\text{stat})^{+30.5}_{-30.1}(\text{sys})^{+31.6}_{-11.5}(\text{extr}) \pm 3.3(\text{norm})\mu\text{b}$$

The uncertainty of the extrapolation is obtained from the variation of the parameterisations of mass, scale and PDF. Since the parameterisation of the FONLL shape using $\mu_f = 0.5$ and $\mu_r = 1$ was found not to be in good agreement with the data, it was not included in the calculation of the uncertainty from

scale variation. The uncertainty obtained from shifting the data points by the systematical uncertainty was added linearly to the systematical uncertainty of the midrapidity cross section. In the same way the cross section of electron from bottom hadron decays was determined to be [160]

$$\frac{d\sigma(H_B \to e)}{dy} = 8.5 \pm 0.3(\text{stat}) \pm 2.2(\text{sys})^{+0.5}_{-0.7}(\text{extr}) \pm 0.3(\text{norm})\mu b$$

After subtraction of the bottom component from the cross section of electrons from heavy-flavour hadron decays, the cross section of electron from charm hadron decays at midrapidity is found to be

$$\frac{d\sigma(H_C \to e)}{dy} = 84.5 \pm 3.5(\text{stat})^{+32.7}_{-32.2}(\text{sys})^{+32.0}_{-12.2}(\text{extr}) \pm 3.0(\text{norm})\mu b$$

According to eq. 29 in [161] the midrapidity charm cross section obtained is

$$\frac{d\sigma_c}{dy} = 889.2 \pm 36.9(\text{stat})^{+344.3}_{-339.2}(\text{sys})^{+337}_{-127.8}(\text{extr}) \pm 31.1(\text{norm}) \pm 36.7(\text{BR})\mu b$$

Here the branching ratio (br) used is $(9.6 \pm 0.4)\%$ [162]. The kinematical correction factor was determined via a PYTHIA simulation to be 0.982 [160]. For the extrapolation in y, the total cross section of FONLL was scaled by the ratio of the midrapidity charm cross section obtained in this analysis to the one obtained from FONLL. In order to obtain the uncertainty of the y-extrapolation on the total charm cross section, the upper and lower limits of the prediction were scaled in the same way. The uncertainty of the y-extrapolation is added linearly to the uncertainty of the p_t-extrapolation. After extrapolation in y, the total charm cross section is found to be

$$\sigma_c = 7.6 \pm 0.3(\text{stat}) \pm 2.9(\text{sys})^{+3.2}_{-2.5}(\text{extr}) \pm 0.3(\text{norm}) \pm 0.3(\text{br})\text{mb}$$

The total charm cross section extracted in this analysis is in agreement with the total charm cross section obtained by ALICE in the hadronic decay channel ($8.5^{+4.2}_{-2.5}$ mb) [163], ATLAS ($7.1^{+4.0}_{-2.2}$) [164] and LHCb (6.1 ± 0.9) [165], as well as the one predicted by FONLL ($4.8^{+6.4}_{-3.3}$ mb).

The p_t spectrum from heavy-flavour hadron decays is measured by ATLAS in the p_t range 7 GeV/$c <$ $p_\text{t} < 26$ GeV/c and the rapidity range $|y| < 2$ excluding $1.37 < |y| < 1.52$ [83]. ATLAS points are
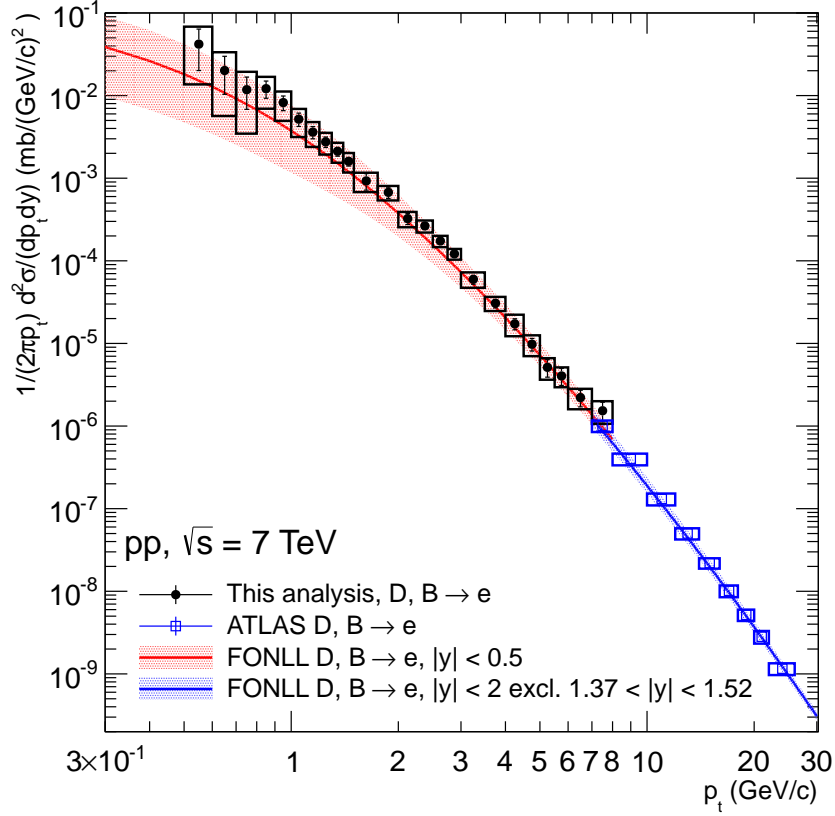
Figure 4.6: Heavy-flavour electron p_t spectrum combined from this analysis and the ATLAS measurement [83]. ATLAS points are scaled to match the ALICE rapidity coverage. Bands indicate the FONLL prediction. In the p_t region covered by ATLAS the prediction is treated in the same way as the measured points from ATLAS.

published as y-integrated differential cross section, $d\sigma/dp_t$, while the points from this analysis are shown as invariant cross section $1/(2\pi p_t)d^2\sigma/(dy\,dp_t)$. In order to compare the two measurements, the ATLAS points are scaled by $1/(2\pi p_t^c)$. To normalise to unit rapidity, the average over the ATLAS y-range is used. Since the rapidity distribution of electrons is not expected to be flat, in particular not towards large absolute values of rapidity, the scaled ATLAS cross sections are expected to be smaller than the cross sections from this analysis. Based on FONLL calculations the difference is estimated to be ≈7% for electrons from bottom hadron decays and ≈3% for electrons from charm hadron decays. Figure 4.6 shows the combination of the heavy-flavour electron spectrum from this analysis and the scaled ATLAS measurement. Only in the p_t bin between 7 and 8 GeV/c a cross section has been measured both with ATLAS and this analysis. In this p_t bin the measurements agree within the uncertainties, with the ATLAS point slightly lower than the point from this analysis. As mentioned above this is expected due to the different rapidity coverages of the two measurements. Combining the two measurements, the p_t-range

from 0.5 to 30 GeV/c is covered. A good agreement with FONLL is observed over the full momentum region covered by the two experiments.

4.3 Comparison to POWHEG predictions

A second prediction which is used for comparison is POWHEG (*Positive Weight Hardest Emission Generator*) [166–168]. POWHEG is a Monte-Carlo code which simulates hard processes based on NLO pQCD calculations, but does not perform the fragmentation of quarks into hadrons and the decays into electrons. In this analysis the hvq package [169] from POWHEG-BOX version 1.0 is used. The simulation generates heavy quark-antiquark pairs, which are imported into PYTHIA (v6.4.21) or HERWIG (*Hadron Emission Reactions With Interfering Gluons*) [170] (v6.510) which are responsible for the simulation of parton showers, fragmentation and decays. As PDF the set CTEQ6.6m [57] from LHAPDF (*Les Houches Accord PDF Interface*) v5.8.8b1 [49] is used. PYTHIA and HERWIG use the default configuration, however for PYTHIA also the tunes *ATLAS CSC* (tune 306) [171] and ATLAS MC09 (tune 330)[1] [172] are checked. For the central prediction, the masses of the heavy quarks are assumed to be 1.5 GeV/c^2 for the charm quark and 4.75 GeV/c^2 for the bottom quark. For both factoristation and renormalisation the scale $\mu_{r,f} = m_t$ is used. In order to obtain a systematic uncertainty, masses, factorisation- and renormalisation scales are varied. The charm quark mass is varied by 0.2 GeV/c^2 and the bottom quark mass by 0.25 GeV/c^2. Both scales are varied from $0.5m_t$ to $2m_t$. An example configuration file for the central prediction for bottom production can be found in appendix F.

The analysis is done both on POWHEG events to obtain the quark-p_t distribution and after fragmentation with PYTHIA/ HERWIG. In contrast to FONLL, the POWHEG prediction contains also contributions from D_s and Λ_c. The cross section is directly obtained from POWHEG. Figure 4.7 shows the quark-p_t distribution for charm and bottom quarks from POWHEG compared to FONLL. The distributions contain only one quark charge. As can be seen from the plot, for bottom production the p_t-spectrum predicted by POWHEG is slightly harder than the one predicted by FONLL. Within the uncertainties, however, both predictions are in agreement. For charm however, POWHEG predicts a cross section in the p_t-region between 5 and 10 GeV/c which is approximately a factor 2 lower than the one predicted by FONLL. For quark-p_t above 20 GeV/c the prediction from POWHEG is above the one from FONLL both for charm and bottom quarks.

---

[1] ATLAS MC09 is not implemented in the PYTHIA version used for this studies. The PYTHIA parameters for this tune were set in the steering program
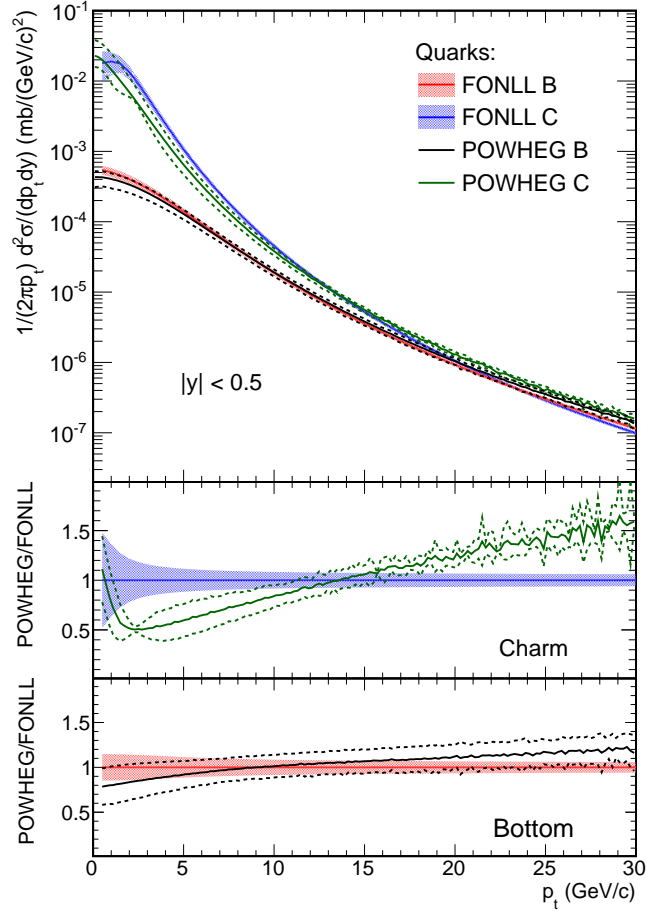
Figure 4.7: Quark-p_t distribution from POWHEG compared to FONLL. Dashed lines indicate the uncertainty bands from POWHEG. Lower panels show the ratio between POWHEG and FONLL for both flavours.

Figure 4.8 shows the comparison of the p_t-spectrum of electrons from semi-electronic heavy-flavour hadron decays between POWHEG and FONLL, including the three components D → e, B → e and B → D → e. The left plot shows the prediction when using PYTHIA as shower generator, while in the right plot HERWIG is used. As on the quark level, the prediction for bottom directly decaying into electrons is still compatible with FONLL within the uncertainty. The charm prediction is a factor 2 lower for POWHEG than for FONLL for p_t above 1 GeV/c, which then is also propagated into the prediction for the sum of the two flavour. The observation is similar for both shower simulations. It is interesting to note that the predictions for bottom hadrons decaying into electrons via charm hadrons is very different between PYTHIA and HERWIG although the contribution from these channels are small. For PYTHIA, results with the ATLAS CSC tune are compatible with the ones obtained using the default settings.

The comparison between between the p_t-spectra of electrons from semi-electronic heavy-flavour hadron decays from POWHEG, which is interfaced to either PYTHIA or HERWIG, and from this analysis is shown in Figure 4.9 (left) for different tunes of PYTHIA. Predictions from the POWHEG +PYTHIA
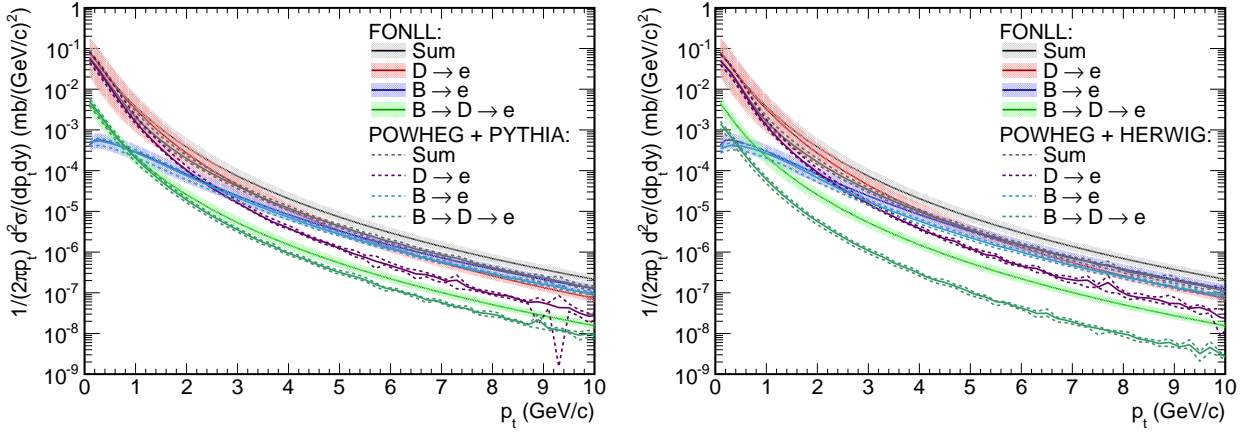
Figure 4.8: p_t-spectrum of electrons from heavy-flavour hadron decays obtained from POWHEG simulations. Contributions from the different sources D → e, B → e and B → D → e are shown separately. Bands indicate the FONLL prediction, lines the one from POWHEG. Dashed lines indicate the systematic uncertainty of the POWHEG prediction. In the left plot POWHEG is interfaced to PYTHIA, in the right plot to HERWIG.

with the PYTHIA tunes default and ATLAS CSC are similar, while using the tune ATLAS MC09 a larger cross section is obtained. Below 4 GeV/c all predictions are below the data by a factor 2 to 4. In this p_t region the contribution from charm is dominating, which already was found to be lower by a factor of 2 when comparing to FONLL. A non-negligible dependence on the PYTHIA tunes was also reported in [155], where predictions for D^+ production where compared for POWHEG interfaced to PYTHIA with the tunes default, Perugia0 (tune 320) and AMBT1 (tune 340). As can be seen from the right plot, which shows a comparison of the measurement to FONLL and POWHEG +PYTHIA using ATLAS MC09 tune, in this p_t region agreement is found to FONLL but not any of the POWHEG predictions used for comparison. When going to higher p_t, where the contribution from bottom becomes important, the deviations between the predictions and data become smaller. Comparing data to POWHEG+PYTHIA with the tune ATLAS MC09, an agreement within the uncertainties can be observed.
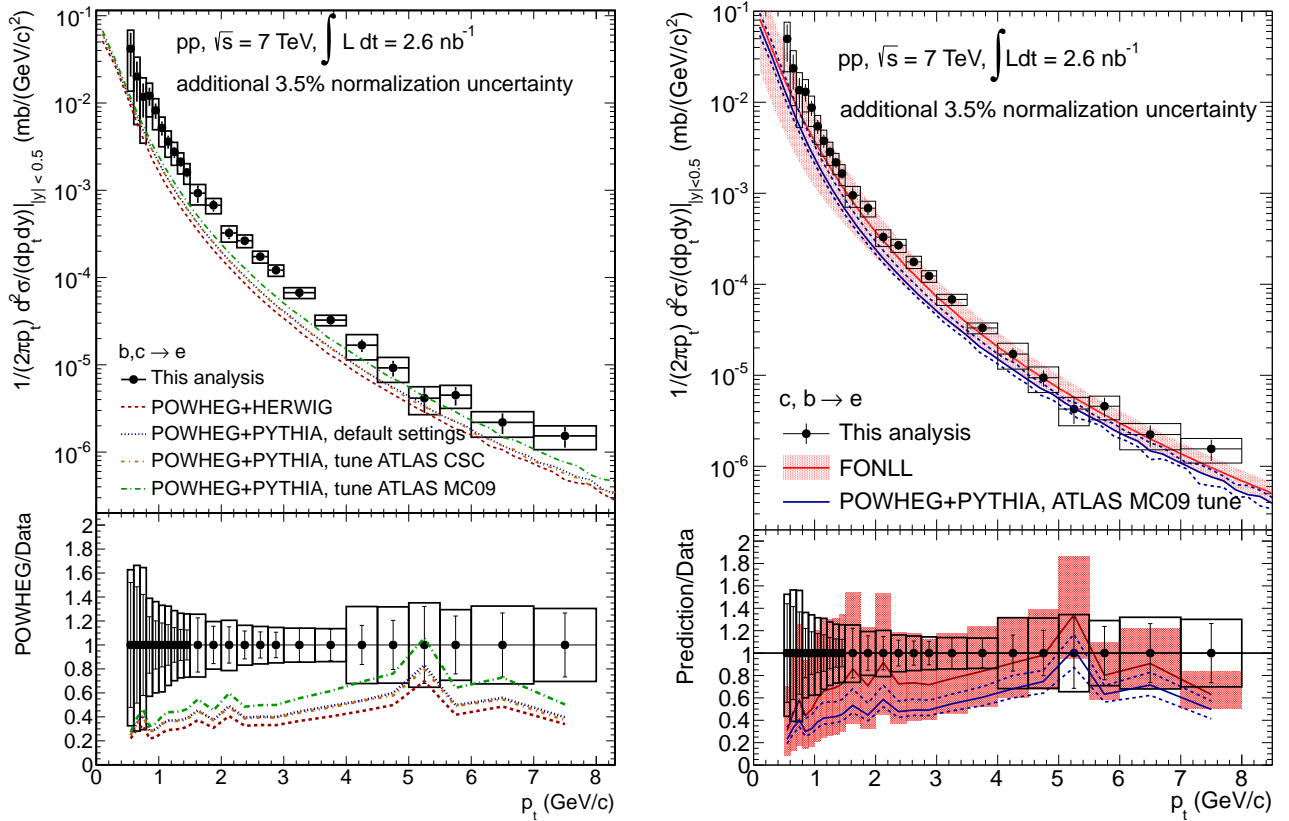
Figure 4.9: Comparison to POWHEG predictions: in the left plot the measured p_t-differential cross section of electrons from heavy-flavour hadron decays is shown in comparison to in comparison to the predictions from POWHEG+HEREIG (red) and POWHEG+PYTHIA for different PYTHIA tunes default (blue), ATLAS CSC (orange) and ATLAS MC09 (green). Boxes indicate the systematic uncertainty on the measurement. The ratio of the prediction to data is shown in the lower panel. In the right plot the measurement is shown in comparison to the FONLL (red band) prediction and to the POWHEG+PYTHIA prediction which uses the PYTHIA tune ATLAS MC09 (blue). Dashed lines indicate the upper and lower limit of the POWHEG+PYTHIA prediction. The ratio of the predictions to the measurement is shown in the lower panel.

5 Outlook: Measurement of electrons from heavy-flavour hadron decays in Pb–Pb collisions at $\sqrt{s_{NN}}$ = 2.76 TeV

As discussed in section 1.2, studies of heavy-flavour production in heavy-ion collisions provide insights into the properties of the hot dense medium created. A comparison of the nuclear modification factor for heavy-flavour hadrons and light hadrons can provide information about the energy loss mechanism in the medium as a function of the parton mass.

In fall 2010 ALICE collected a sample of 14 million minimum bias Pb–Pb events at $\sqrt{s_{NN}}$ = 2.76 TeV. For the determination of the collision centrality the V0 detector is used [35].

The reference spectrum from pp collisions used for the nuclear modification factor is obtained from the measured one at $\sqrt{s}$ = 7 TeV. In order to derive a reference at the Pb–Pb centre-of-mass energy, the reference was scaled with the help of FONLL [173]. As discussed in chapter 4 the ALICE measurement and the FONLL prediction are in good agreement. The analysis in Pb–Pb collisions is done separately for the different centrality classes, using the detectors TOF and TPC for the candidate selection. The procedure is the same as applied to pp collisions. However, due to contamination from hadrons in the p_t-range where the electron line and the proton and kaon line cross in the TPC, due to mismatches in TOF, the measurement currently is performed for $p_t > 1.5 \text{GeV}/c$. For the efficiency correction, a HIJING[1] [174] minimum bias MC sample is used. The cocktail describing electrons from background source is obtained in a similar way as the one obtained in pp collisions. The input is based on the charged pion measurement with ALICE [175] assuming $\pi^0 = (\pi^+ + \pi^-)/2$. Since there are no p_t spectra available for J/ψ and Υ, the two sources are not included in the cocktail. As input for direct photons the pQCD prediction for pp collisions [153] is used and scaled with the number of binary collisions.

Comparisons of the inclusive electron spectrum to the background cocktail in different centrality classes have shown an excess of the inclusive electron yield with respect to the cocktail in the p_t-range 1.5 GeV/c < p_t < 3 GeV/c, where the signal-to-background ratio is still low. The excess increases with centrality [176, 177]. In pp collisions this excess is not observed. A reason for this excess could be thermal radiation. Thermal radiation was observed with PHENIX [178], however at RHIC the temperature reached in Au–Au collisions is not sufficiently high to generate a significant direct radiation contribution

---

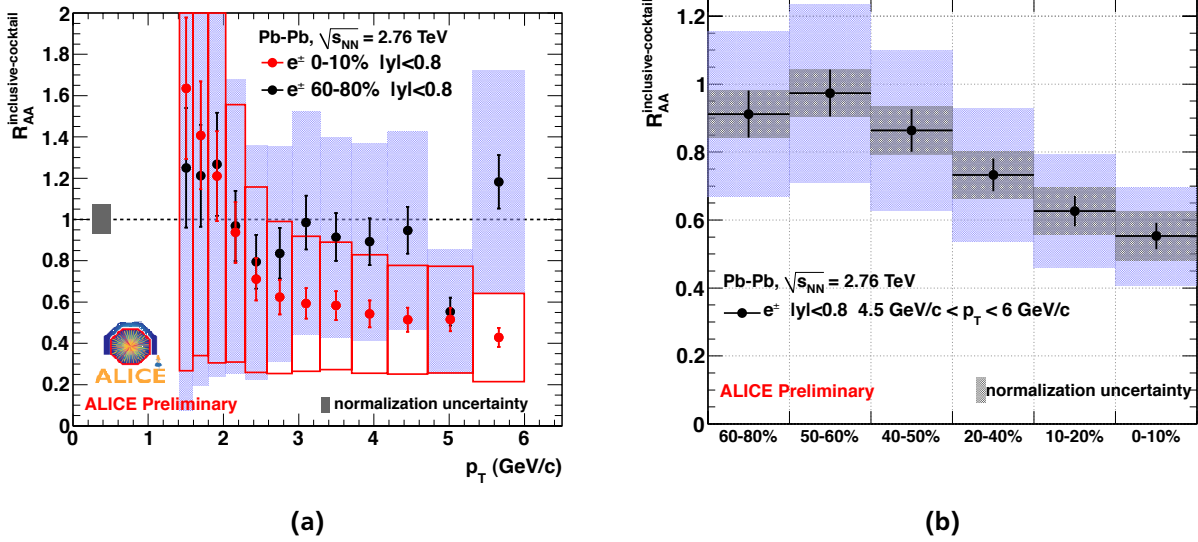[1]   Heavy Ion Jet INteraction Generator

Figure 5.1: Nuclear modification factor of electrons from heavy-flavour hadron decays (Figure taken from [177]). In (a) the nuclear modification factor is shown for as function of p_t for central (black) and peripheral collisions (red). Boxes indicate the systematical uncertainty. In (b) the nuclear modification factor integrated in the p_t-region $4.5 \, \mathrm{GeV}/c < p_t < 6 \, \mathrm{GeV}/c$ is shown versus the centrality.

to the single electron cocktail. At LHC, with a larger initial temperature the contribution from thermal radiation will be larger, however no measurement is available yet.

First preliminary results indicate a suppression of electrons from heavy-flavour hadron decays in most central collisions [177]. The suppression increases when going to more central collisions. Figure 5.1 shows the nuclear modification factor R_{AA} for electrons from heavy-flavour hadron decays. On the left plot (Figure 5.1a) the R_{AA} is shown as function of p_t for central and peripheral collisions, indicating the suppression in the most central collisions. Results however have large systematic uncertainties. Work is ongoing to improve the systematic uncertainty. On the right plot (Figure 5.1b), the R_{AA} is shown integrated in the p_t-region $4.5 \, \mathrm{GeV}/c < p_t < 6 \, \mathrm{GeV}/c$ as function of the centrality, indicating the increase of the suppression with increasing centrality.

A separation of the nuclear modification factors of electrons from charm and bottom hadron decays is in preparation. As for pp collisions, the separation is based on the distance of the electron to the primary vertex.

6 Conclusions

The measurement of the p_t-differential cross section of electrons from heavy-flavour hadron decays in proton-proton collisions at $\sqrt{s} = 7$ TeV is presented. The measurement, performed at midrapidity ($|y| <$ 0.5) in the p_t-region 0.5 GeV/$c < p_t < 8$ GeV/c, uses the central barrel detectors ITS, TPC, TRD and TOF of the ALICE apparatus.

A major contribution to the electron selection is provided by the TRD, which is used for the first time for electron identification in data. For this, the quality of the data collected in 2010 is studied. As outcome of the calibration, the TRD signal is observed to be stable in time for the data taking period used for this analysis. The pion rejection power is verified using a data-driven method based on electron and pion reference samples obtained from K_S^0-decays and γ-conversions. A pion rejection factor of 30 was achieved for tracks having six tracklets with a likelihood method based on the total charge deposit in a chamber.

The heavy-flavour cross section extracted from electrons is well described by perturbative QCD calculations. However, in case the results are compared to predictions from the POWHEG Monte-Carlo program, which is interfaced either to PYTHIA or to HERWIG for parton shower generation, fragmentation and decays, the data are above the prediction for both Monte-Carlo generators by up to a factor of 2. Our measurement complements the one performed by the ATLAS collaboration in the p_t-region 7 GeV/$c < p_t < 26$ GeV/c. The p_t-region covered by our analysis contains the dominant fraction of the charm as well as the bottom production cross section. By using the distance to the primary vertex as additional selection criterion, the contributions from charm and bottom hadron decays will be separated.

The presented measurement also serves as a reference for studies done in Pb–Pb collisions. First results of the measurement of the nuclear modification factor show a suppression of cocktail-subtracted inclusive electrons for $p_t > 3$ GeV/c, which is increasing with centrality, however the uncertainties are still large. Work on improving this measurement is ongoing.

A Differential cross section of heavy-flavour hadron decay electron production

Table A.1: Double-differential cross section of electron production is several p_t-bins measured with ALICE. The uncertainty of the cross section normalisation (3.5%) is not included in the systematical uncertainty.

| p_t (GeV/c)	$\frac{1}{2\pi p_t}\frac{d^2\sigma}{dp_t dy} \pm$ stat. $\pm$ sys. (μb/GeV/c^2)
0.50 - 0.60	$41.94 \pm 21.85^{+26.32}_{-28.28}$
0.60 - 0.70	$20.11 \pm 9.76^{+13.36}_{-14.46}$
0.70 - 0.80	$11.79 \pm 4.97^{+7.61}_{-8.32}$
0.80 - 0.90	$12.13 \pm 2.86^{+4.72}_{-5.20}$
0.90 - 1.00	$8.23 \pm 1.65^{+2.97}_{-3.29}$
1.00 - 1.10	$5.18 \pm 0.95^{+1.71}_{-2.03}$
1.10 - 1.20	$3.61 \pm 0.61^{+1.17}_{-1.22}$
1.20 - 1.30	$2.75 \pm 0.40^{+0.79}_{-0.82}$
1.30 - 1.40	$2.12 \pm 0.27^{+0.56}_{-0.58}$
1.40 - 1.50	$1.60 \pm 0.20^{+0.41}_{-0.43}$
1.50 - 1.75	$0.92 \pm 0.21^{+0.24}_{-0.25}$
1.75 - 2.00	$0.67 \pm 0.10^{+0.13}_{-0.15}$
2.00 - 2.25	$0.32 \pm 0.05^{+0.067}_{-0.069}$
2.25 - 2.50	$0.26 \pm 0.03^{+0.043}_{-0.045}$
2.50 - 2.75	$0.17 \pm 0.019^{+0.027}_{-0.027}$
2.75 - 3.00	$0.12 \pm 0.013^{+0.018}_{-0.018}$
3.00 - 3.50	$0.067 \pm 0.0093^{+0.0094}_{-0.0096}$
3.50 - 4.00	$0.033 \pm 0.0043^{+0.0044}_{-0.0045}$
4.00 - 4.50	$0.017 \pm 0.0027^{+0.0054}_{-0.0054}$
4.50 - 5.00	$0.0092 \pm 0.0019^{+0.0029}_{-0.0029}$
5.00 - 5.50	$0.0041 \pm 0.0013^{+0.0015}_{-0.0015}$
5.50 - 6.00	$0.0045 \pm 0.0011^{+0.0013}_{-0.0013}$
6.00 - 7.00	$0.0022 \pm 0.0006^{+0.0007}_{-0.0007}$
7.00 - 8.00	$0.0015 \pm 0.0004^{+0.0005}_{-0.0005}$

B Cut variation studies for the estimation of the systematic uncertainty of the p_t-differential invariant yield of the inclusive electron spectrum
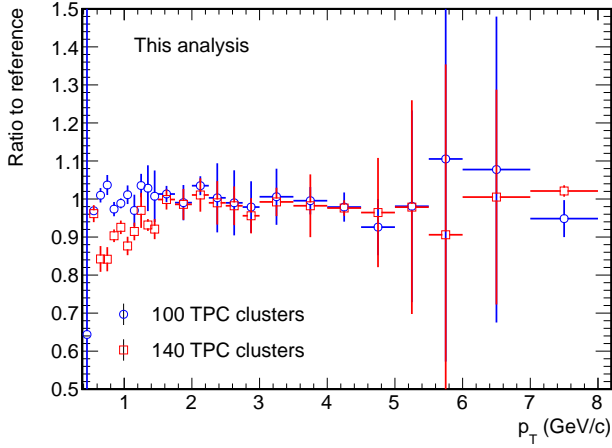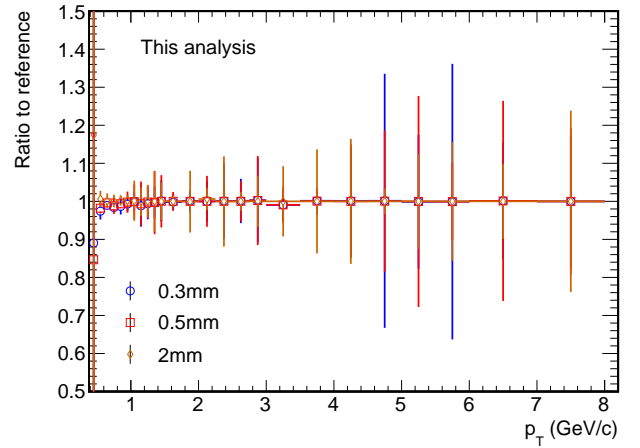

(a) Number of clusters in the TPC
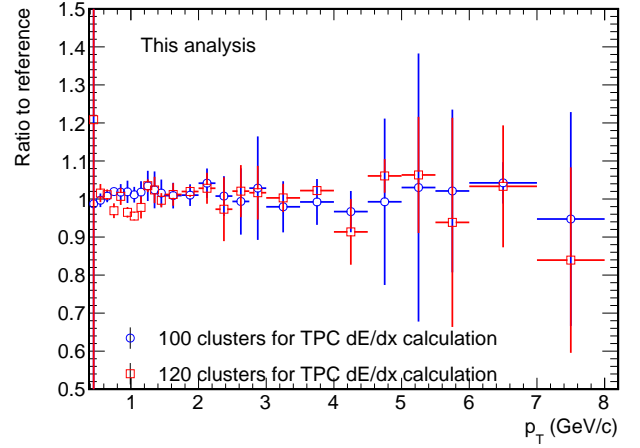
(b) Number of clusters for TPC dE/dx calculation
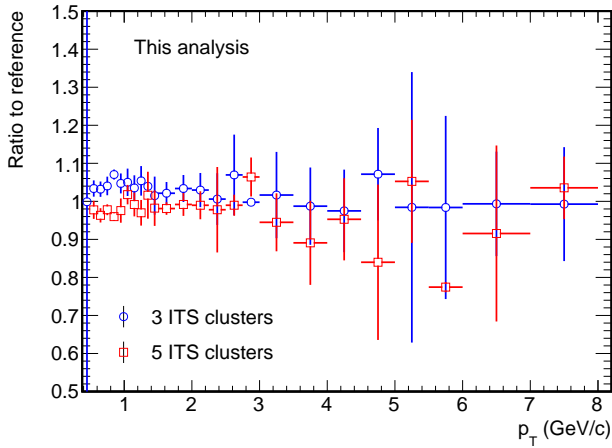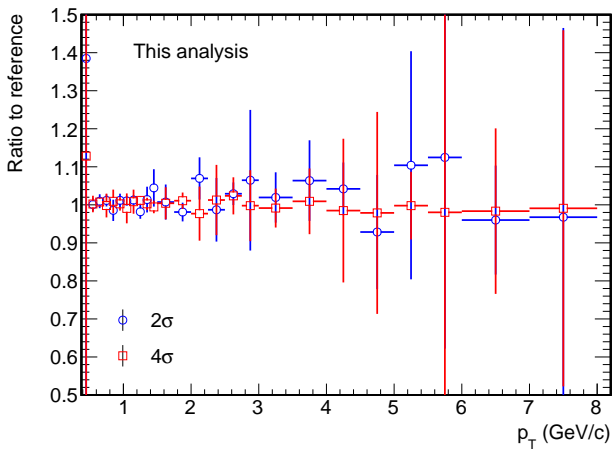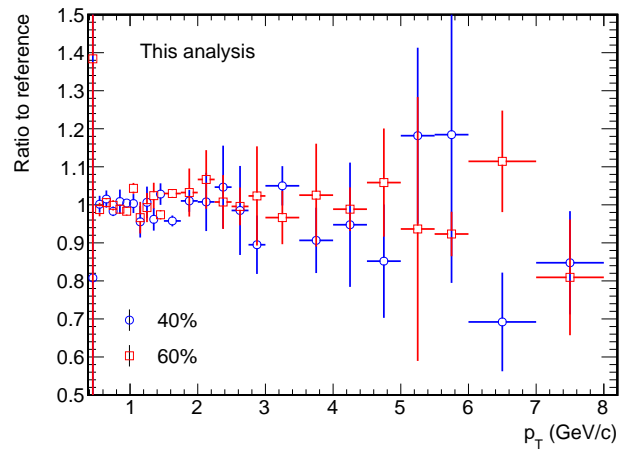

(c) Number of clusters in the ITS

(d) DCA to the primary vertex

Figure B.1: Overview of the cut variation studies: shown is the ratio of the corrected invariant yield of inclusive electrons after cut variation with respect to the reference spectrum for the cuts on the number of clusters in the TPC (a), the number of clusters used for the TPC dE/dx calculation (b), the number of clusters in the ITS (c), the DCA to the primary vertex (d), the TOF electron identification (e), and the TPC electron identification (f).

(e) Electron identification in the TOF

(f) Electron identification in the TPC

Figure B.1: Overview of the cut variation studies: shown is the ratio of the corrected invariant yield of inclusive electrons after cut variation with respect to the reference spectrum for the cuts on the number of clusters in the TPC (a), the number of clusters used for the TPC dE/dx calculation (b), the number of clusters in the ITS (c), the DCA to the primary vertex (d), the TOF electron identification (e), and the TPC electron identification (f).

C Fits to the charge distributions from the testbeam 2004
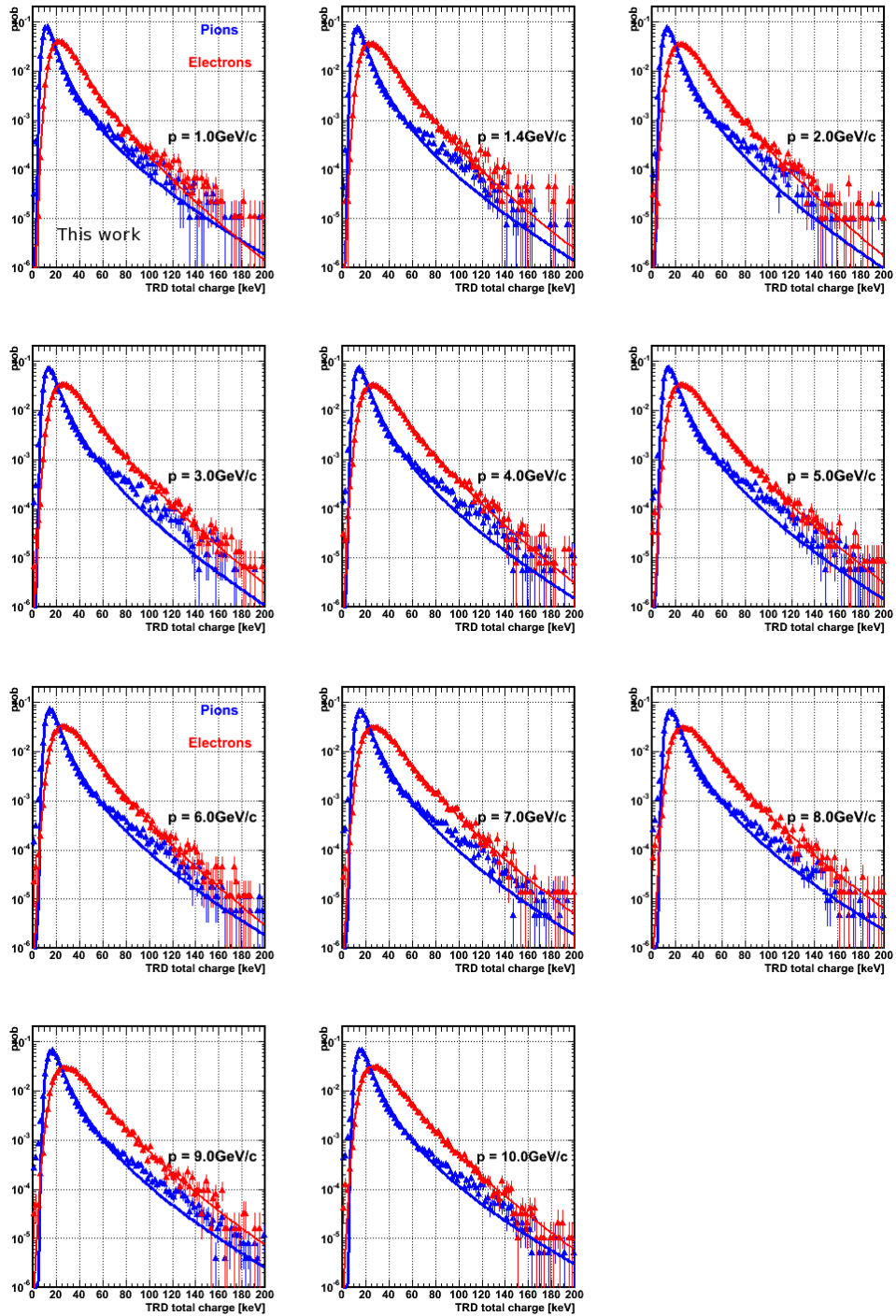
Figure C.1: Fits of the model in eq. 2.4 to the measure charge distribution for electrons (red) and pions (blue) to the charge distributions obtained from the testbeam 2004.

D Armenteros cuts used in the creation of the reference samples
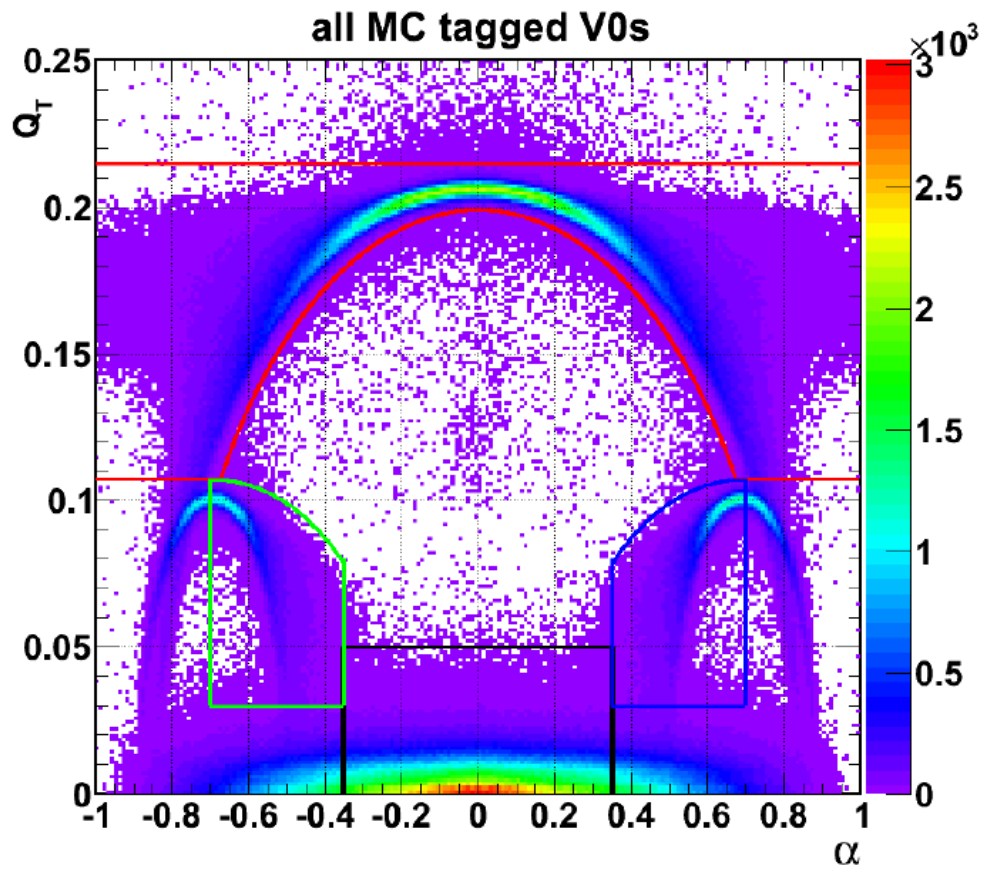
Figure D.1: Cuts applied to the Armenteros variables Q_t and α in order to create the reference samples for electrons from γ-conversions(black square), pions from K_S^0 (red box) and protons from Λ (blue box) respectively anti-Λ (green box)[116]

E List of runs at $\sqrt{s}$ = 7 TeV

Table E.1: List of runs in period LHC10d declared as good. Also shown is the number of min. bias events per run

Run number	Number of min. bias events	Run number	Number of min. bias events
122374	4243325	126008	1055555
122375	777367	126073	2753462
124751	371347	126078	5772669
125023	107975	126081	1887091
125085	5688313	126082	5961263
125097	4404112	126088	8084783
125100	395721	126090	7527753
125101	2494468	126097	1523169
125133	694319	126158	7811415
125134	3606871	126160	2046317
125139	6853300	126168	2224048
125140	2356763	126283	1463878
125156	215407	126284	7998200
125186	1658185	126285	297783
125296	6061566	126351	4427060
125628	3299193	126352	2240812
125630	2130626	126359	1377823
125632	3012186	126403	488043
125633	997631	126404	5979917
125842	2689629	126405	332506

Table E.1: List of runs in period LHC10d declared as good. Also shown is the number of min. bias events per run

Run number	Number of min. bias events	Run number	Number of min. bias events
125843	419241	126406	4851280
125844	177395	126407	5179710
125847	682019	126408	2624310
125848	753284	126409	1645111
125849	2131877	126422	4352831
125850	2446627	126424	7967680
125851	1810293	126425	1542525
125855	2773005	126432	8379629
126004	626203	126437	1888926
126007	4287397		

F Example configuration file used in the POWHEG simulation

Table F.1: Example of a POWHEG cofiguration file for bottom production. Values are shown for the central configuration. In order to obtain a systematical uncertainty, the mass (qmass) is varied by 0.25 GeV/c and the scales (facscfact and renscfact) from 0.5 to 2. For charm quarks the mass in the central prediction is chosen to be 1.5 GeV/c^2 and varied by 0.2GeV/c^2.

key	value	
ih1	1	ID of hadron 1 (proton)
ih2	1	ID of hadron 2 (proton)
lhans1	10550	LHAPDFcode of CTEQ6.6m used for hadron 1
lhans2	10550	LHAPDFcode of CTEQ6.6m used for hadron 2
ebeam1	3500	energy of beam 1 (GeV)
ebeam2	3500	energy of beam 2 (GeV)
qmass	4.75	mass of heavy quark in GeV/c^2
facscfact	1	factorization scale factor: $\mu_f = \mu_0 * facscfact$
renscfact	1	renormalization scale factor: $\mu_r = \mu_0 * renscfact$
ncall1	10000	number of calls for initializing the integration grid
itmx1	5	number of iterations for initializing the integration grid
ncall2	100000	number of calls for computing the integral and finding upper bound
itmx2	5	number of iterations for computing the integral and finding upper
bound foldcsi	2	number of folds on x integration
foldy	5	number of folds on y integration
foldphi	1	number of folds on phi integration
nubound	500000	number of bbarra calls to setup norm of upper bounding function
iymax	1	normalization of upper bounding function
ixmax	1	normalization of upper bounding function
xupbound	2	upper bound for radiation generation

Glossary

ACORDE	ALICE COsmic Ray DEtector
AGS	Alternating Gradient Synchrotron
ALICE	A Large Ion Collider Experiment
AliRoot	ALIce ROOT
ATLAS	A Toroidal LHC ApparatuS
ATLAS CSC	A tune of PYTHIA
Au–Au	gold-gold
BNL	Brookhaven National Laboratory
CDF	Collider Detector at Fermilab
CERN	European Organisation for Nuclear Research
CMS	Compact Muon Solenoid
CORRFW	ALICE Correction Framework
D0	D0 Experiment
DCA	Distance of closest approach
EMCAL	ElectroMagnetic CALorimeter
FMD	Forward Multiplicity Detector
FNAL	Fermi National Laboratory

FONLL	Fixed Order plus Next-to-Leading-Logarithms pQCD
GEANT3	Detector Simulation
GEANT4	Detector Simulation
GM-VFNS	General-mass variable-flavour-number scheme
HERWIG	Software for event generation and particle decays (*Hadron Emission Reactions With Interfering Gluons)*
HLT	High-Level Trigger
HMPID	High-Momentum Particle Identification Detector
ITS	Inner Tracking System
LHAPDF	Les Houches Accord PDF Interface
LHC	Large Hadron Collider
LHCb	LHC beauty
MIP	Minimum Ionising Particles
MRPC	Multi-gap Resistive Plate Chambers
NLO	Next-to-leading order
Pb-Pb	lead-lead
PDF	Parton Distribution Function
PDG	Particle Data Group

Perugia0	A tune of PYTHIA
PHENIX	Pioneering High Energy Nuclear Interactions eXperiment
PHOS	PHOton Spectrometer
PMD	Photon Multiplicity Detector
POWHEG	Positive Weight Hardest Emission Generator
pp	proton-proton
pQCD	perturbative QCD
PS	Proton Synchrotron
PYTHIA	Software for event generation and particle decays
QCD	Quantum Chromodynamics
QGP	Quark-Gluon Plasma
R$_{AA}$	Nuclear Modification Factor
RHIC	Relativistic Heavy Ion Collider
SDD	Silicon Drift Detector
SIS	Schwerionensynchrotron
SLAC	Stanford Linear Accelerator
SPD	Silicon Pixel Detector
SPS	Super Proton Synchrotron
SSD	Silicon Strip Detector
STAR	Solonoidal Tracker At RHIC

T0	T0 detector
TOF	Time-Of-Flight detector
TPC	Time Projection Chamber
TRD	Transition Radiation Detector
VZERO	VZERO detector
ZDC	Zero Degree Calorimeters

Bibliography

[1] B. Abelev et al. Measurement of electrons from semileptonic heavy-flavour decays in pp collisions at $\sqrt{s} = 7$ TeV. arxiv:hep-ex/1205.5423, submitted to Phys. Rev. D, 2012.

[2] P. A. Tipler and R. A. Llewellyn. *Modern Physics*. W. H. Freeman and Company, 2008.

[3] K. Nakamura et al. Review of particle physics. *J. Phys. G*, 37:075021, 2010. doi:10.1088/0954-3899/37/7A/075021.

[4] C. Berger. *Elementarteilchenphysik*. Springer-Lehrbuch, 2006. doi:10.1007/3-540-33594-3.

[5] P. Braun-Munzinger and J. Wambach. Colloquium: Phase diagram of strongly interacting matter. *Rev. Mod. Phys.*, 81:1031, 2009. doi:10.1103/RevModPhys.81.1031.

[6] F. Karsch. The Phase transition to the quark gluon plasma: Recent results from lattice calculations. *Nucl. Phys. A*, 590:367C, 1995. doi:10.1016/0375-9474(95)00248-Y.

[7] F. Karsch. Lattice QCD at high temperature and density. *Lect. Notes Phys.*, 583:209, 2002. arxiv:hep-lat/0106019.

[8] M.A. Stephanov. QCD phase diagram: An Overview. *PoS*, LAT2006:024, 2006. arxiv:hep-lat/0701002.

[9] A. Andronic and P. Braun-Munzinger. Ultrarelativistic nucleus-nucleus collisions and the quark gluon plasma. *Lect.Notes Phys.*, 652:35, 2004. arxiv:hep-ph/0402291.

[10] Y. Aoki, G. Endrodi, Z. Fodor, S.D. Katz, and K.K. Szabo. The Order of the quantum chromodynamics transition predicted by the standard model of particle physics. *Nature*, 443:675, 2006. doi:10.1038/nature05120.

[11] B Mohanty. STAR experiment results from the beam energy scan program at RHIC. *J. Phys. G*, 38:124023, 2011. doi:10.1088/0954-3899/38/12/124027.

[12] S. Bathe. PHENIX highlights. *J. Phys. G*, 38:124001, 2011. doi:10.1088/0954-3899/38/12/124001.

[13] H. Masui. STAR Highlights. *J. Phys. G*, 38:124002, 2011. doi:10.1088/0954-3899/38/12/124002.

[14] B. Friman, C. Höhne, J. Knoll, S. Leupold, J Randrup, R. Rapp, and P. Senger. The CBM Physics Book. *Lect. Notes Phys.*, 814:1, 2011. doi:10.1007/978-3-642-13293-3.

[15] Igor Shovkovy. Two Lectures on Color Superconductivity. *Foundations of Physics*, 35:1309, 2005. doi:10.1007/s10701-005-6440-x.

[16] C. Lourenco. Searching for quark matter at the CERN SPS. *Nucl. Phys. A*, 698:13, 2002. doi:10.1016/S0375-9474(01)01344-6.

[17] M.J. Tannenbaum. Recent results in relativistic heavy ion collisions: From 'a new state of matter' to 'the perfect fluid'. *Rept.Prog.Phys.*, 69:2005, 2006. doi:0.1088/0034-4885/69/7/R01.

[18] S. Chatrchyan et al. Study of high-pT charged particle suppression in PbPb compared to pp collisions at $\sqrt{s_{NN}}$ = 2.76 TeV, 2012. arxiv:nucl-ex/1202.2554.

[19] G. Aad et al. Observation of a Centrality-Dependent Dijet Asymmetry in Lead-Lead Collisions at $\sqrt{s_{NN}}$ = 2.76 TeV with the ATLAS Detector at the LHC. *Phys. Rev. Lett.*, 105:252303, 2010. doi:10.1103/PhysRevLett.105.252303.

[20] S. Chatrchyan et al. Observation and studies of jet quenching in PbPb collisions at $\sqrt{s_{NN}}$ = 2.76 TeV. *Phys. Rev. C*, 84:024906, 2011. doi:10.1103/PhysRevC.84.024906.

[21] P. Steinberg. Recent heavy-ion results with the ATLAS detector at the LHC. *J. Phys. G*, 38:124004, 2011. doi:10.1088/0954-3899/38/12/124004.

[22] J. A. Robles. Weak boson production measured in PbPb and pp collisions by CMS. *J. Phys. G*, 38:124132, 2011. doi:10.1088/0954-3899/38/12/124132.

[23] S. Chatrchyan et al. Study of *Z* Boson Production in PbPb Collisions at $\sqrt{s_{NN}}$ = 2.76 TeV. *Phys. Rev. Lett.*, 106:212301, 2011. doi:10.1103/PhysRevLett.106.212301.

[24] G. Aad et al. Measurement of the centrality dependence of yields and observation of Z production in lead-lead collisions with the ATLAS detector at the LHC. *Phys. Lett. B*, 697:294, 2011. doi:10.1016/j.physletb.2011.02.006.

[25] K. Aamodt et al. Two-pion Bose-Einstein correlations in central Pb–Pb collisions at. *Phys. Lett. B*, 696:328, 2011. doi:10.1016/j.physletb.2010.12.053.

[26] A. Białas, M. M. Bleszyński, and W. Czyż. Multiplicity distributions in nucleus-nucleus collisions at high energies. *Nucl. Phys. B*, 111:461, 1976. doi:10.1016/0550-3213(76)90329-1.

[27] R. J. Glauber and G. Matthiae. High-energy scattering of protons by nuclei. *Nucl. Phys. B*, 21:135, 1970. [doi:10.1016/0550-3213(70)90511-0](doi:10.1016/0550-3213(70)90511-0).

[28] A. Toia. Bulk properties of Pb–Pb collisions at $\sqrt{s_{NN}}$ = 2.76 TeV measured by ALICE. *J. Phys. G*, 38:124007, 2011. [doi:10.1088/0954-3899/38/12/124007](doi:10.1088/0954-3899/38/12/124007).

[29] S. S. Adler et al. Centrality Dependence of Direct Photon Production in $\sqrt{s_{NN}}$ =200 GeV Au + Au Collisions. *Phys. Rev. Lett.*, 94:232301, 2005. 10.1103/PhysRevLett.94.232301.

[30] S. Chatrchyan et al. Measurement of isolated photon production in pp and PbPb collisions at $\sqrt{s_{NN}}$ = 2.76 TeV. arxiv:nucl-ex/1201.3093.

[31] K. Adcox et al. Formation of dense partonic matter in relativistic nucleus–nucleus collisions at RHIC: Experimental evaluation by the PHENIX Collaboration. *Nucl. Phys. A,* 757:184, 2005. doi:10.1016/j.nuclphysa.2005.03.086.

[32] J. Adams et al. Experimental and theoretical challenges in the search for the quark–gluon plasma: The STAR Collaboration's critical assessment of the evidence from RHIC collisions. *Nucl. Phys. A,* 75:102, 2005. doi:10.1016/j.nuclphysa.2005.03.085.

[33] B.B. Back et al. The PHOBOS perspective on discoveries at RHIC. *Nucl. Phys. A,* 757:28, 2005. doi:10.1016/j.nuclphysa.2005.03.084.

[34] I. Arsene et al. Quark–gluon plasma and color glass condensate at RHIC? The perspective from the BRAHMS experiment. *Nucl. Phys. A,* 757:1, 2005. doi:10.1016/j.nuclphysa.2005.02.130.

[35] K. Aamodt et al. Suppression of charged particle production at large transverse momentum in central Pb–Pb collisions at $\sqrt{s_{NN}}$ = 2.76 TeV. *Phys. Lett. B,* 696:30, 2011. doi:10.1016/j.physletb.2010.12.020.

[36] A. Milov. Centrality dependence of charged particle spectra and R CP in Pb+Pb collisions at $\sqrt{s_{NN}}$ = 2.76 TeV with the ATLAS detector at the LHC. *J. Phys. G,* 38:124113, 2011. [doi:10.1088/0954-3899/38/12/124113](doi:10.1088/0954-3899/38/12/124113).

[37] A. Andronic, P. Braun-Munzinger, and J. Stachel. Thermal hadron production in relativistic nuclear collisions. *Acta Phys. Polon. B,* 40:1005, 2009. arxiv:nucl-th/0901.2909.

[38] A. Andronic, P. Braun-Munzinger, and J. Stachel. Thermal hadron production in relativistic nuclear collisions: The hadron mass spectrum, the horn, and the QCD phase transition. *Phys. Lett. B,* 673:142, 2009. doi:10.1016/j.physletb.2009.02.014.

[39] A. Andronic, P. Braun-Munzinger, and J. Stachel. Hadron production in central nucleus–nucleus collisions at chemical freeze-out. *Nucl. Phys. A*, 772:167, 2006. doi:10.1016/j.nuclphysa.2006.03.012.

[40] P. Braun-Munzinger and J. Stachel. The quest for the quark-gluon plasma. *Nature*, 448:302, 2007. doi:10.1038/nature06080.

[41] P. Braun-Munzinger, K. Redlich, and J. Stachel. Particle Production in Heavy Ion Collisions. In *Quark-Gluon Plasma*, page 491, 2004. arxiv:nucl-th/0304013.

[42] J. Cleymans, H. Oeschler, and K. Redlich. Influence of impact parameter on thermal description of relativistic heavy ion collisions at (1-2)AGeV. *Phys. Rev. C*, 59:1663, 1999. doi:10.1103/PhysRevC.59.1663.

[43] A. Andronic, P. Braun-Munzinger, K. Redlich, and J. Stachel. The thermal model on the verge of the ultimate test: particle production in Pb–Pb collisions at the LHC. *J. Phys. G*, 38:124081, 2011. doi:10.1088/0954-3899/38/12/124081.

[44] J. E. Augustin et al. Discovery of a Narrow Resonance in e^+e^- Annihilation. *Phys. Rev. Lett.*, 33:1406, 1974. doi:10.1103/PhysRevLett.33.1406.

[45] J. J. Aubert et al. Experimental Observation of a Heavy Particle J. *Phys. Rev. Lett.*, 33:1404, 1974. doi:10.1103/PhysRevLett.33.1404.

[46] S. W. Herb et al. Observation of a Dimuon Resonance at 9.5 GeV in 400-GeV Proton-Nucleus Collisions. *Phys. Rev. Lett.*, 39:252, 1977. doi:10.1103/PhysRevLett.39.252.

[47] M. L. Mangano, P. Nason, and G. Ridolfi. Heavy quark correlations in hadron collisions at next-to-leading order. *Nucl. Phys. B*, 373:295, 1992. doi:10.1016/0550-3213(92)90435-E.

[48] A. Andronic. private communication.

[49] M.R. Whalley, D. Bourilkov, and R.C. Group. The Les Houches accord PDFs (LHAPDF) and LHAGLUE, 2005. arxiv:hep-ph/0508110.

[50] C. Peterson, D. Schlatter, I. Schmitt, and P. M. Zerwas. Scaling violations in inclusive e^+e^- annihilation spectra. *Phys. Rev. D*, 27:105, 1983. doi:10.1103/PhysRevD.27.105.

[51] M. L. Mangano. The Saga of bottom production in $p\bar{p}$ collisions. *AIP Conf. Proc.*, 753:247, 2005. doi:10.1063/1.1896706.

[52] M. Cacciari, M. Greco, and P. Nason. The p_t spectrum in heavy flavor hadroproduction. *JHEP*, 9805:007, 1998. doi:10.1088/1126-6708/1998/05/007.

[53] B. A. Kniehl, G. Kramer, I. Schienbein, and H. Spiesberger. Reconciling Open-Charm Production at the Fermilab Tevatron with QCD. *Phys. Rev. Lett.*, 96:012001, 2006. doi:10.1103/PhysRevLett.96.012001.

[54] A. Dainese. Heavy-flavour production in Pb-Pb collisions at the LHC, measured with the ALICE detector. *J. Phys. G*, 38:124032, 2011. doi:10.1088/0954-3899/38/12/124032.

[55] Yu. L. Dokshitzer and D. E. Kharzeev. Heavy-quark colorimetry of QCD matter. *Phys. Lett. B*, 519:199, 2001. doi:10.1016/S0370-2693(01)01130-3.

[56] Dainese, A. private communication.

[57] J. Pumplin, D. Robert Stump, J. Huston, H. Lai, P. Nadolsky, and W. Tung. New Generation of Parton Distributions with Uncertainties from Global QCD Analysis. *JHEP*, 0207:012, 2002. doi:10.1088/1126-6708/2002/07/012.

[58] S. S. Adler et al. Single Electrons from Heavy-Flavor Decays in $p + p$ Collisions at $\sqrt{s} = 200$ GeV. *Phys. Rev. Lett.*, 96:032001, 2006. doi:10.1103/PhysRevLett.96.032001.

[59] A. Adare et al. Measurement of High-p_t Single Electrons from Heavy-Flavor Decays in $p + p$ Collisions at $\sqrt{s} = 200$ GeV. *Phys. Rev. Lett.*, 97:252002, 2006. doi:10.1103/PhysRevLett.97.252002.

[60] B. I. Abelev et al. Transverse Momentum and Centrality Dependence of High-p_t Nonphotonic Electron Suppression in Au + Au Collisions at $\sqrt{s_{NN}} = 200$ GeV. *Phys. Rev. Lett.*, 98:192301, 2007. doi:10.1103/PhysRevLett.98.192301.

[61] B. I. Abelev et al. Erratum: Transverse Momentum and Centrality Dependence of High-p_t Nonphotonic Electron Suppression in Au + Au Collisions at $\sqrt{s} = 200$ GeV [Phys. Rev. Lett. 98, 192301 (2007)]. *Phys. Rev. Lett.*, 106:159902, 2011. doi:10.1103/PhysRevLett.106.159902.

[62] H. Agakishiev et al. High p_t nonphotonic electron production in $p + p$ collisions at $\sqrt{s} = 200$ GeV. *Phys. Rev. D*, 83:052006, 2011. doi:10.1103/PhysRevD.83.052006.

[63] A. Adare et al. Energy Loss and Flow of Heavy Quarks in Au + Au Collisions at $\sqrt{s} = 200$ GeV. *Phys. Rev. Lett.*, 98:172301, 2007. doi:10.1103/PhysRevLett.98.172301.

[64] A. Mischke. A New correlation method to identify and separate charm and bottom production processes at RHIC. *Phys. Lett. B*, 671:361, 2009. doi:10.1016/j.physletb.2008.11.075.

[65] M. M. Aggarwal et al. Measurement of the Bottom Quark Contribution to Nonphotonic Electron Production in $p + p$ Collisions at $\sqrt{s}$ = 200 GeV. *Phys. Rev. Lett.*, 105:202301, 2010. doi:10.1103/PhysRevLett.105.202301.

[66] A. Adare et al. Measurement of Bottom Versus Charm as a Function of Transverse Momentum with Electron-Hadron Correlations in $p + p$ Collisions at $\sqrt{s}$ = 200 GeV. *Phys. Rev. Lett.*, 103:082002, 2009. doi:10.1103/PhysRevLett.103.082002.

[67] S. S. Adler et al. Measurement of single muons at forward rapidity in $p + p$ collisions at $\sqrt{s}$ = 200 GeV and implications for charm production. *Phys. Rev. D*, 76:092002, 2007. doi:10.1103/PhysRevD.76.092002.

[68] S. Wicks, W. Horowitz, M. Djordjevic, and M. Gyulassy. Heavy Quark Jet Quenching with Collisional plus Radiative Energy Loss and Path Length Fluctuations. *Nucl. Phys. A*, 783:493, 2007. doi:10.1016/j.nuclphysa.2006.11.102.

[69] P. Sorensen and X. Dong. Suppression of nonphotonic electrons from enhancement of charm baryons in heavy ion collisions. *Phys. Rev. C*, 74:024902, 2006. doi:10.1103/PhysRevC.74.024902.

[70] G. Martinez-Garcia, S. Gadrat, and P. Crochet. Consequences of a enhancement effect on the non-photonic electron nuclear modification factor in central heavy ion collisions at RHIC energy. *Phys. Lett. B*, 663:55, 2008. doi:10.1016/j.physletb.2008.01.079.

[71] G. Martinez-Garcia, S. Gadrat, and P. Crochet. Erratum to: Consequences of a enhancement effect on the non-photonic electron nuclear modification factor in central heavy ion collisions at RHIC energy [Phys. Lett. B 663 (2008) 55]. *Phys. Lett. B*, 666:533, 2008. doi:10.1016/j.physletb.2008.07.061.

[72] D. Acosta et al. Measurement of prompt charm meson production cross sections in $p\bar{p}$ collisions at $\sqrt{s}$ = 1.96 TeV. *Phys. Rev. Lett.*, 91:241804, 2003. doi:10.1103/PhysRevLett.91.241804.

[73] D. Acosta et al. Measurement of the B^+ total cross section and B^+ differential cross section $d\sigma/dp_T$ in $p\bar{p}$ collisions at $\sqrt{s}$ = 1.8 TeV. *Phys. Rev. D*, 65:052005, 2002. doi:10.1103/PhysRevD.65.052005.

[74] B. Abbott et al. The bb production cross section and angular correlations in pp collisions at $\sqrt{s}$ =1.8 TeV. *Phys. Lett. B*, 487(3):264, 2001. doi:10.1016/S0370-2693(00)00844-3.

[75] G. Pauletta et al. Heavy flavour production at the Tevatron. *J. Phys. G*, 31:817, 2005. doi:10.1088/0954-3899/31/6/023.

[76] D. Acosta et al. Measurement of the J/ψ meson and b-hadron production cross sections in $p\overline{p}$ collisions at $\sqrt{s}$ = 1960 GeV. *Phys. Rev. D*, 71:032001, 2005. doi:10.1103/PhysRevD.71.032001.

[77] B. Abelev et al. Measurement of charm production at central rapidity in proton-proton collisions at $\sqrt{s}$ = 7 TeV. *JHEP*, 1:1, 2012. doi:10.1007/JHEP01(2012)128.

[78] G. M. Innocenti. D_s^+ production at central rapidity in pp collisions at 7 TeV with the ALICE experiment. *EPJ Web Conf.*, 28:12001, 2012. doi:10.1051/epjconf/20122812001.

[79] R. Romita. Reconstruction and first observation of the charmed baryon Λ_c with AL-ICE@LHC. https://indico.cern.ch/materialDisplay.py?contribId= 414&sessionId=65&materialId=slides&confId=30248. Poster at the 22nd International Conference on Ultrarelativistic Nucleus-Nucleus Collisions (Quark Matter 2011).

[80] B. Abelev et al. Suppression of high transverse momentum D mesons in central Pb–Pb collisions at $\sqrt{s_{NN}}$ = 2.76 TeV. *JHEP*, 1209:112, 2012. doi:10.1007/JHEP09(2012)112.

[81] S. Chatrchyan et al. Suppression of non-prompt J/ψ, prompt J/ψ, and Y(1S) in PbPb collisions at $\sqrt{s_{NN}}$ = 2.76 TeV, 2012. arxiv:nucl-ex/1201.5069.

[82] B. Abelev et al. Heavy flavour decay muon production at forward rapidity in proton–proton collisions at $\sqrt{s}$ = 7 TeV. *Phys. Lett. B*, 708:265, 2012. doi:10.1016/j.physletb.2012.01.063.

[83] G. Aad et al. Measurements of the electron and muon inclusive cross-sections in proton-proton collisions at $\sqrt{s}$ = 7 TeV with the ATLAS detector. *Phys. Lett. B*, 707:438, 2012. doi:10.1016/j.physletb.2011.12.054.

[84] ALICE Collaboration. ALICE: Physics Performance Report, Volume I. *J. Phys. G*, 30:1517, 2004. doi:10.1088/0954-3899/30/11/001.

[85] CMS Collaboration. CMS Physics Technical Design Report, Volume I: Detector Performance and Software. Technical report, CERN, 2006.

[86] ATLAS Collaboration. ATLAS Detector and Physics Performance. Technical Design Report, Volume 1. Technical report, CERN, 1999.

[87] K. Aamodt et al. Production of pions, kaons and protons in pp collisions at $\sqrt{s}$ = 900 GeV with ALICE at the LHC. *Eur. Phys. J. C,* 71:1655, 2011. doi:10.1140/epjc/s10052-011-1655-9.

[88] J. Alme et al. The ALICE TPC, a large 3-dimensional tracking device with fast readout for ultra-high multiplicity events. *Nucl. Inst. Meth. A,* 622:316, 2010. doi:10.1016/j.nima.2010.04.042.

[89] H. Bethe. Zur Theorie des Durchgangs schneller Korpuskularstrahlen durch Materie. *Annalen der Physik*, 397:325, 1930.

[90] K Aamodt et al. First proton–proton collisions at the LHC as observed with the ALICE detector: measurement of the charged particle pseudorapidity density at $\sqrt{s}$ = 900 GeV. *Eur. Phys. J. C,* 65:111, 2010. doi:10.1140/epjc/s10052-009-1227-4.

[91] K. Aamodt et al. The ALICE experiment at the CERN LHC. *Journal of Instrumentation*, 3:S08002, 2008. doi:10.1088/1748-0221/3/08/S08002.

[92] P. Billoir. Track fitting with multiple scattering: A new method. *Nucl. Inst. Meth. A,* 225:352, 1984. doi:10.1016/0167-5087(84)90274-6.

[93] ALICE Collaboration. ALICE: Physics Performance Report, Volume II. *J. Phys. G,* 32:1295, 2006. doi:10.1088/0954-3899/32/10/001.

[94] E Scapparone. The Time-of-Flight detector of the ALICE experiment. *J. Phys. G,* 34:725, 2007. doi:10.1088/0954-3899/34/8/S82.

[95] ALICE Collaboration. ALICE Electromagnetic Calorimeter Technical Design Report. Technical report, CERN, 2008.

[96] ALICE Collaboration. ALICE Technical Design Report of the Photon Spectrometer (PHOS). Technical report, CERN, 1999.

[97] K. Aamodt et al. Rapidity and transverse momentum dependence of inclusive J/ψ production in pp collisions at $\sqrt{s}$ = 7 TeV. *Phys. Lett. B,* 704:442, 2011. doi:10.1016/j.physletb.2011.09.054.

[98] D. Stocco. Measurement of forward-rapidity heavy-flavour muons in proton-proton collisions at with alice. *Nucl. Phys. A,* 855:323, 2011. doi:10.1016/j.nuclphysa.2011.02.070.

[99] ALICE Collaboration. ALICE Technical Design Report of the Transition Radiation Detector. Technical report, CERN, 2001.

[100] A. Andronic et al. Transition radiation spectra of electrons from 1 to 10 GeV/c in regular and irregular radiators. *Nucl. Inst. Meth. A*, 558:516, 2006. doi:10.1016/j.nima.2005.12.188.

[101] A. Andronic et al. Pulse height measurements and electron attachment in drift chambers operated with Xe, CO(2) mixtures. *Nucl. Inst. Meth. A*, 498:143, 2003. doi:10.1016/S0168-9002(02)02083-1.

[102] C. Adler et al. Position reconstruction in drift chambers operated with Xe, (15%). *Nucl. Inst. Meth. A*, 540:140, 2005. doi:10.1016/j.nima.2004.11.016.

[103] J. Klein. Triggering with the ALICE TRD, 2011. arxiv:nucl-ex/1112.5110.

[104] S. Schmiederer. Development and Implementation of the Control System of the Pre-Trigger System of the Transition Radiation Detector at ALICE, 2008.

[105] M. Fasel. Hadronenproduktion in Proton-Proton Kollisionen. Master's thesis, Technische Universität Darmstadt, 2008.

[106] J. Thäder. *Commissioning of the ALICE High-Level Trigger*. PhD thesis, Frankfurt, U., 2012.

[107] M. Ivanov et al. Track reconstruction in high density environment. *Nucl. Inst. Meth. A*, 566:70, 2006. doi:10.1016/j.nima.2006.05.029.

[108] M. Fasel. Stand alone tracking in the ALICE Transition Radiation Detector, 2008. Project Proposal.

[109] S. Huber. *Ausrichtung des ALICE Übergangsstrahlungsdetektors sowie Zweiteilchenintensitätsinterferometrie identischer Pionen aus p+p Kollisionen bei LHC Energien von 900 GeV und 7.0 TeV* . PhD thesis, Technische Universität Darmstadt, 2011.

[110] M. Al-Helwi. Gain calibration of the ALICE Transition Radiation detector with ^{83}Kr. Diploma thesis, Ruprecht-Karls Universität Heidelberg, 2010.

[111] R. Bailhache et al. Calibration of the ALICE Transition Radiation Detector with the First Proton Beam Data. Technical report, GSI Helmholtzzentrum für Schwerionenforschung GmbH, 2009.

[112] R. Bailhache. *Calibration of the ALICE Transition Radiation Detector and a study of Z^0 and heavy quark production in pp collisions at the LHC*. PhD thesis, Technische Universität Darmstadt, 2009.

[113] F. Poppenborg. A Drift Velocity Monitor for the ALICE TRD, 2011.

[114] A. Wilk. Analysis of the electron/pion separation capability with real size ALICE TRD prototypes using a neural network algorithm. *Nucl. Inst. Meth. A,* 563:314, 2006. doi:10.1016/j.nima.2006.02.165.

[115] A. Wilk. *Particle Identification Using Artificial Neural Networks with the ALICE Transition Radiation Detector.* PhD thesis, Westfälische Wilhelms-Universität Münster, 2010.

[116] M. Kalisky. private communication.

[117] T. Dahms. Measurement of photons via conversion pairs with the PHENIX experiment at RHIC, 2005.

[118] M. Fasel. Hunting electrons from heavy-flavour hadron decays with the ALICE Transition Radiation Detector in proton-proton collisions at $\sqrt{s}$ = 7 TeV. https://indico.cern.ch/getFile.py/access?contribId=425&sessionId=65&resId=0&materialId=poster&confId=30248. Poster at the 22nd International Conference on Ultrarelativistic Nucleus-Nucleus Collisions (Quark Matter 2011).

[119] R. Bailhache and C. Lipppmann. New test beam results with prototypes of the ALICE TRD. *Nucl. Inst. Meth. A,* 563:310, 2006. doi:10.1016/j.nima.2006.02.157.

[120] R.Brun et al. GEANT Detector Description and Simulation Tool, 1994. CERN Program Library Long Write-up, W5013.

[121] A. Andronic et al. Energy loss of pions and electrons of 1-6 GeV/c in drift chambers operated with $XeCO_2$(15%). *Nucl. Inst. Meth. A,* 519:508, 2004. doi:10.1016/j.nima.2003.11.036.

[122] S. Agostinelli et al. GEANT4 - a simulation toolkit. *Nucl. Inst. Meth. A,* 506:250, 2003. doi:10.1016/S0168-9002(03)01368-8.

[123] S. Eidelman et al. Review of particle physics. *Phys. Lett. B,* 592:1, 2004. doi:10.1016/j.physletb.2004.06.001.

[124] B. Abelev et al. Measurement of electrons from beauty hadron decays in pp collisions at $\sqrt{s}$ = 7 TeV, 2012. arxiv:hep-ex/1208.1902.

[125] R. Vernet. private communication.

[126] R. Bailhache. private communication.

[127] S. Sakai. private communication.

[128] Y. Pachmayer. private communication.

[129] M. Völkl. private communication.

[130] J. Wiechula. private communication.

[131] A. Kalweit. private communication.

[132] ALICE TPC Collaboration. Definitions of TPC related track properties. Technical report, CERN, 2011.

[133] A. Kalweit. *Soft particle production with ALICE at LHC*. PhD thesis, Technische Universität Darmstadt, 2012.

[134] S. Masciocchi. private communication.

[135] T. Sjostrand et al. PYTHIA 6.4 Physics and Manual. *JHEP*, 0605:026, 2006. doi:10.1088/1126-6708/2006/05/026.

[136] P. Z. Skands. The Perugia Tunes, 2009. arxiv:hep-ph/0905.3418.

[137] Agostini, G. D. A multidimensional unfolding method based on Bayes' theorem. *Nucl. Inst. Meth. A*, 362:487, 1995. doi:10.1016/0168-9002(95)00274-X.

[138] R. Vernet. private communication.

[139] M. Gagliardi. Measurement of reference cross sections in pp and Pb-Pb collisions at the LHC in van der Meer scans with the ALICE detector. *AIP Conf. Proc.*, 1422:110, 2011. doi:10.1063/1.3692205.

[140] K Oyama. Cross-section normalization in proton–proton collisions at $\sqrt{s}$ = 2.76 and 7 TeV with ALICE at the LHC. *J. Phys. G*, 38:124131, 2011. doi:10.1088/0954-3899/38/12/124131.

[141] S. van der Meer. Calibration of the effective beam height in the ISR, 1968. CERN-ISR-PO-68-31, ISR-PO-68-31.

[142] B. Abelev et al. Measurement of inelastic, single and double diffraction cross sections in proton-proton collisions at LHC with ALICE, 2012. arxiv:hep-ex/1208.4968.

[143] R. Bailhache. private communication.

[144] R. Averbeck. private communication.

[145] B. Abelev et al. Neutral pion and η meson production in proton-proton collisions at $\sqrt{s} = 0.9$ TeV and $\sqrt{s} = 7$ TeV. arxiv:hep-ex/1205.5724, 2012.

[146] C. Tsallis. Possible Generalization of Boltzmann-Gibbs Statistics. *J.Statist.Phys.*, 52:479, 1988. doi:10.1007/BF01016429.

[147] E.L. Bratkovskaya et al. Meson m_T-scaling in heavy-ion collisions at SIS energies. *Phys. Lett. B*, 424:244, 1998. doi:10.1016/S0370-2693(98)00213-5.

[148] A. Adare et al. Production of omega mesons in p+p, d+Au, Cu+Cu, and Au+Au collisions at $\sqrt{s_{NN}} = 200$ GeV. *Phys. Rev. C*, 84:044902, 2011. doi:10.1103/PhysRevC.84.044902.

[149] Yu. Riabov. Measurement of leptonic and hadronic decays of omega and phi-mesons at RHIC by PHENIX. *J. Phys. G*, 34:925, 2007. doi:10.1088/0954-3899/34/8/S127.

[150] V. Khachatryan et al. Measurement of the Inclusive Upsilon production cross section in pp collisions at $\sqrt{s} = 7$ TeV. *Phys. Rev. D*, 83:112004, 2011. doi:10.1103/PhysRevD.83.112004.

[151] V. Khachatryan et al. Measurement of the Isolated Prompt Photon Production Cross Section in pp Collisions at $\sqrt{s} = 7$ TeV. *Phys. Rev. Lett.*, 106:082001, 2011. doi:10.1103/PhysRevLett.106.082001.

[152] S. Chatrchyan et al. Measurement of the differential cross section for isolated prompt photon production in pp collisions at 7 TeV. *Phys. Rev. D*, 84:052011, 2011. doi:/10.1103/PhysRevD.84.052011.

[153] L.E. Gordon and W. Vogelsang. Polarized and unpolarized prompt photon production beyond the leading order. *Phys. Rev. D*, 48:3136, 1993. doi:10.1103/PhysRevD.48.3136.

[154] M. Cacciari, S. Frixione, and P. Nason. The p_t spectrum in heavy-flavor photoproduction. *JHEP*, 0103:006, 2001. doi:10.1088/1126-6708/2001/03/006.

[155] M. Cacciari, S. Frixione, N. Houdeau, M. Mangano, P. Nason, and G. Ridolfi. Theoretical predictions for charm and bottom production at the LHC, 2012. arxiv:hep-ph/1205.6344.

[156] V.G. Kartvelishvili and A.K. Likhoded. Structure functions and leptonic width of heavy mesons. *Yad.Fiz.*, 42:1306, 1985.

[157] V.G. Kartvelishvili et al. On the fragmentation functions of heavy quarks into hadrons. *Phys. Lett. B*, 78:615, 1978. doi:10.1016/0370-2693(78)90653-6.

[158] M. Cacciari and P. Nason. Charm cross-sections for the Tevatron Run II. *JHEP*, 0309:006, 2003. doi:10.1088/1126-6708/2003/09/006.

[159] M. Cacciari, P. Nason, and R. Vogt. QCD predictions for charm and bottom production at RHIC. *Phys. Rev. Lett.*, 95:122001, 2005. doi:10.1103/PhysRevLett.95.122001.

[160] M. Kweon. private communication.

[161] A. Adare et al. Heavy-quark production in $p + p$ and energy loss and flow of heavy quarks in au + au collisions at $\sqrt{s_{NN}}$ =200 gev. *Phys. Rev. C*, 84:044905, 2011. doi:10.1103/PhysRevC.84.044905.

[162] J. Beringer et al. Review of particle physics. *Phys. Rev. D*, 86:010001, 2012.

[163] B. Abelev et al. Measurement of charm production at central rapidity in proton-proton collisions at $\sqrt{s}$ = 2.76 TeV, 2012. arxiv:hep-ex/1205.4007.

[164] ATLAS Collaboration. Comparison of D^* meson production cross sections with FONLL and GM-VFNS predictions. ATLAS-PHYS-PUB-2011-012,ATLAS-CONF-2011-017, 2011.

[165] LHCb Collaboration. Prompt charm production in pp collisions at $\sqrt{s}$ = 7 TeV. LHCb-CONF-2010-013, 2010.

[166] P. Nason. A new method for combining NLO QCD with shower Monte Carlo algorithms. *JHEP*, 1104:040, 2004. doi:dx.doi.org/10.1088/1126-6708/2004/11/040.

[167] S. Frixione, P. Nason, and C. Oleari. Matching NLO QCD computations with parton shower simulations: the POWHEG method. *JHEP*, 1107:070, 2007. doi:10.1088/1126-6708/2007/11/070.

[168] S. Alioli, P. Nason, C. Oleari, and E. Re. A general framework for implementing NLO calculations in shower Monte Carlo programs: the POWHEG BOX. *JHEP*, 0610:043, 2010. doi:10.1007/JHEP06(2010)043.

[169] S. Frixione, G. Ridolfi, and P. Nason. A Positive-weight next-to-leading-order Monte Carlo for heavy flavour hadroproduction. *JHEP*, 0709:126, 2007. doi:10.1088/1126-6708/2007/09/126.

[170] G. Corcella et al. HERWIG 6: an event generator for hadron emission reactions with interfering gluons (including supersymmetric processes). *JHEP*, 0101:010, 2001. doi:10.1088/1126-6708/2001/01/010.

[171] A. Moreas. Modeling the underlying event: generating predictions for the LHC. Technical report, CERN, 2009. ATL-PHYS-PROC-2009-045.

[172] ATLAS Collaboration. ATLAS Monte-Carlo Tunes for MC09. Technical report, CERN, 2010. ATL-PHYS-PUB-2010-002.

[173] R. Averbeck, N. Bastid, Z. Conesa del Valle, P. Crochet, A. Dainese, and X. Zhang. Reference heavy flavour cross sections in pp collisions at $\sqrt{s} = 2.76$ TeV, using a pQCD-driven $\sqrt{s}$-scaling of ALICE measurements at $\sqrt{s} = 7$ TeV, 2011. arxiv:hep-ph/1107.3243.

[174] X. Wang and M. Gyulassy. HIJING: A Monte Carlo model for multiple jet production in pp, pA and AA collisions. *Phys. Rev. D*, 44:3501, 1991. doi:10.1103/PhysRevD.44.3501.

[175] A. Kalweit. Particle identification in the ALICE experiment. *J. Phys. G*, 38:124073, 2011. doi:10.1088/0954-3899/38/12/124073.

[176] S. Masciocchi. Investigation of charm and beauty hadron production via semileptonic decays of heavy-flavour hadrons in pp at 7 TeV and Pb–Pb at 2.76 TeV with ALICE. *J. Phys. G*, 38:124069, 2011. doi:10.1088/0954-3899/38/12/124069.

[177] Y. Pachmayer. Measurement of the nuclear modification factor of electrons from heavy-flavour decays at mid-rapidity in Pb–Pb collisions at $\sqrt{s_{NN}} = 2.76$ TeV measured with ALICE. *J. Phys. G*, 38:124186, 2011. doi:10.1088/0954-3899/38/12/124186.

[178] A. Adare et al. Enhanced Production of Direct Photons in Au + Au Collisions at $\sqrt{s_{NN}} = 200$ GeV and Implications for the Initial State Temperature. *Phys. Rev. Lett.*, 104:132301, 2010. doi:PhysRevLett.104.132301.

Acknowledgements

At the end of this thesis it is time to express thanks to persons which have supported me during this work.

First of all I express my thanks to Professor Dr. Braun-Munzinger for giving me the opportunity to perform this work inside his group. Suggestions and comments were very helpful for the creation of this work. Further thanks go to the ALICE Collaboration for giving me the possibility to participate in the research project. Thanks goes to HGS-HIRe for the support to present my work in international conferences.

Special thanks I also express to my supervisors Dr. Silvia Masciocchi and Dr. Anton Andronic for the excellent support, many productive discussions, and the patience with me.

Many thanks go to the ALICE TRD group, in particular Prof. Dr. Stachel, Dr. Alexandru Bercuci, Dr. Ionut Arsene and Dr. Alexander Wilk. Working in this group was always a nice experience.

Also I express my thanks also belong to the ALICE heavy-flavour electron group, in particular Dr. Ralf Averbeck, Dr. Raphaelle Bailhache-Roemer, Dr. Matus Kalisky, Dr. MinJung Kweon, Dr. Yvonnne Pachmayr and Dr. Shingo Sakai for the excellent collaboration in the group.

Last but not least I express thanks to my parents for the support during whole my studies.

Index

Curriculum Vitae

Name:	Markus Fasel
Birth:	July 28th, 1983 in Koblenz (Germany)
Nationality:	German
Address:	Christian-Götz Str. 22
	64319 Pfungstadt
E-Mail:	m.fasel@gsi.de

Education

2006 - 2008   Technische Universität Darmstadt

                 Graduation: Master of Science

                 Thesis title: *Hadronenproduktion in Proton-Proton Kollisionen*

2003 - 2006   Technische Universität Kaiserslautern & Technische Universität Darmstadt

                 Graduation: Bachelor of Science

                 Thesis title: *LabVIEW-Programmierung zur Automatisierung von Messprozessen im Rahmen des LIDAR-Projektes*

1994 - 2003   Gymnasium im Kannebäckerland

                 Graduation: Abitur

Publications

- *Measurement of the nuclear modification factor of electrons from heavy-flavour hadron decays in Pb–Pb collisions at $\sqrt{s_{NN}} = 2.76$ TeV with ALICE at the LHC,* Proceedings of the International Workshop on Early Physics with Heavy-ion Collisions at the LHC (EPIC@LHC), AIP Conference Proceedings, 1422:135, 2012

- *Measurement of electrons from semileptonic heavy-flavour hadron decays in pp collisions at $\sqrt{s} = 7$ TeV,* arxiv:hep-ex/1205.5423, submitted to Phys. Rev. D

Talks and Posters

- *Measurement of electrons from semi-electronic heavy-flavour hadron decays in proton-proton collisions at $\sqrt{s}$ = 7 TeV with ALICE,* Poster at the LHCC Poster Session, Geneva, 2012

- *Hunting electrons from heavy flavour hadron decays with the ALICE Transition Radiation Detector in proton-proton collisions at $\sqrt{s}$ = 7 TeV,* Poster at the 486th WE-Heraeus-Seminar: Characterization of the Quark Gluon Plasma with Heavy Quarks, Bad Honnef, 2011

- *Measurement of the nuclear modification factor of electrons from heavy-flavour hadron decays in Pb–Pb collisions at $\sqrt{s_{NN}}$ = 2.76 TeV with ALICE at the LHC,* Talk at the International Workshop on Early Physics with Heavy-ion Collisions at the LHC (EPIC@LHC), Bari, 2011

- *Hunting electrons from heavy flavour hadron decays with the ALICE Transition Radiation Detector in proton-proton collisions at $\sqrt{s}$ = 7 TeV,* Poster at the XXII International Conference on Ultrarelativistic Nucleus-Nucleus Collisions (Quark Matter 2001), Annecy, 2011

- *Messung des Wirkungsquerschnitts von Hadronen mit schweren Quarks in Proton-Proton Kollisionen mit dem ALICE Experiment,* Talk at the DPG Frühjahrstagung Münster, 2011

- *Spurrekonstruktion und Teilchenidentifikation mit dem ALICE Übergangsstrahlungsdetektor,* Talk at the DPG Frühjahrtagung Bonn, 2010

- *First Results from the ALICE Transition Radiation Detector,* Talk at the XI Arbeitstreffen der Kernphysiker Schleching, 2010

- *Reconstruction performance of the ALICE Transition Radiation Detector,* Talk at the DPG Frühjahrstagung Bochum, 2009

- *Stand alone Tracking in the ALICE Transition Radiation Detector,* Talk at the DPG Frühjahrstagung Darmstadt, 2008